Advances in Mathematical Physics

Foundations of Relativistic Quantum Mechanics: Mathematical Structures and Evolution Equations

Lead Guest Editor: David Carfi
Guest Editors: Alfonso Agnew and Luiz Roberto Evangelista

Foundations of Relativistic Quantum Mechanics: Mathematical Structures and Evolution Equations

Advances in Mathematical Physics

Foundations of Relativistic Quantum Mechanics: Mathematical Structures and Evolution Equations

Lead Guest Editor: David Carfi
Guest Editors: Alfonso Agnew and Luiz Roberto Evangelista

Contents

Hindawi
Advances in Mathematical Physics
Volume 2022, Article ID 6423730, 16 pages
https://doi.org/10.1155/2022/6423730

Research Article

Analytic Simulation for Magnetohydrodynamic Unsteady Buongiorno Model Hybrid Nanofluid Flow over Stretching

Muhammad Jawad,[1] Salah Boulaaras,[2] Niaz Ali Shah,[1] Rashid Jan,[1] and Sulima Ahmed Zubair[2,3]

[1]*Department of Mathematics, University of Swabi, Swabi, 23561 KPK, Pakistan*
[2]*Department of Mathematics, College of Sciences and Arts, Qassim University, Ar Rass, Saudi Arabia*
[3]*Department of Mathematics, College of Sciences, Juba University, Sudan*

Correspondence should be addressed to Sulima Ahmed Zubair; sulimaa2021@gmail.com

Received 29 August 2021; Revised 11 January 2022; Accepted 4 April 2022; Published 13 June 2022

Academic Editor: John D. Clayton

In this work, we inspect and analyze a two dimensional, unsteady mixed convectional hybrid nanofluid hydromagnetic flow (Al_2O_3-Cu/H_2O) over a convectional heated an extending/contracting surface with the influence of thermal radiation. Hybrid nanofluid (Al_2O_3-Cu/H_2O) flows with magnetohydrodynamic and heat source or sink. Brownian motion and thermophoresis were incorporated using the Buongiorno model. Hybrid nanofluid with vol. fraction range limited to 1.5% and within the higher temperature range of 50°C to 70°C is considered for thermal conductivity and viscosity analysis. The proposed model is then converted into ODEs through similarity transformation with the help of homotopy analysis. The effect of embedded input factors on the temperature, velocity, and concentration profiles is visually demonstrated and explained. The magnetic field has inverse impact on velocity and temperature profiles. Velocity profile increases for both mixed convection and buoyancy ratio parameters. It has been noticed that the temperature profile increases with thermal radiation. For increasing values of Lewis number, the concentration of hybrid nanoparticles is considerably lowered. Moreover, we observed an increase in the concentration of hybrid nanoparticles through a destructive chemical reaction, whereas a generative chemical reaction has the reverse effect. It has been proved that skin friction is increasing function of $\varepsilon, M$and decreasing function of λ_1, N_r. On the other hand, Nusselt number increased with the increase of R, Q, N_b, N_t while Sherwood number is decreased, with the increase of N_b, N_t, Le.

1. Introduction

It is eminent that many studies have been carried out on two cases of nanoparticles floating in a base fluid known as "Hybrid Nanofluid" the forefront nanofluid. The key importance of the hybrid nanofluid is that by selecting the right mix of nanoparticles, favorable characteristics may be enhanced, and drawbacks can be mitigated owing to their interactive influence. It is reported that these hybrid nanofluids are new and have a number of application acoustics, defense, manufacturing, transportation, medical, microfluidics, and naval constructions. Nanofluid flow, in particular, is long familiar for its high heat conveyance when equated to regular fluid. The hybrid nanofluid is applied to raise it even further. Jamshed and Aziz [1] studied the Cattaneo-Christov heat flux impact and discovered that spherical shaped nanoparticles transmit heat at the fastest rate when compared to hexagon, platelet type nanoparticles. The authors in [2] examined squeezing flow in a hybrid base fluid with nanoparticles suspended in it. The hybrid nanofluid stagnation point flow past an extending sheet was investigated by the researchers [3]. The influence on flow

between two riga-plates was investigated by Ahmed et al. [4]. The authors in [5] studied the impact of changing viscosity on a stretched sheet containing hybrid nanoparticles using the Runge–Kutta fourth order technique. The researchers in [6] interrogated the synthesis of hybrid nanofluid while in [7] examined the effects of a hybrid nanofluid of (Al_2O_3-Cu/H_2O) on heat transmission.

There are numerous numerical methods in the literature to inspect the boundary layer flow and heat transport of a hybrid nanofluid. These concepts were further explored by the researchers in their research [9] to conceptualize the main idea. The problem was then expanded to a three-dimensional flow capable to the Newtonian heating consideration by the authors [10]. In both the above studies, they obtained key results about the heat transfer. The difficulty of a hybrid nanofluid consisting of a rotating flow was described by Hayat and Nadeem [11]. Zainal et al. [12] inspected the unsteady stagnation point flow of a hybrid nanofluid past a convectional heated an extending/contracting surface while accounting for velocity slip's influence on heat transfer. Using the Buongiorno model, Daniel et al. [13] investigated an unstable blended convectional electrical magnetohydrodynamic (MHD) flow and heat conveyance generated by nanofluid across a permeable stretched surface. The friction coefficient and wear volume were studied by Xie et al. [14] to determine the tribological properties of hybrid nanoparticles. Devi and Anjali [10] investigated the three-dimensional flow of (Cu-Al_2O_3/water) copper alumina/water hybrid nanofluid using the RK-Fehlberg integration technique.

Thermal radiation's effect on MHD blood flow and heat conveyance in a permeable capillary in extending motion was inspected. It has been examined that at high temperatures, heat transfer and thermal radiation are recognized to have a significant influence on numerous physiological processes, technological, and engineering industry equipment. Solar collector performance, plume dynamics, rocket propulsion, high-dose cancer therapy, fire propagation, material processing, and combustion systems are just a few examples. With the advancement of analytical and computational techniques, thermal convection flows with high radiative flux have received more attention recently. The effect of heat radiation on peristaltic transport of ionic nanoliquids in biomicrofluid channels had analyzed by Prakash et al. [15]. In context from melting heat transfer and thermal radiation, the researcher [16] proposed the dynamics of stagnation point flow of carbon nanotubes. To get series solution, the optimal homotopy technique was used. Muhammad et al. [17] make another notable attempt to address the key aspects of heat radiation and viscous dissipation impacts in a viscous nanofluid. Mixed convectional and slide impacts in viscous nanofluid across an extended sheet were described by Hsiao [18]. The solution was numerically defined using the convective boundary conditions [19]. The reader can further study about heat transfer through nanofluid flow in refs. [20–27]. The relevant study has been seen in [28–31].

The main aim of this research is to see how magnetic fields, thermal radiation, and heat generation/absorption affect unstable hybrid nanofluid hydromagnetic flow (Al_2O_3-Cu/H_2O) across a convectional heated an extending/contracting surface. The thermophoresis and Brownian motion characteristics were included in the Buongiorno model. To minimize the autonomous variables in governance equations resulting from mathematical modelling, a suitable collection of dimensionless variables is employed. By implementing the homotopy approach, an analytical solution has been calculated. Comparison between HAM and ND solve has been shown in Table 1.

2. Mathematical Formulation

Assume the unsteady hybrid nanofluid hydromagnetic flow (Al_2O_3-Cu/H_2O) past a convectional heated an extending/contracting surface in the bearing of the magnetic field, chemical reaction, heat generation/absorption, and thermal radiation. The flow problem plot is depicted in Figure 1, where $u_w(x,t) = bx/(1-ct)$, the extending/contracting is surface velocity, b indicates a constant that agree to extending ($b > 0$) and contracting($b < 0$) instances, and c denotes the problem of unsteadiness. The velocity of the free stream is notified by $u_e(x,t) = ax/(1-ct)$, where $a > 0$ is the strength of the stagnation flow. T_1 and T_0 are used to represent the ambient and reference temperature separately. Then, we consider that the bottom of the surface is heated by convectional from a hot fluid at a particular temperature $T_f(x,t) = T_1 - T_0(ax^2/2v)(1-ct)^{-3/2}$ and coefficient of heat transfer has noted by h_f while the mass transfer coefficient is indicated by h_s. The governing boundary layer equations may be recognized as [12, 13] based on all of the assumptions mentioned.

$$\frac{\partial u}{\partial x} + \frac{\partial u}{\partial y} = 0, \tag{1}$$

$$\frac{\partial u}{\partial t} + u\frac{\partial u}{\partial x} + v\frac{\partial u}{\partial y} = \frac{\partial u_e}{\partial t} + \mu_e\frac{\partial u_e}{\partial x} + \frac{\mu_{hnf}}{\rho_{hnf}}\frac{\partial^2 u}{\partial y^2} + \frac{1}{\rho_{hnf}}\left[(1-C_\infty)\beta_{hnf}\rho_f(T-T_\infty) - \left(\rho_p - \rho_f\right)(C-C_\infty)\right]g + \frac{\sigma_{hnf}\beta_0^2}{\rho_{hnf}(1-ct)}u, \tag{2}$$

$$\frac{\partial T}{\partial t} + u\frac{\partial T}{\partial x} + v\frac{\partial T}{\partial y} = \frac{k_{hnf}}{(\rho c_p)_{hnf}}\frac{\partial^2 T}{\partial y^2} + \frac{1}{(\rho c_p)_{hnf}}\left(\frac{\partial q_r}{\partial y}\right) + \tau\left[D_B\left(\frac{\partial C}{\partial y}\frac{\partial T}{\partial y}\right) + \frac{D_T}{T_\infty}\left(\frac{\partial T}{\partial y}\right)^2\right] + \frac{Q_0}{(\rho c_p)_{hnf}}(T-T_\infty), \tag{3}$$

Applying concept of Rosseland approximation q_r is as follows:

$$q_r = -\frac{4\sigma_1}{3k^*}\frac{\partial T^4}{\partial y}, \tag{4}$$

Table 1: Comparison of HAM with ND solve solution $\phi_1 = 0.25, \phi_2 = 0.25, \varepsilon = 0.3, N_r = 1.0, \lambda_1 = 0.2, Q = 0.5$, Pr = 6.5, $M = 0.5, R = 0.5$, $Sc = 1.0, N_t = 0.2, N_b = 0.1$.

η	$f(\eta)$		$f'(\eta)$		$\theta(\eta)$		$\Phi(\eta)$	
	HAM	ND solve	HAM	ND solve	HAM	ND solve	HAM	ND solve
0	0	0	0.02453760	0.02452978	0.487	0.487	0.55	0.55
0.5	0.03469568	0.03468659	0.04076865	0.04056421	0.50874001	0.50873986	0.61285007	0.61284999
1.0	0.06034958	0.06033885	0.20425912	0.20425742	0.51243432	0.51242415	0.55162402	0.55162416
1.5	0.12373158	0.12373098	0.21768635	0.21767085	0.52785902	0.52785899	0.84572417	0.84572406
2.0	0.11524238	0.11519427	0.22753476	0.22753087	0.53762042	0.53761997	0.85465107	0.85465099
2.5	0.28505217	0.28505214	0.10843705	0.10843604	0.54702062	0.54701015	1.04640087	1.04640015
3.0	0.37086918	0.37086908	0.10784304	0.10784291	0.49093352	0.49093295	1.04465601	1.04465592
3.5	0.39292487	0.39292467	0.02030697	0.02030691	0.47529652	0.47529605	1.03547618	1.03547608
4.0	0.40946208	0.40946179	0.02363014	0.02363001	0.48842752	0.48842702	1.03840447	1.03840396
4.5	0.41575308	0.41575305	0.04157226	0.04155423	0.49605602	0.49605595	1.03905327	1.03915306
5.0	0.42407258	0.42407239	0.04216302	0.04216271	0.39754262	0.39754187	1.05743307	1.05743298
5.5	0.44812538	0.44810615	0.04341604	0.04341581	0.35504732	0.35504711	1.05816737	1.05816706
6.0	0.45242414	0.45242409	0.04539012	0.04538997	0.34648862	0.34648795	1.00908797	1.00908706
6.5	0.47365747	0.47365729	0.04683201	0.04683192	0.35742472	0.35703415	0.94253457	0.94253406
7.0	0.49502798	0.49502796	0.04765024	0.04764981	0.37508582	0.37508565	0.92718608	0.92718594
7.5	0.50392098	0.50391896	0.04852079	0.04851972	0.38710902	0.38710875	0.85842701	0.85842689

where the parameters σ_1 and k^* are explained in nomenclature

$$T^4 = 4T_0^4 T - 3T_0^4. \tag{5}$$

Further simplification leads us to the following:

$$(q_r)_y = -\frac{16\sigma_1 T_0^3}{3k^*} T_{yy}. \tag{6}$$

Here, we rewrite Equation (3) as follows:

$$\frac{\partial T}{\partial t} + u\frac{\partial T}{\partial x} + v\frac{\partial T}{\partial y} = \frac{k_{hnf}}{(\rho c_p)_{hnf}}\frac{\partial^2 T}{\partial y^2} + \frac{1}{(\rho c_p)_{hnf}}\left(\frac{\partial q_r}{\partial y}\right) + \tau\left[D_B\left(\frac{\partial C}{\partial y}\frac{\partial T}{\partial y}\right) + \frac{D_T}{T_\infty}\left(\frac{\partial T}{\partial y}\right)^2\right] + \frac{Q_0}{(\rho c_p)_{hnf}}(T - T_\infty), \tag{7}$$

$$\frac{\partial C}{\partial t} + u\frac{\partial C}{\partial x} + v\frac{\partial C}{\partial y} = D_B\frac{\partial^2 C}{\partial y^2} + \left(\frac{D_T}{T_\infty}\right)T_{yy}, \tag{8}$$

where u denotes the factor of velocity in x-axis, v is the velocity factor in y-axis, μ_{hnf} is the Al_2O_3-Cu/H_2O dynamic viscosity, and D_b and D_t are the Brownian thermophoretic diffusion terms while ρ_{hnf} is the density of Al_2O_3-Cu/H_2O, T is the Al_2O_3-Cu/H_2O temperature, k_{hnf} is the thermal/heat conductivity of Al_2O_3-Cu/H_2O, and $(\rho c_p)_{hnf}$ is the Al_2O_3-Cu/H_2O heat capacity. The boundary conditions, as well as the velocity partial slip, are set to

$$u = u_w(x,t) + H_1 v\frac{\partial u}{\partial y}, v = 0, -k_{hnf}T_y = h_f\left(T_f - T\right), D_b C_y = h_s\left(C_f - C\right) \text{ at } y = 0,$$

$$u \longrightarrow u_e(x,t), T \longrightarrow T_\infty, C \longrightarrow C_\infty \text{ at } y \longrightarrow \infty, \tag{9}$$

where $H_1 = H(1-ct)^{1/2}$ is the velocity slip term, in which H stands for the starting merit of the velocity slip term. Table 2 lists the thermophysical characteristics of copper (Cu), as well as aluminium oxide (Al_2O_3) and water (H_2O) nanoparticles. The thermophysical characteristics of hybrid nanofluid are shown in Table 3. The solid volume fraction of nanoparticles is described as ϕ, where ρ_f denotes the density, ρ_s is the density of the hybrid nanoparticle, c_p is the constant pressure of heat capacity, k_f represents the thermal conductivity of H_2O, and k_s is the thermal conductivity of the hybrid nanoparticle.

The follower similarity transformations are provided in order to represent the governed Equations (1), (2), (7), and (8) concerning the BCs (9) in a much easy way [12].

$$\psi = \left(\frac{av}{1-ct}\right)^{1/2} xf(\eta), \theta(\eta) = \frac{T - T_\infty}{T_f - T_\infty},$$

$$\Phi(\eta) = \frac{C - C_\infty}{C_f - C_\infty}\eta = \left(\frac{a}{v(1-ct)}\right)^{1/2} y, \tag{10}$$

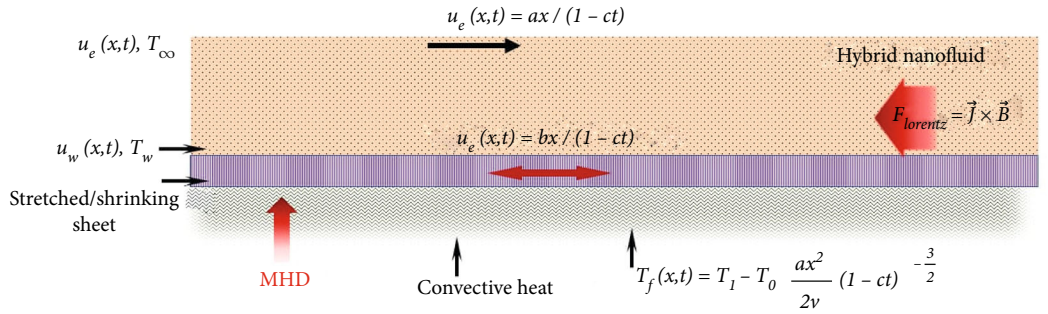

Figure 1: Schematic diagram of the 2D flow past a stretching/shrinking sheet.

Table 2: Cu thermophysical properties along with Al_2O_3 and H_2O [12].

Thermophysical properties	Cu	Al_2O_3	H_2O
k(W/mK)	400	40	0.613
$\rho(\mathrm{kg/m^3})$	8933	3970	9971
c_p(J/kgK)	385	765	4179
$\beta \times 10^5(1/\mathrm{K})$	1.67	0.85	21

where ψ is the stream function that can be specified as $u = \partial\psi/\partial y$ and $v = -\partial\psi/\partial x$ and η is the similarity variable. Thus, we attain

$$u = \frac{ax}{1-ct} f'(\eta), v = -\left(\frac{av}{1-ct}\right)^{1/2} f(\eta). \tag{11}$$

Equations (2), (7), and (8) are converted into the following set of nonlinear similarity ODEs by using the similarity variables (10) and (11) in light of the aforementioned relationships.

$$\frac{\mu_{hnf}/\mu_f}{\rho_{hnf}/\rho_f} f''' + 2ff'' - f'^2 + 1 - \varepsilon\left(f' - \frac{1}{2}\eta f'' - 1\right) - \lambda\frac{\beta_{hnf}}{\beta}\left[\theta - \frac{N_r}{\beta_{hnf}/\beta}\phi\right] + \frac{\sigma_{hnf}/\sigma_f}{\rho_{hnf}/\rho_f} M f' = 0, \tag{12}$$

$$\frac{1}{\mathrm{Pr}} \frac{1}{(\rho c_p)_{hnf}/(\rho c_p)_f} \left(\frac{k_{hnf}}{k_f} + \frac{4}{3}R\right)\theta'' + f\theta' - 2f'\theta + \frac{\varepsilon}{2}\left(\eta\theta' + 3\theta\right) + \left[N_b\theta'\Phi' + N_t\theta'^2\right] + \frac{Q(\rho c_p)_f}{(\rho c_p)_{hnf}}\theta = 0, \tag{13}$$

$$\Phi'' + Scf\Phi' - Sc\frac{\varepsilon}{2}\left(\eta\Phi' + 3\Phi\right) + \frac{N_t}{N_b}\theta'' = 0. \tag{14}$$

Now the starting and final constraints (9) are also changed into the following:

$$f(0) = 0, f'(0) = \lambda + \gamma f''(0),$$
$$-\frac{k_{hnf}}{k_f}\theta'(0) = Bi[1 - \theta(0)],$$
$$\Phi'(0) = -N_d(1 - \Phi(0)),$$
$$f'(\eta) \longrightarrow 1, \theta(\eta) \longrightarrow 0, \Phi(\eta) \longrightarrow 0, \text{while } \eta \longrightarrow \infty, \tag{15}$$

where $\varepsilon, M, R, \mathrm{Pr}, N_r, Bi, \mathrm{Re}_x, \lambda, Q, \lambda_1, Sc, N_t$, and N_b are unsteadiness parameter, magnetic parameter, thermal radiation parameter, Prandtl number, buoyancy ratio parameter, Biot number, local Reynolds number in x-axis, ratio of velocity parameter, heat source/sink parameter, mixed convection parameter, Lewis number, thermophoretic parameter, and Brownian motion parameter.

$$\varepsilon = \frac{c}{a}, M = \frac{\sigma\beta_0^2}{\rho_f a}, \gamma = H(av)^{1/2},$$
$$Bi = \frac{h_f}{k_f}\sqrt{\frac{v(1-ct)}{a}},$$
$$\mathrm{Re}_x = \frac{u_e x}{v}, R = \frac{4\sigma^* T_\infty^3}{3k^* k_f}$$
$$Q = \frac{Q_0(1-ct)^2}{ax}, \mathrm{Pr} = \frac{v}{\alpha},$$
$$N_r = \frac{\left(\rho_p - \rho_f\right)\Delta C}{\rho_f\beta(1 - C_\infty)\Delta T},$$
$$\lambda = \frac{b}{a}, \lambda_1 = \frac{Gr}{(\mathrm{Re}_x)^2},$$
$$Sc = \frac{v}{D_B}, N_t = \frac{\tau D_T(T_s - T_0)}{\nu_f T_0},$$
$$\mathrm{N}_b = \frac{\tau D_B(C_w - C_\infty)}{\nu_f}. \tag{16}$$

Table 3: Applied models for thermophysical properties of the hybrid nanofluid [12].

Property	Hybrid nanofluid
Viscosity	$\mu_{hnf} = 1/\left(1-\phi_{hnf}\right)^{2.5}$
Density	$\rho_{hnf} = \left(1-\phi_{hnf}\right)\rho_f + \phi_1\rho_{s1} + \phi_2\rho_{s2}$
Thermal capacity	$\left(\rho c_p\right)_{hnf} = \left(1-\phi_{hnf}\right)\left(\rho c_p\right)_f + \phi_1\left(\rho c_p\right)_{s1} + \phi_2\left(\rho c_p\right)_{s2}$
Thermal conductivity	$k_{hnf}/k_f = \left[\left(\phi_1 k_{s1} + \phi_2 k_{s2}/\phi_{hnf}\right) + 2k_f + 2(\phi_1 k_{s1} + \phi_2 k_{s2}) - 2\phi_{hnf}k_f/\left(\phi_1 k_{s1} + \phi_2 k_{s2}/\phi_{hnf}\right) + 2k_f - 2(\phi_1 k_{s1} + \phi_2 k_{s2}) - \phi_{hnf}k_f\right]$
Electrical conductivity where	$\sigma_{hnf}/\sigma_{nf} = \left[\sigma_{s2} + \sigma_{nf} - 2\phi_2\left(\sigma_{nf} - \sigma_{s2}\right)/\sigma_{s2} + 2\sigma_{nf} + \phi_2\left(\sigma_{nf} - \sigma_{s2}\right)\right]$ $\sigma_{nf}/\sigma_f = \left[\sigma_{s1} + 2\sigma_f - 2\phi_1\left(\sigma_f - \sigma_{s1}\right)/\sigma_{s1} + 2\sigma_f + \phi_1\left(\sigma_f - \sigma_{s1}\right)\right]$
Thermal expansion	$(\rho\beta)_{hnf} = \left\{(1-\phi_2)(1-\phi_1) + (1-\phi_2)\phi_1\left((\rho\beta)_{s1}/(\rho\beta)_f\right)\right\} + \phi_2\left((\rho\beta)_{s2}/(\rho\beta)_f\right)$

2.1. Physical Quantities of Interest. For above model local Nusselt number (Nu_x), the skin friction coefficient (c_f) and Sherwood number are clear as follows:

$$c_f = \frac{\tau_w}{\rho_f u_e^2}, Nu_x = \frac{xq_w}{k_f(T_f - T_\infty)}, Sh_x = \frac{xq_m}{D_B(C_f - C_\infty)}, \tag{17}$$

where

$$\tau_w = \mu_{hnf}\left(\frac{\partial u}{\partial y}\right)_{y=0},$$
$$q_w = -k_{hnf}\left(\frac{\partial T}{\partial y} - q_r\right)\Big|_{y=0},$$
$$q_m = -D_b(C_y)_{y=0}. \tag{18}$$

In dimensional form, we have from above as

$$[\mathrm{Re}_x]^{1/2} C_f = \frac{\mu_{hnf}}{\mu_f} f''(0),$$

$$[\mathrm{Re}_x]^{-1/2} Nu_x = -\frac{k_{hnf}}{k_f}\left(1 + \frac{4}{3}R\right)\theta'(0),$$

$$[\mathrm{Re}_x]^{-1/2} Sh = -\phi'(0). \tag{19}$$

2.2. Idea of HAM for the Model. Here, we used HAM to solve Equations (12)–(14) using boundary conditions (15). The Mathematica software is utilized for this, and the proposed model can be solved using HAM in the following manner:

$$L_{\widehat{f}}\left(\widehat{f}\right) = \widehat{f}''' - \widehat{f}', L_{\widehat{\theta}}\left(\widehat{\theta}\right) = \widehat{\theta}'' - \widehat{\theta}, L_{\widehat{\Phi}}\left(\widehat{\Phi}\right) = \widehat{\Phi}'' - \widehat{\Phi}, \tag{20}$$

where operators are specified as $L_{\widehat{f}}$ and $L_{\widehat{\theta}}$; moreover, we have

$$L_{\widehat{f}}(\gamma_1 + \gamma_2 e^{-\eta} + \gamma_3 e^{\eta}) = 0, L_{\widehat{\theta}}(\gamma_4 e^{-\eta} + \gamma_5 e^{\eta}) = 0, L_{\widehat{\phi}}(\gamma_6 e^{-\eta} + \gamma_7 e^{\eta}) = 0. \tag{21}$$

We also define the operators, such that

$$N_{\widehat{f}}\left[\widehat{f}(\eta;\zeta), \widehat{\theta}(\eta;\zeta), \widehat{\Phi}(\eta;\zeta)\right] = \frac{\mu_{hnf}/\mu_f}{\rho_{hnf}/\rho_f}\widehat{f}_{\eta\eta\eta} + 2\widehat{f}\widehat{f}_{\eta\eta} - \widehat{f}_\eta^2 + 1 - \varepsilon\left(\widehat{f}_\eta - \frac{1}{2}\eta\widehat{f}_{\eta\eta} - 1\right) - \lambda\frac{\beta_{hnf}}{\beta}\left[\widehat{\theta} - \frac{N_r}{\beta_{hnf}/\beta}\widehat{\Phi}\right] + \frac{\sigma_{hnf}/\sigma_f}{\rho_{hnf}/\rho_f}M\widehat{f}_\eta,$$

$$N_{\widehat{\theta}}\left[\widehat{f}(\eta;\zeta), \widehat{\theta}(\eta;\zeta)\right] = \frac{1}{\mathrm{Pr}}\frac{1}{(\rho c_p)_{hnf}/(\rho c_p)_f}\left(\frac{k_{hnf}}{k_f} + \frac{4}{3}R\right)\widehat{\theta}_{\eta\eta} + \widehat{f}\widehat{\theta}_\eta - 2\widehat{f}_\eta\widehat{\theta} + \frac{\varepsilon}{2}\left(\eta\widehat{\theta}_\eta + 3\widehat{\theta}\right) + \frac{\tau_{hnf}}{(\tau/\upsilon)_f}\left[N_b\widehat{\theta}'\widehat{\Phi}' + N_t\widehat{\theta}'^2\right] + \frac{Q(\rho c_p)_f}{(\rho c_p)_{hnf}}\widehat{\theta},$$

$$N_{\widehat{\Phi}}\left[\widehat{\Phi}(\eta;\zeta), \widehat{f}(\eta;\zeta), \widehat{\theta}(\eta;\zeta)\right] = \widehat{\Phi}_{\eta\eta} + Sc\widehat{f}\widehat{\Phi}_\eta - Sc\widehat{f}_\eta\widehat{\Phi} - Sc\frac{\varepsilon}{2}\left(\eta\widehat{\Phi}_\eta + 3\widehat{\Phi}\right) + \frac{N_t}{N_b}\widehat{\theta}''. \tag{22}$$

For Equations (12)–(14), the 0th-order system is shown as follows:

$$(1-\zeta)L_{\widehat{f}}\left[\widehat{f}(\eta;\zeta) - \widehat{f}_0(\eta)\right] = p\hbar_{\widehat{f}}\mathrm{N}_{\widehat{f}}\left[\widehat{f}(\eta;\zeta)\right],$$

$$(1-\zeta)L_{\widehat{\theta}}\left[\widehat{\theta}(\eta;\zeta) - \widehat{\theta}_0(\eta)\right] = p\hbar_{\widehat{\theta}}N_{\widehat{\theta}}\left[\widehat{\theta}(\eta;\zeta), \widehat{f}(\eta;\zeta)\right],$$

$$(1-\zeta)L_{\widehat{\Phi}}\left[\widehat{\Phi}(\eta;\zeta) - \widehat{\Phi}_0(\eta)\right] = p\hbar_{\widehat{\Phi}}N_{\widehat{\Phi}}\left[\widehat{\Phi}(\eta;\zeta), \widehat{f}(\eta;\zeta), \widehat{\theta}(\eta;\zeta)\right], \tag{23}$$

with the BCs are

$$\widehat{f}(\eta;\zeta)\Big|_{\eta=0} = 0, \frac{\partial\widehat{f}(\eta;\zeta)}{\partial\eta}\Big|_{\eta=0} = \lambda + \gamma\frac{\partial^2\widehat{f}(\eta;\zeta)}{\partial\eta^2}\Big|_{\eta=0}, f(0) = 0,$$

$$\frac{k_{nf}}{k_f}\frac{\partial\widehat{\theta}(\eta;\zeta)}{\partial\eta}\Big|_{\eta=0} = -Bi\left(1 - \widehat{\theta}(0)\right), \frac{\partial\widehat{\Phi}(\eta;\zeta)}{\partial\eta}\Big|_{\eta=0} = -N_d\left(1 - \widehat{\Phi}(0)\right)$$

$$\frac{\partial\widehat{f}(\eta;\zeta)}{\partial\eta}\Big|_{\eta=\infty} \longrightarrow 1, \widehat{\theta}(\eta;\zeta)\Big|_{\eta=\infty} \longrightarrow 0, \widehat{\Phi}(\eta;\zeta)\Big|_{\eta=\infty} \longrightarrow 0. \tag{24}$$

While the embedding constraint is $\zeta \in [0,1]$, to regulate for the solution convergence $\hbar_{\widehat{f}}$, $\hbar_{\widehat{\theta}}$, and $\hbar_{\widehat{\Phi}}$ are used. At specific values $\zeta = 0$ and $\zeta = 1$, the following is obtained:

$$\widehat{f}(\eta;1) = \widehat{f}(\eta), \widehat{\theta}(\eta;1) = \widehat{\theta}(\eta), \widehat{\Phi}(\eta;1) = \widehat{\Phi}(\eta). \tag{25}$$

Expand the $\widehat{f}(\eta;\zeta)$, $\widehat{\theta}(\eta;\zeta)$, and $\widehat{\Phi}(\eta;\zeta)$ through Taylor's series for $\zeta = 0$

$$\widehat{f}(\eta;\zeta) = \widehat{f}_0(\eta) + \sum_{n=1}^{\infty} \widehat{f}_n(\eta)\zeta^n,$$

$$\widehat{\theta}(\eta;\zeta) = \widehat{\theta}_0(\eta) + \sum_{n=1}^{\infty} \widehat{\theta}_n(\eta)\zeta^n,$$

$$\widehat{\Phi}(\eta;\zeta) = \widehat{\Phi}_0(\eta) + \sum_{n=1}^{\infty} \widehat{\Phi}_n(\eta)\zeta^n,$$

$$\widehat{f}_n(\eta) = \frac{1}{n!}\frac{\partial \widehat{f}(\eta;\zeta)}{\partial \eta}\bigg|_{p=0},$$

$$\widehat{\theta}_n(\eta) = \frac{1}{n!}\frac{\partial \widehat{\theta}(\eta;\zeta)}{\partial \eta}\bigg|_{p=0},$$

$$\widehat{\Phi}_n(\eta) = \frac{1}{n!}\frac{\partial \widehat{\Phi}(\eta;\zeta)}{\partial \eta}\bigg|_{p=0}. \tag{26}$$

While BCs are

$$\widehat{f}(0) = 0, \widehat{f}'(0) = \lambda + \gamma \widehat{f}''(0),$$

$$\frac{k_{hnf}}{k_f}\widehat{\theta}'(0) = -Bi\left(1 - \widehat{\theta}(0)\right), \widehat{\Phi}'(0) = -N_d\left(1 - \widehat{\Phi}(0)\right),$$

$$\widehat{f}'(\eta) \longrightarrow 0, \widehat{\theta}(\eta) \longrightarrow 0, \widehat{\Phi}(\eta) \longrightarrow 0\eta \longrightarrow \infty.$$

$$\begin{aligned}\mathfrak{R}_n^{\widehat{f}}(\eta) = {} & \frac{\mu_{hnf}/\mu_f}{\rho_{hnf}/\rho_f}\widehat{f}'''_{n-1} + 2\sum_{j=0}^{w-1}\widehat{f}_{w-1-j}\widehat{f}''_j - \widehat{f}'^2_{n-1} \\ & + 1 - \varepsilon\left(\widehat{f}'_{n-1} - \frac{1}{2}\eta\widehat{f}''_{n-1} - 1\right) + \frac{\sigma_{hnf}/\sigma_f}{\rho_{hnf}/\rho_f}M\widehat{f}'_{n-1} \\ & - \lambda\left[\widehat{\theta}_{n-1} - N_r\widehat{\Phi}_{n-1}\right],\end{aligned}$$

$$\begin{aligned}\mathfrak{R}_n^{\widehat{\theta}}(\eta) = {} & \frac{1}{\Pr}\frac{1}{(\rho c_p)_{hnf}/(\rho c_p)_f}\left(\frac{k_{hnf}}{k_f} + \frac{4}{3}R\right)\left(\widehat{\theta}''_{n-1}\right) \\ & + \sum_{j=0}^{w-1}\widehat{\theta}'_{w-1-j}\widehat{f}_j - 2\sum_{j=0}^{w-1}\widehat{\theta}_{w-1-j}\widehat{f}'_j + \\ & \frac{\varepsilon}{2}\left(\eta\widehat{\theta}'_{n-1} + 3\widehat{\theta}_{n-1}\right) + \frac{\tau_{hnf}}{(\tau/\upsilon)_f}\left[N_b\sum_{j=0}^{w-1}\widehat{\theta}'_{w-1-j}\widehat{\Phi}'_j + N_t\widehat{\theta}'^2_{n-1}\right] \\ & + \frac{Q(\rho c_p)_f}{(\rho c_p)_{hnf}}\widehat{\theta}_{n-1},\end{aligned}$$

$$\begin{aligned}\mathfrak{R}_n^{\widehat{\Phi}}(\eta) = {} & \widehat{\Phi}''_{n-1} + Sc\sum_{j=0}^{w-1}\widehat{f}_{w-1-j}\widehat{\Phi}'_j - Sc\sum_{j=0}^{w-1}\widehat{f}'_{w-1-j}\widehat{\Phi}_j \\ & + \frac{N_t}{N_b}\widehat{\theta}''_{n-1} + Sc\frac{\varepsilon}{2}\left(\eta\widehat{\Phi}'_{n-1} + 3\widehat{\Phi}_{n-1}\right).\end{aligned} \tag{27}$$

While

$$\chi_n = \begin{cases} 0, & \text{if } n \le 1, \\ 1, & \text{if if } n > 1. \end{cases} \tag{28}$$

3. Outcomes with Discussion

In the following discussion section, the outcomes of various parametric quantity on velocity, concentration profiles, and temperature are shown graphically and discussed. These parameters are unsteadiness parameter, buoyancy ratio parameter, magnetic parameter, thermal radiation parameter, Lewis number, mixed convection parameter, Prandtl number and thermophorotic parameter, and Brownian motion parameter. The geometry of the problem is shown in Figure 1. It can be seen that when the magnetic parameter M assigns maximum values, the velocity distribution retains its declining tendency as shown in Figure 2. There is a periodic oscillation velocity with diminishing amplitude while the magnetic force produces a resistive nature force known as the Lorentz force which controls the flow of fluid particles. As a result, to demonstrate the value of reducing the velocity of moving particles, the effect of the unsteadiness parameter on ε the nanofluid velocity profile has seen in Figure 3. Because of the acceleration situation, $(\varepsilon > 0)$ brings down rate of fluid flow and a narrower momentum boundary barrier thickness; the behavior occurs. The velocity profile reduces for the higher acceleration.

Figure 4 illustrates the influence of the buoyancy ratio parameter on velocity drawings and also increasing levels of N_r; there is a noticeable increase in velocity. This increase in velocity drawings is more noticeable in stable condition than in the unsteadness situation. Figure 5 shows the effect of λ_1 on $f'(\eta)$. From Figure 5, it can be expected that $f'(\eta)$ has greater values of λ_1. Physically, this is because of the larger values of buoyancy force. The impact of heat generation/absorption on the temperature is plotted in Figure 6. The temperature of the fluid and the thickness of the thermal boundary level are both increased when a heat source $(Q > 0)$ is used. The heat sink $(Q < 0)$, on the other hand, lowers the fluid's temperature and thins the thermal boundary level thickness.

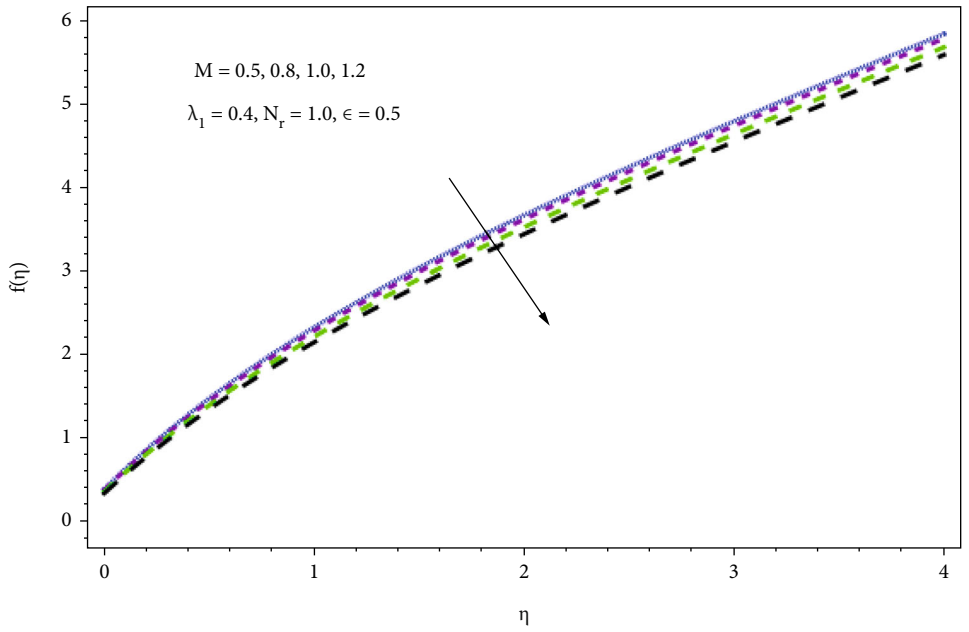

Figure 2: Illustration of the effect of M on $f'(\eta)$.

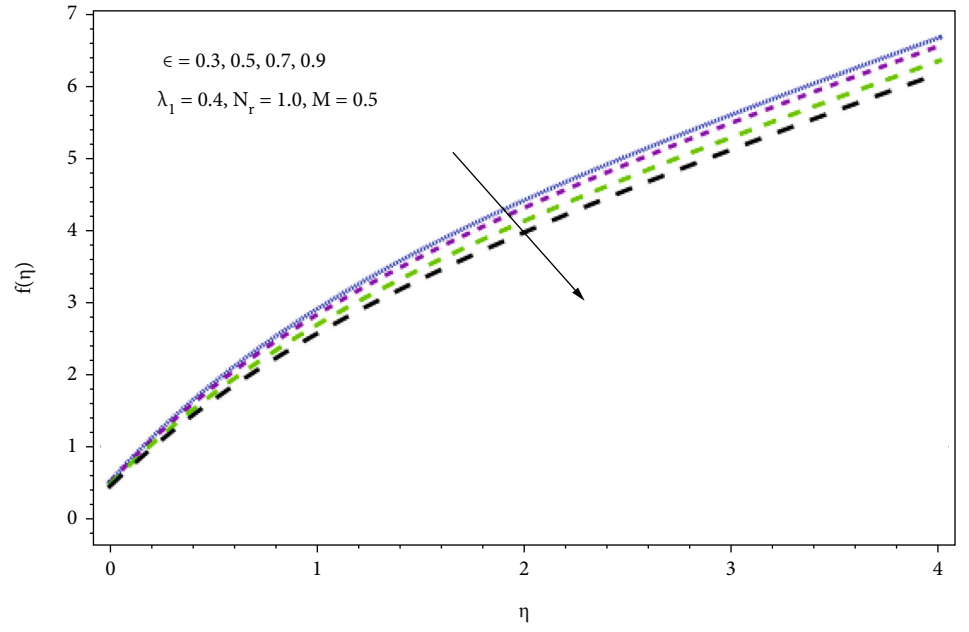

Figure 3: Representation of the effect of ε on $f'(\eta)$.

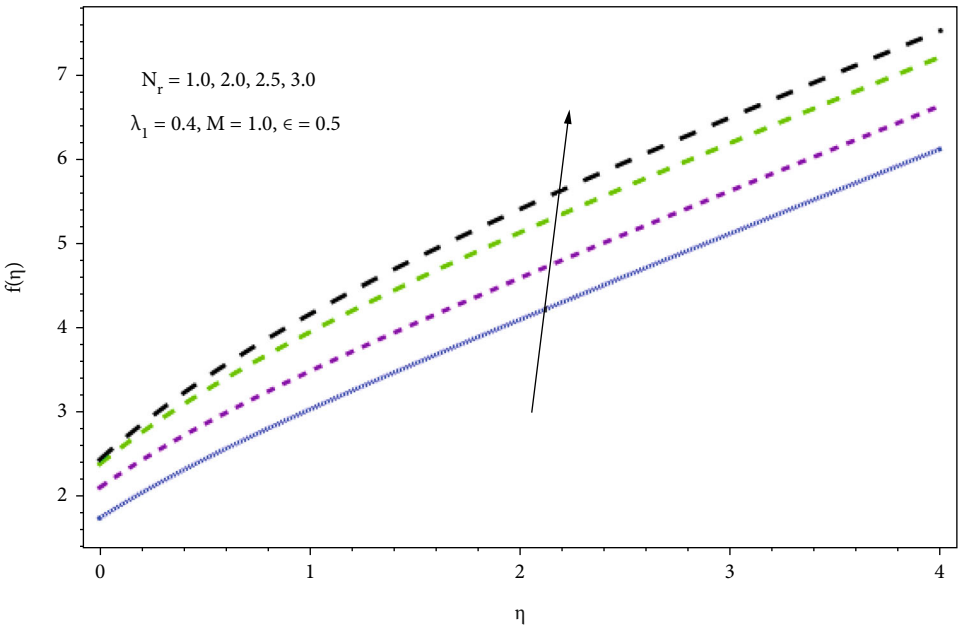

Figure 4: Illustration of the effect of N_r on $f'(\eta)$.

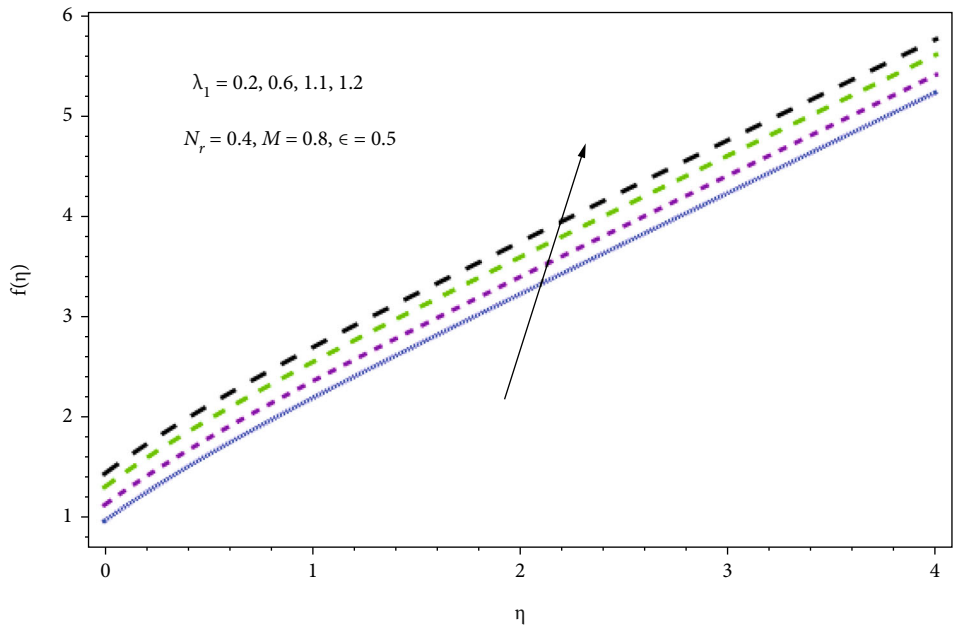

Figure 5: Illustration of the effect of λ_1 on $f'(\eta)$.

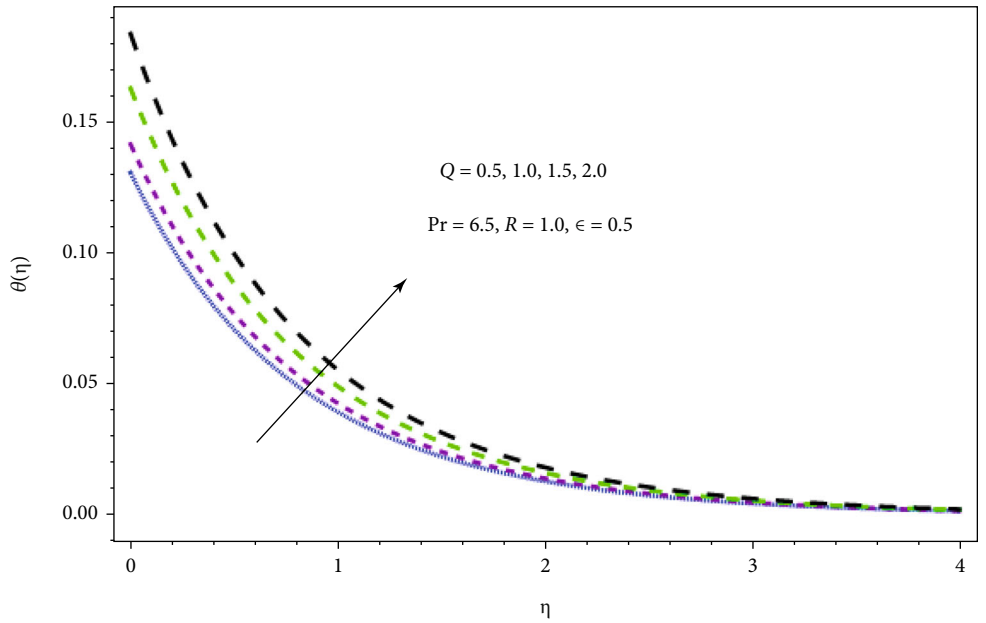

Figure 6: Illustration of the effect of Q on $\theta(\eta)$.

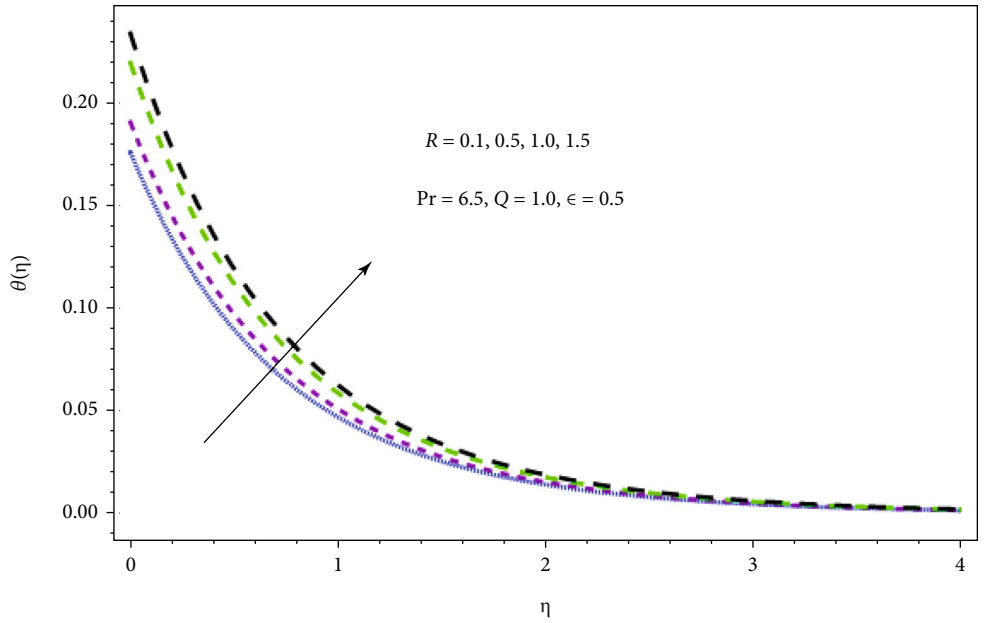

Figure 7: Representation of the effect of R on $\theta(\eta)$.

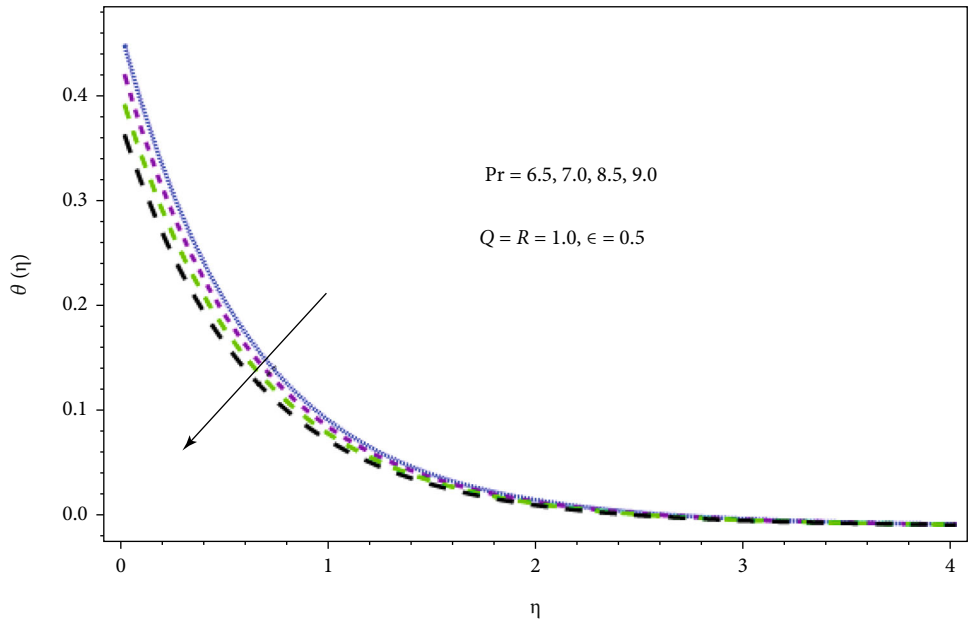

Figure 8: Graphical view to show the effect of Pr on $\theta(\eta)$.

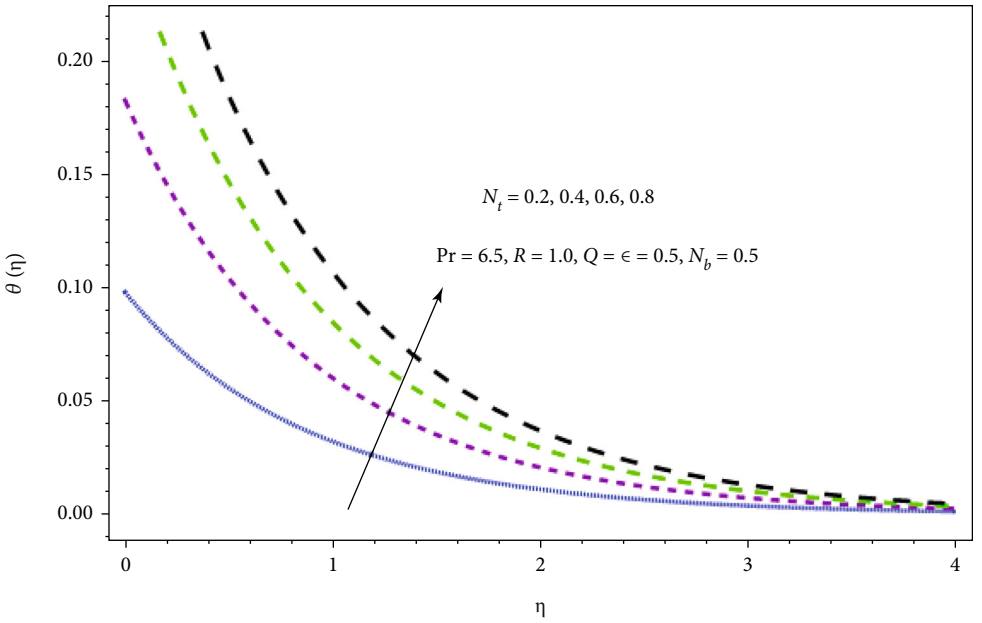

Figure 9: Illustration of the effect of N_t on $\theta(\eta)$.

To denote $(Q = 0)$, the lack of heat generation or absorption, the increase in thermal radiation raises the temperature but lowers the concentration profiles, as seen in Figure 7. This is because an increase in thermal radiation gives to a greater extent heat to the hybrid nanofluid, resulting in a rise in temperature and the thickness of the thermal boundary layer. Physically, radiative aspect creates the Brownian motion of minute ingredients faster than normal; thus, random migrated particles strike with one another, and the caused frictional energy transforms it to thermal energy. The effect from the Prandtl number along the temperature profile has seen in Figure 8. By increasing the Prandtl number, the fluid's thermal conductivity decreases. This fact is due to inverse relation of Pr with thermal diffusivity, and it is well-known fact that the fluid with higher values of Pr has weaker thermal diffusion so that the temperature declines. Figures 9 and 10 demonstrate the consequence of the thermophoresis parametric quantity (N_t) along the thermal profile. When the thermophoresis parametric quantity is increased which enhance the behavior of the system,

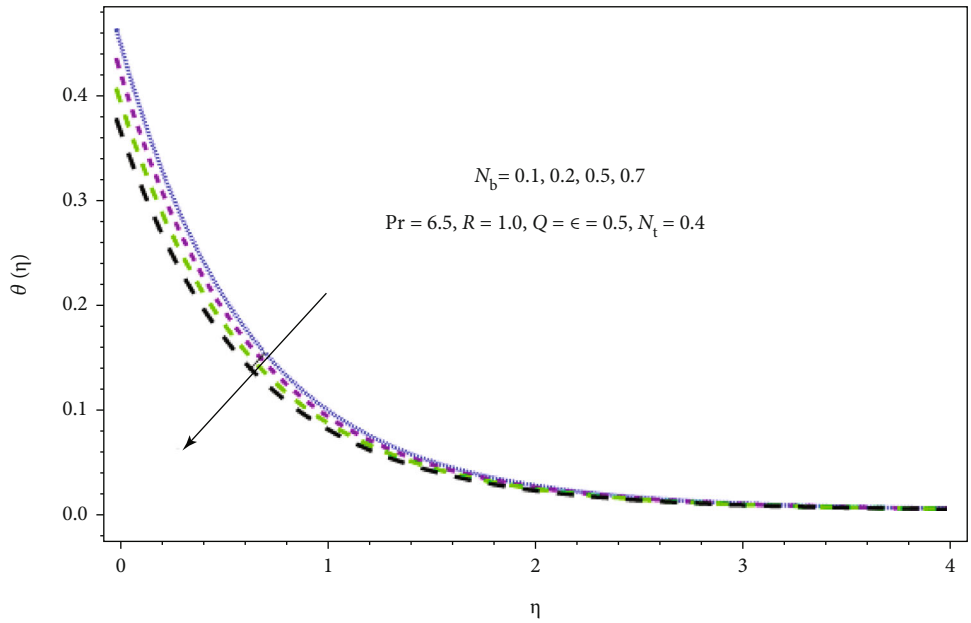

Figure 10: Graphical view of the effect of N_b on $\theta(\eta)$.

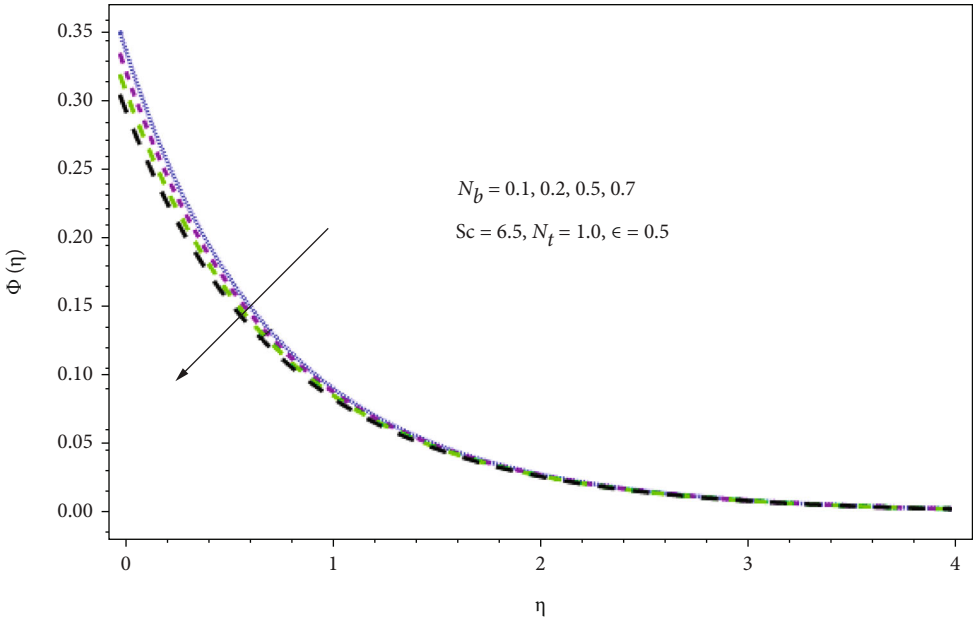

Figure 11: Representation of the effect of N_b on $\Phi(\eta)$.

thermophoresis effect is associated with movement of nanoparticles from a hot wall to a cold wall, and since it is generated by temperature gradients, it creates a fast flow away from the moving plate; thus, more fluid is heated away from the surface, and this leads to an increase in the temperature within the thermal boundary layer. Figure 10 demonstrates the consequence of the Brownian diffusion parameter (N_b) on the thermal profile. Physically, the imperfect nature of the Brownian motion parametric quantity enables heating the physical setup. This heating causes nanoparticles to be transferred from the cooler stretched sheet area to the quiescent fluid zone. Because the particles migrate from a high up to a low concentration part, an increase in the Brownian motion parameter N_b and $\Phi(\eta)$ leads decrease in the fluid concentration gradient, as seen in Figure 11.

The Brownian motion is the movement of fluid particles from higher to lower concentration so increases in the thermophoresis parameter (N_t) produce a huge rise in the concentration dispersion of the fluid flow $\Phi(\eta)$, which meet to zero at the boundary level, as shown in Figure 12. A minor

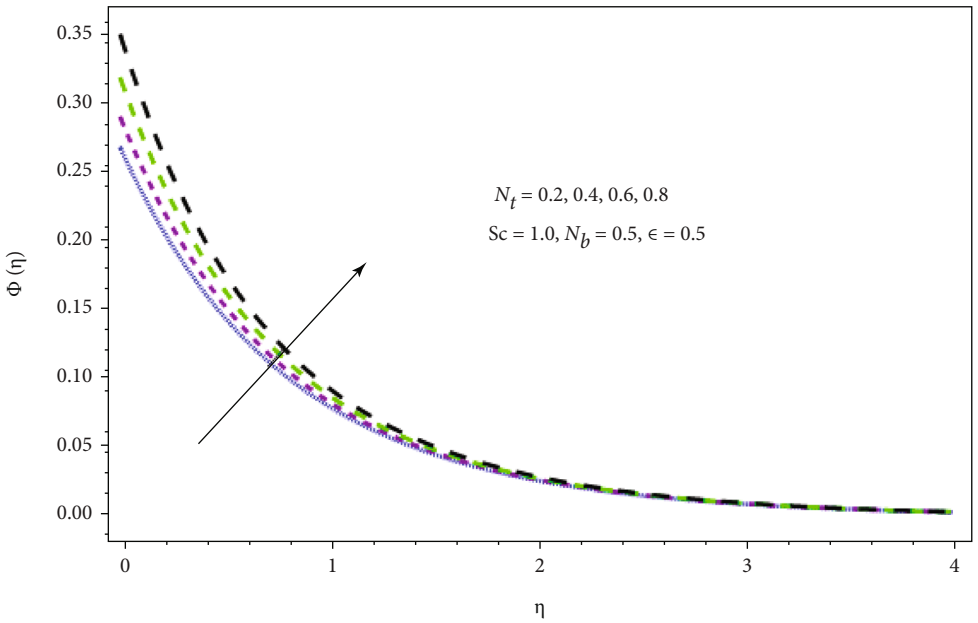

Figure 12: Illustration of the effect of N_t on $\Phi(\eta)$.

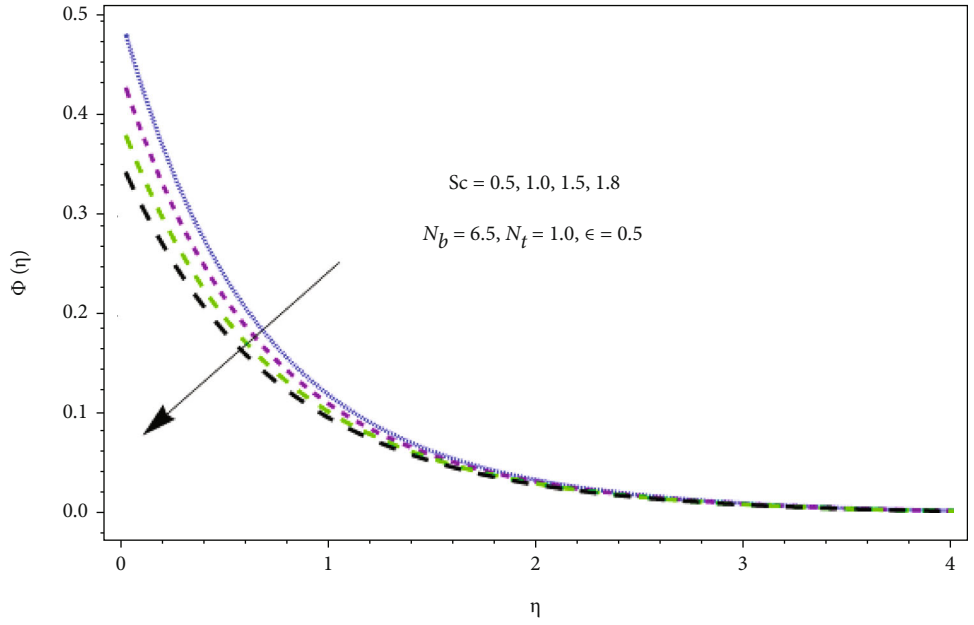

Figure 13: Representation of the effect of*Sc* on $\Phi(\eta)$.

Table 4: Representation of the influence of different physical factors on skin friction $[\mathrm{Re}_x]^{1/2}C_f = (\mu_{hnf}/\mu_f)f''(0)$.

λ_1	N_r	M	ε	$\left(\mu_{hnf}/\mu_f\right)f''(0)$
0.3	0.3	0.5	0.3	1.6735237
0.5				1.4321803
1.0				1.2307539
	0. 3			2.2316739
	0.5			2.1317693
	1.0			2.1038033
		0.5		1.3156063
		1.0		1.4367109
		1.5		1.4837333
			0.3	2.1396853
			0.5	2.1946379
			0.7	2.2453103

Table 5: Illustration of the influence of different physical factors over Nusselt number $[\mathrm{Re}_x]^{-1/2}Nu_x = -(k_{hnf}/k_f)(1 + (4/3)R)\theta'(0)$.

R	Q	Pr	N_t	N_b	ε	$-\left(k_{hnf}/k_f\right)(1 + 4/3R)\theta'(0)$
0.8	-0.5	7.5	0.7	0.5	0.3	1.8363904
1.0						1.7214318
1.2						1.3274134
	-0.5					1.3435906
	-1.0					1.1643153
	-1.5					1.0366173
		7.5				1.3453139
		8.5				1.6437058
		9.5				1.8467893
			0.2			1.2327811
			0.4			1.1364383
			0.6			1.0953647
				0.3		1.4735333
				0.7		1.3794531
				0.9		1.2393407
					0.3	1.6157203
					0.5	1.7240367
					0.7	1.8090526

change in the thermophoresis parameter causes the fluid particles to move quickly, releasing surplus heat energy and causing a huge rise in the concentration dispersion. As a result, with an increase in the value of (N_t), Figure 12 indicates a considerable rise in the concentration dispersion. Figure 13 also shows the influence of the Schmidt number on the concentration dispersion. It is noticed that for larger values of *Sc*, the fluid concentration decreases. This fact is quite similar with that of Prandtl number impact on temperature. Actually, *Sc* has inverse relation with mass diffusivity; therefore, larger values of *Sc* correspond thinner concentration boundary layer.

Table 6: Illustration of the influence of different physical factors over Sherwood number $\mathrm{Re}\, s^{-1/2}\mathrm{Sh}_x = -\phi'(0)$..

N_t	N_b	Le	$-\phi'(0)$
0.2	0.3	2.0	2.1493731
0.4			2.1730691
0.6			2.2393414
	0.3		2.3518701
	0.7		2.4504103
	0.9		2.4993798
		2.0	2.5623087
		3.3	2.6573919
		4.0	2.6935286

4. Discussion on Tabulated Results

Table 4 shows that C_f is increased when the values of ε, M are increased. The C_f is decreased, when the values of λ_1, N_r are increased. Table 5 shows that Nu_x is increased when the values of R, Q, N_b, N_t are increased. The Nu_x is decreased, when the values of Pr are increased. Table 6 shows that *Sh* is decreased, when the values of N_b, N_t, Le are increased. Table 1 shows the very excellent agreement of the HAM and ND solve solution by computer-based package Mathematica 11.1.0.

5. Conclusions

In this research work, the uniform mixed convectional with the combined consequences of thermal radiation and heat generation/absorption along the magnetohydrodynamic (MHD) flow of hybrid nanofluid via a convectional heated the stretching/shrinking surface is studied. Brownian motion and thermophoresis were incorporated using the Buongiorno model. We came at the following key conclusions based on our findings with various factors in this study:

(i) Increasing the combined convection and buoyancy ratio parameters improved nanofluid flow properties

(ii) It is well established that an increase in the unsteadiness and magnetic parameters result in a decrease in the velocity profile

(iii) Consequently, a rise in the thermophorotic parameter, radiation parameter, or Brownian motion parameter means an increase in the temperature profile

(iv) It is noticed that the increase of the Prandtl number decreases the temperature profile

(v) Increases in the values of the thermophoretic parameter and Brownian motion parameter have an inverse influence on the concentration profile

(vi) The $\Phi(\eta)$ displays lessening tendency for rising values of *Le*

(vii) Skin friction is augmented when the values of ε, M are improved. When the values of λ_1, N_r is enlarged, C_f is reduced

(viii) Nusselt number is improved when the values R, Q, N_b, N_t are increased. The Nu_x is reduced, when the values of Pr are augmented

(ix) Sherwood number is declined, when the values of N_b, N_t, Le are enlarged

Nomenclature

u and v: Components of velocity along x- and y-axes (m/s)
u_w: Stretching/shrinking velocity (m/s)
T_1: Ambient temperature (K)
h_f: Heat transfer coefficient
μ_{hnf}: ($kgm^{-1}s^{-1}$) Viscosity of hybrid nanofluid
Re_x: Reynolds number
θ: Dimensionless temperature
ρ_s: The density of the nanoparticle (kgm^{-3})
k_s: Nanoparticle thermal conductivity ($Wm^{-1}K^{-1}$)
ψ: Stream function
M: Magnetic parameter
H_1: Velocity slip factor
λ: Ratio of velocity parameter and heat
Nu_x: Local Nusselt number
f': Dimensionless velocity
v: Kinematic viscosity (m^2s^{-1})
q_m: Wall mass flux
q_r: Rosseland approximation
ϕ: Nanoparticle solid volume fraction
k^*: Coefficient of mean absorption
C_f: Plate concentration
C_∞: Concentration of ambient
h_s: Mass transfer coefficient
N_b: Brownian motion parameter
x, y: Cartesian coordinate axis
u_e: Strength of the stagnation flow
T_0: Reference temperature (K)
ρ_{hnf}: Hybrid nanofluid density (kgm^{-3})
$(\rho c_p)_{hnf}$: Hybrid nanofluid volumetric heat capacity ($m^2s^{-2}K^{-1}$)
H: Initial value of the velocity slip factor
c_p: Constant pressure of heat capacity
ρ_f: Base fluid density (kgm^{-3})
k_f: Base fluid thermal conductivity ($Wm^{-1}K^{-1}$)
ε: Unsteadiness parameter
Φ: Dimensionless concentration
Pr: Prandtl number
Q: Source/sink parameter
c_f: Skin friction coefficient
T: Temperature of fluid (K)
μ_f: Dynamic viscosity ($kgm^{-1}s^{-1}$)
τ_w: Wall shear stress
q_w: Transportation of heat
σ^*: Stefan-Boltzmann constant
k_1: Porosity parameter
R: Thermal radiation parameter
C_w: Wall concentration
Bi: Biot number
N_t: Thermophoretic parameter.

Data Availability

No data were used to support this study.

Conflicts of Interest

The authors declare that they have no conflicts of interest.

References

[1] W. Jamshed and A. Aziz, "Cattaneo–Christov based study of TiO_2–CuO/EG Casson hybrid nanofluid flow over a stretching surface with entropy generation," *Applied Nanoscience*, vol. 8, no. 4, pp. 685–698, 2018.

[2] S. S. Ghadikolaei, M. Gholinia, M. E. Hoseini, and D. D. Ganji, "Natural convection MHD flow due to MoS_2–Ag nanoparticles suspended in $C_2H_6O_2$–H_2O hybrid base fluid with thermal radiation," *Journal of the Taiwan Institute of Chemical Engineers*, vol. 97, pp. 12–23, 2019.

[3] S. S. Ghadikolaei, M. Yassari, H. Sadeghi, K. Hosseinzadeh, and D. D. Ganji, "Investigation on thermophysical properties of Tio_2-Cu/H_2O hybrid nanofluid transport dependent on shape factor in MHD stagnation point flow," *Powder Technology*, vol. 322, pp. 428–438, 2017.

[4] N. Ahmed, F. Saba, U. Khan et al., "Spherical shaped (Ag –Fe_3O_4/H_2O) hybrid nanofluid flow squeezed between two riga plates with nonlinear thermal radiation and chemical reaction effects," *Energies*, vol. 12, no. 1, p. 76, 2019.

[5] S. Manjunatha, B. A. Kuttan, S. Jayanthi, A. Chamkha, and B. J. Gireesha, "Heat transfer enhancement in the boundary layer flow of hybrid nanofluids due to variable viscosity and natural convection," *Heliyon*, vol. 5, no. 4, article e01469, 2019.

[6] S. Suresh, K. Venkitaraj, P. Selvakumar, and M. Chandrasekar, "Synthesis of Al_2O_3-Cu/water hybrid nanofluids using two step method and its thermo physical properties," *Colloids and Surfaces A: Physicochemical and Engineering Aspects*, vol. 388, no. 1-3, pp. 41–48, 2011.

[7] S. Suresh, K. Venkitaraj, P. Selvakumar, and M. Chandrasekar, "Effect of Al_2O_3-Cu/water hybrid nanofluid in heat transfer," *Experimental Thermal and Fluid Science*, vol. 38, pp. 54–60, 2012.

[8] S. Suresh, K. P. Venkitaraj, M. S. Hameed, and J. Sarangan, "Turbulent heat transfer and pressure drop characteristics of dilute water based Al_2O_3Cu hybrid nanofluids," *Journal of Nanoscience and Nanotechnology*, vol. 14, pp. 2563–2572, 2014.

[9] S. P. A. Devi and S. S. U. Devi, "Numerical investigation of hydromagnetic hybrid Cu – Al_2O_3/water nanofluid flow over a permeable stretching sheet with suction," *International Journalof Nonlinear Sciences and Numerical Simulation*, vol. 17, no. 5, pp. 249–257, 2016.

[10] S. S. U. Devi and S. P. A. Devi, "Numerical investigation of three-dimensional hybrid Cu–Al_2O_3/water nanofluid flow over a stretching sheet with effecting Lorentz force subject to Newtonian heating," *Canadian Journal of Physics*, vol. 94, no. 5, pp. 490–496, 2016.

[11] T. Hayat and S. Nadeem, "Heat transfer enhancement with Ag-CuO/water hybrid nanofluid," *Results in Physics*, vol. 7, pp. 2317–2324, 2017.

[12] N. A. Zainal, R. Nazar, K. Naganthran, and I. Pop, "Unsteady stagnation point flow of hybrid nanofluid past a convectively heated stretching/shrinking sheet with velocity slip," *Mathematics*, vol. 8, no. 10, p. 1649, 2020.

[13] Y. S. Daniel, Z. A. Aziz, Z. Ismail, and F. Salah, "Double stratification effects on unsteady electrical MHD mixed convection flow of nanofluid with viscous dissipation and Joule heating," *Journal of Applied Research and Technology*, vol. 15, no. 5, pp. 464–476, 2017.

[14] H. Xie, B. Jiang, B. Liu, Q. Wang, J. Xu, and F. Pan, "An investigation on the tribological performances of the SiO_2/ MoS_2 hybrid nanofluids for magnesium alloy-steel contacts," *Nanoscale Research Letters*, vol. 11, no. 1, pp. 329–336, 2016.

[15] J. Prakash, A. Sharma, and D. Tripathi, "Thermal radiation effects on electroosmosis modulated peristaltic transport of ionic nanoliquids in biomicrofluidics channel," *Journal of Molecular Liquids*, vol. 249, pp. 843–855, 2018.

[16] T. Hayat, K. Muhammad, M. Farooq, and A. Alsaedi, "Melting heat transfer in stagnation point flow of carbon nanotubes towards variable thickness surface," *AIP Advances*, vol. 6, no. 1, article 015214, 2016.

[17] K. Muhammad, T. Hayat, S. A. Shehzad, and A. Alsaedi, "Viscous dissipation and Joule heating effects in MHD 3D flow with heat and mass fluxes," *Results in Physics*, vol. 8, pp. 365–371, 2018.

[18] K. L. Hsiao, "Stagnation electrical MHD nanofluid mixed convection with slip boundary on a stretching sheet," *Applied Thermal Engineering*, vol. 98, no. 5, pp. 850–861, 2016.

[19] B. Mahanthesh, B. J. Gireesha, and R. S. R. Gorla, "Nonlinear radiative heat transfer in MHD three-dimensional fow of water based nanofuidover a non-linearly stretching sheet with convective boundary condition," *Journal of the Nigerian Mathematical Society*, vol. 35, pp. 78–98, 2016.

[20] S. Murtaza, M. Iftekhar, F. Ali, and I. Khan, "Exact analysis of non-linear electro-osmotic flow of generalized Maxwell nanofluid: applications in concrete based nano-materials," *IEEE Access*, vol. 8, pp. 96738–96747, 2020.

[21] N. Mezouar and S. M. Boulaaras, "Global existence and decay of solutions of a singular nonlocal viscoelastic system with damping terms," *Topological Methods in Nonlinear Analysis*, vol. 56, no. 1, pp. 1–312, 2020.

[22] J. Ahmad, F. Ali, S. Murtaza, and I. Khan, "Caputo time fractional model based on generalized Fourier's and Fick's laws for Jeffrey nanofluid: applications in automobiles," *Mathematical Problems in Engineering*, vol. 2021, Article ID 4611656, 12 pages, 2021.

[23] S. M. Boulaaras, A. Choucha, A. Zara, M. Abdalla, and B. B. Cheri, "Global existence and decay estimates of energy of solutions for a new class of -Laplacian heat equations with logarithmic nonlinearity," *Journal of Function Spaces*, vol. 2021, Article ID 5558818, 11 pages, 2021.

[24] F. Ali, S. Murtaza, N. A. Sheikhand, and I. Khan, "Heat transfer analysis of generalized Jeffery nanofluid in a rotating frame: Atangana-Balaenu and Caputo-Fabrizio fractional models," *Chaos, Solitons & Fractals*, vol. 129, pp. 1–15, 2019.

[25] S. Boulaaras and M. Haiour, "The finite element approximation of evolutionary Hamilton-Jacobi-Bellman equations with nonlinear source terms," *Indagationes Mathematicae*, vol. 24, no. 1, pp. 161–173, 2013.

[26] S. Toualbia, A. Zaraï, and S. Boulaaras, "Decay estimate and non-extinction of solutions of p-Laplacian nonlocal heat equations," *AIMS Mathematics*, vol. 5, no. 3, pp. 1663–1679, 2020.

[27] S. Boulaaras, "Some new properties of asynchronous algorithms of theta scheme combined with finite elements methods for an evolutionary implicit 2-sided obstacle problem," *Mathematical Methods in the Applied Sciences*, vol. 40, no. 18, pp. 7231–7239, 2017.

[28] N. Acharya, R. Bag, and P. K. Kundu, "On the impact of nonlinear thermal radiation on magnetized hybrid condensed nanofluid flow over a permeable texture," *Applied Nanoscience*, vol. 10, no. 5, pp. 1679–1691, 2020.

[29] N. Acharya, "On the flow patterns and thermal behaviour of hybrid nanofluid flow inside a microchannel in presence of radiative solar energy," *Journal of Thermal Analysis and Calorimetry*, vol. 141, no. 4, pp. 1425–1442, 2020.

[30] N. Acharya and F. Mabood, "On the hydrothermal features of radiative Fe_3O_4–graphene hybrid nanofluid flow over a slippery bended surface with heat source/sink," *Journal of Thermal Analysis and Calorimetry*, vol. 143, no. 2, pp. 1273–1289, 2021.

[31] N. Acharya, "Spectral quasi linearization simulation on the radiative nanofluid spraying over a permeable inclined spinning disk considering the existence of heat source/sink," *Applied Mathematics and Computation*, vol. 411, article 126547, 2021.

Hindawi
Advances in Mathematical Physics
Volume 2022, Article ID 8371954, 9 pages
https://doi.org/10.1155/2022/8371954

Research Article

Theoretical Analysis of Two Collinear Cracks in an Orthotropic Solid under Linear Thermal Flux and Linear Mechanical Load

Bing Wu,[1] **Bao-Yin Zhu**,[2] **Hao-Meng Song**,[1] **and Qiong-Ao Huang**[3]

[1]*Technology Innovation Center for Testing and Evaluation in Civil Engineering of Hebei Province, Hebei University, Baoding, Hebei 071002, China*
[2]*Suzhou Nuclear Power Research Institute, Xihua Road 1688, Suzhou 215004, China*
[3]*South China Research Center for Applied Mathematics and Interdisciplinary Studies, South China Normal University, Guangzhou 510631, China*

Correspondence should be addressed to Qiong-Ao Huang; huangqiongao@m.scnu.edu.cn

Received 27 August 2021; Revised 7 November 2021; Accepted 2 December 2021; Published 9 February 2022

Academic Editor: David Carf

This paper studies the problem of a cracked orthotropic solid subject to linear thermal flux and linear mechanical load. The proposed extended partially insulated crack model is employed to simulate two collinear cracks. Taking advantage of Fourier transform technique and superposition theory, the closed form of some physical quantities and fracture parameters is obtained. Some simple examples are employed to demonstrate dimensionless thermal conductivity (R_c) between the upper and below crack regions, and the proposed coefficient (ε) has great effects on some physical quantities and fracture parameters.

1. Introduction

Multicomponent composite materials are widely used in the material industry. However, considering the complex factors involving working environment, internal and external loads, and production process, it is inevitable to contain a series of various cracks in these solids. The appearances of different kinds of cracks will reduce the capacity of cracked structures and even bring about severe accidents. Therefore, it is vital to do some research on fracture analysis of a cracked solid by utilizing the theory of thermal elasticity for the purpose of safety [1–3]. With the rapid growth of thermoelasticity theory, a great deal of treatises and papers was published to investigate fracture characters of cracked solids [4–6]. The fracture parameters of an orthotropic material containing a central crack under heat flow were obtained by Tsai [7]. The closed form of fracture parameters of cracked orthotropic solids was calculated by Ju and Rowlands [8]. The closed form of some physical quantities of two collinear cracks was studied by Chen and Zhang [9]. The transient thermal problem of a cracked orthotropic plate was taken into account by Noda [10]. Some physical quantities of a cracked orthotropic semi-infinite medium were given by Rizk [11]. On the other hand, the thermoelastic problems of orthotropic functionally graded solids brought about the widespread attention. For example, the fracture parameters of orthotropic functionally graded solids under mechanical load were given explicitly by Kim and Paulino [12]. The problem of a cracked solid subject to plane temperature-step waves was investigated by Brock [13]. The equivalent domain integral was formulated to study the fracture problems subject to thermal stresses by Dag [14]. The problems of cracked orthotropic solids subject to symmetrical thermomechanical loads with application of Fourier transform technique (FTT) and superposition principle were studied by Wu et al. [15].

Subject to thermal load, the analysis of fracture behavior for cracked solids which were often regarded as orthotropic or isotropic has generated enormous publicity [16–20]. To

simulate two collinear cracks, a partially insulated crack model prevailed [21–23].

$$Q_{1c} = -h_c \Delta T, \tag{1}$$

where the definitions of Q_{1c}, h_c, and ΔT have been given in detail [3]. The case of $h_c \longrightarrow 0$ or $h_c \longrightarrow \infty$ denotes a fully thermally impermeable or permeable state.

The following extended partially insulated crack model is also put forward by virtue of mathematical intuition.

$$Q_{1c} = -h_c \Delta T + \varepsilon Q_1, \tag{2}$$

where Q_1 presents initial heat flux. The coefficient ε is considered a constant. Whether it is negative or positive is mainly relies on the portion of thermal flux and mechanical load. Clearly, the crack model proposed in (2) returns to (1) when $\varepsilon = 0$.

The reasons of introducing constant εQ_1 in (2) are as follows. First, the value of h_c does not precisely address the cracks with thermal resistance. Second, the constant εQ_1, which is introduced as an adjustment factor, conforms to the complex situation and meets the abnormal state of crack surface.

This paper employs an extended partially insulated crack model to discuss two collinear cracks under linear thermal flux and linear mechanical load. The thermoelastic field is given in explicit form based on the proposed extended partially insulated crack model, Fourier transform, and superposition theory. The results show the effects of dimensionless thermal conductivity (R_c) between the upper and below crack regions and the proposed coefficient (ε) on Q_{1c} and K_{II} and S. It is revealed the boundary conditions of crack surface, thermal properties of crack, and the raised coefficient should be paid attention to the analysis of crack growth under thermal load in numerical results.

2. Problem Statement

Two collinear cracks in an orthotropic solid are taken into account as shown in Figure 1. They are located at $a < |x| < b$.

Making use of the state of plane stress [3], we obtain

$$\sigma_x = c_{11} \frac{\partial u}{\partial x} + c_{12} \frac{\partial v}{\partial y} - \beta_1 T, \tag{3}$$

$$\sigma_y = c_{12} \frac{\partial u}{\partial x} + c_{22} \frac{\partial v}{\partial y} - \beta_2 T, \tag{4}$$

$$\tau_{xy} = c_{66} \left[\frac{\partial u}{\partial y} + \frac{\partial v}{\partial x} \right], \tag{5}$$

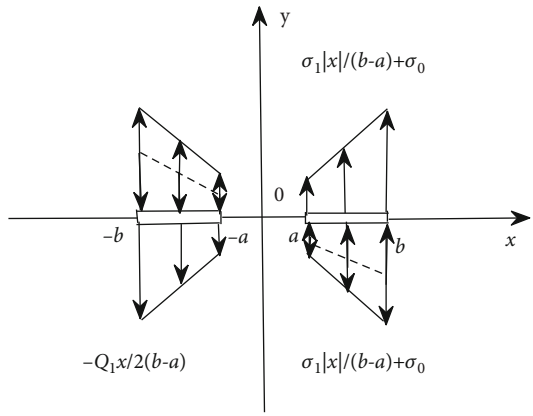

Figure 1: Two collinear cracks subject to linear thermal flux and linear mechanical load.

where

$$\begin{aligned} c_{11} &= \frac{E_{xx}}{1 - \nu_{xy}\nu_{yx}}, \\ c_{22} &= \frac{E_{yy}}{1 - \nu_{xy}\nu_{yx}}, \\ c_{12} &= \frac{E_{xx}\nu_{yx}}{1 - \nu_{xy}\nu_{yx}} = \frac{E_{yy}\nu_{xy}}{1 - \nu_{xy}\nu_{yx}}, \\ \begin{bmatrix} \beta_1 \\ \beta_2 \end{bmatrix} &= \begin{bmatrix} c_{11} & c_{12} \\ c_{12} & c_{22} \end{bmatrix} \begin{bmatrix} \alpha_{xx} \\ \alpha_{yy} \end{bmatrix}, \end{aligned} \tag{6}$$

where the definitions of u, v, σ_x, σ_y, $\tau_{xy}T$, ν_{xx}, $\nu_{yy}E_{xx}$, E_{yy}, $c_{66} = G_{xy}$, α_{xx}, and α_{yy} have been given in [3].

$$\begin{aligned} \frac{\partial \sigma_x}{\partial x} + \frac{\partial \tau_{xy}}{\partial y} &= 0, \\ \frac{\partial \tau_{xy}}{\partial x} + \frac{\partial \sigma_y}{\partial y} &= 0. \end{aligned} \tag{7}$$

One obtains

$$c_{11} \frac{\partial^2 u}{\partial x^2} + c_{66} \frac{\partial^2 u}{\partial y^2} + (c_{12} + c_{66}) \frac{\partial^2 v}{\partial x \partial y} = \beta_1 \frac{\partial T}{\partial x}, \tag{8}$$

$$c_{66} \frac{\partial^2 v}{\partial x^2} + c_{22} \frac{\partial^2 v}{\partial y^2} + (c_{12} + c_{66}) \frac{\partial^2 u}{\partial x \partial y} = \beta_2 \frac{\partial T}{\partial y}. \tag{9}$$

Making use of the Fourier heat conduction leads to

$$\begin{aligned} Q_x &= -\lambda_x \frac{\partial T}{\partial x}, \\ Q_y &= -\lambda_y \frac{\partial T}{\partial y}, \end{aligned} \tag{10}$$

where the definitions of Q_x, Q_y, λ_x, and λ_y have been given in [3]. Furthermore, based on the equilibrium equation,

one has

$$\frac{\partial Q_x}{\partial x} + \frac{\partial Q_y}{\partial y} = 0. \tag{11}$$

Taking advantage of the thermal equilibrium equations brings out

$$\lambda^2 \frac{\partial^2 T}{\partial x^2} + \frac{\partial^2 T}{\partial y^2} = 0, \tag{12}$$

where

$$\lambda = \sqrt{\frac{\lambda_x}{\lambda_y}}. \tag{13}$$

The crack face boundary conditions are depicted as

$$Q_y^{II}(x,0) - Q_y^{I}(x,0) = -\frac{Q_1 x}{2(b-a)^2}, \quad |a| < x < |b|, \tag{14}$$

$$\sigma_y^{II}(x,0) = \sigma_y^{I}(x,0) = \frac{\sigma_1 |x|}{b-a} + \sigma_0, \quad |a| < x < |b|, \tag{15}$$

Hereafter, the subscript 'I' or 'II' denotes the physical quantity of the upper ($y > 0$) or below ($y < 0$) part. Q_0, Q_1, σ_0, and σ_1 stand for the prescribed constants. Based on (14) and (15), thermal flux is composed of only one part ($-Q_1 x/2(b\text{-}a)^2$) and mechanical loading is divided into two parts ($\sigma_1|x|/(b-a)$ and σ_0). As linear thermal flux and linear mechanical load are antisymmetrical and symmetrical, respectively, the thermoelastic field of the region ($x > 0$) is only dealt with. The crack-surface boundary conditions are expressed with the application of the improved partially insulated crack model.

$$\tau_{xy}^{II}(x,0) = \tau_{xy}^{I}(x,0) = 0, \quad a < x < b, \tag{16}$$

$$Q_y^{II}(x,0) - Q_y^{I}(x,0) = -\frac{Q_1 - Q_{1c}}{2(b-a)^2}\, x \quad a < x < b, \tag{17}$$

$$\sigma_y^{II}(x,0) = \sigma_y^{I}(x,0) = \frac{\sigma_1 x}{b-a} + \sigma_0, \quad a < x < b. \tag{18}$$

According to Equations (17) and (18), the solutions under thermal flux ($-Q_1 x/2(b\text{-}a)^2$) and mechanical loading (σ_0) have been given explicitly in [24, 25]. Next, we depict the boundary conditions of crack-surface subject to linear mechanical load ($\sigma_1 x/(b-a)$).

$$\tau_{xy}^{I}(x,0) = \tau_{xy}^{II}(x,0) = 0, \quad a < x < b, \tag{19}$$

$$\sigma_y^{II}(x,0) = \sigma_y^{I}(x,0) = \frac{\sigma_1 x}{b-a}, \quad a < x < b, \tag{20}$$

where

$$Q_{1c} = -h_c\left(T^{I}(x,0) - T^{II}(x,0)\right) + \varepsilon Q_1. \tag{21}$$

Besides, some physical quantities conform to the following conditions:

$$\begin{aligned}
&\tau_{xy}^{I}(x,0) = \tau_{xy}^{II}(x,0),\ \sigma_y^{I}(x,0) = \sigma_y^{II}(x,0), && x > b \text{ or } 0 < x < a,\\
&u^{I}(x,0) = -u^{II}(x,0),\ v^{I}(x,0) = -v^{II}(x,0), && x > b \text{ or } 0 < x < a,\\
&T^{I}(x,0) = T^{II}(x,0),\ Q_y^{I}(x,0) = Q_y^{II}(x,0), && x > b \text{ or } 0 < x < a.
\end{aligned} \tag{22}$$

3. Solution Procedure

3.1. Temperature Field. According to [25], one obtains the explicit form of temperature difference on crack faces as

$$T^{I}(x,0) - T^{II}(x,0) = -\frac{Q_1 - Q_{1c}}{2(b-a)^2 \lambda \lambda_y} \sqrt{(x^2 - a^2)(b^2 - x^2)}, \quad a < x < b. \tag{23}$$

3.2. Elastic Field. To achieve the goal of explicit form in Equations (8) and (9), $u^{I,II}(x,y)$ and $v^{I,II}(x,y)$ are expressed according to [26].

$$u^{I,II}(x,y) = \sum_{i=1}^{2} u_i^{I,II}(x,y), \quad v^{I,II}(x,y) = \sum_{i=1}^{2} v_i^{I,II}(x,y), \tag{24}$$

where the definitions of $u_j^{I,II}(x,y)$ and $v_j^{I,II}(x,y)$ $(j = 1, 2)$ have been given in [26].

$$u_1^{I,II}(x,y) = \sum_{j=1}^{2} \int_0^{+\infty} g_j^{I,II}(\xi) e^{-\xi \delta^{\pm} \gamma_j y} \sin(\xi x) d\xi, \tag{25}$$

$$v_1^{I,II}(x,y) = \sum_{j=1}^{2} \int_0^{+\infty} \eta_j \delta^{\pm} g_j^{I,II}(\xi) e^{-\xi \delta^{\pm} \gamma_j y} \cos(\xi x) d\xi. \tag{26}$$

Hereafter, $\delta^{+} = 1$ or $\delta^{-} = -1$ denotes $y > 0$ or $y < 0$. $g_j^{I,II}(\xi)$ need to solve. The definitions of $\gamma_j (j = 1, 2)$ have been given in [26].

$$c_{22} c_{66} \gamma^4 + \left(c_{12}^2 + 2c_{12} c_{66} - c_{12} c_{22}\right)\gamma^2 + c_{11} c_{66} = 0, \tag{27}$$

where

$$\eta_j = \frac{c_{11} - c_{66} \gamma_j^2}{(c_{12} + c_{66})\gamma_j}. \tag{28}$$

Furthermore, $u_2^{I,II}(x,y)$ and $v_2^{I,II}(x,y)$ are chosen as

$$u_2^{I,II}(x,y) = \sum_{j=1}^{2} \int_0^{+\infty} g^{*I,II}(\xi) e^{-\delta \pm \xi \lambda y} \sin(\xi x) d\xi, \tag{29}$$

$$v_2^{I,II}(x,y) = \sum_{j=1}^{2} \int_0^{+\infty} \delta^{\pm} L^{*I,II}(\xi) e^{-\delta \pm \xi \lambda y} \cos(\xi x) d\xi. \tag{30}$$

Taking advantage of Equations (29), (30), (8), and (9),

we have

$$\begin{bmatrix} g^{*I,II}(\xi) \\ L^{*I,II}(\xi) \end{bmatrix} = \begin{bmatrix} M_1 \\ M_2 \end{bmatrix} \frac{g^{I,II}(\xi)}{\xi}, \tag{31}$$

where

$$\begin{bmatrix} M_1 \\ M_2 \end{bmatrix} = \begin{bmatrix} c_{11} - c_{66}\lambda^2 & -(c_{12} + c_{66})\lambda \\ (c_{12} + c_{66})\lambda & c_{66} - c_{22}\lambda^2 \end{bmatrix}^{-1} \begin{bmatrix} \beta_1 \\ \beta_2\lambda \end{bmatrix}. \tag{32}$$

By the aid of Equations (3)–(5), (25), (26), (29), and (30), the components of stress are in the form of the following expressions:

$$\sigma_x^{I,II}(x,0) = \sum_{j=1}^{2} \int_0^{+\infty} \left(c_{11} - c_{12}\gamma_j\eta_j\right)\xi g_j^{I,II}(\xi)\cos(\xi x)d\xi + (c_{11}M_1 - c_{12}\lambda M_2 - \beta_1)\int_0^{+\infty} g^{I,II}(\xi)\cos(\xi x)d\xi, \tag{33}$$

$$\sigma_y^{I,II}(x,0) = \sum_{j=1}^{2} \int_0^{+\infty} \left(c_{12} - c_{22}\gamma_j\eta_j\right)\xi g_j^{I,II}(\xi)\cos(\xi x)d\xi + (c_{12}M_1 - c_{22}\lambda M_2 - \beta_2)\int_0^{+\infty} g^{I,II}(\xi)\cos(\xi x)d\xi, \tag{34}$$

$$\tau_{xy}^{I,II}(x,0) = -c_{66}\left[\sum_{j=1}^{2}\int_0^{+\infty}\delta^{\pm}\left(\gamma_j + \eta_j\right)\xi g_j^{I,II}(\xi)\sin(\xi x)d\xi + \int_0^{+\infty}\delta^{\pm}(M_1\lambda + M_2)g^{I,II}(\xi)\sin(\xi x)d\xi\right]. \tag{35}$$

In order to get the explicit solution of this considered problem, we depict the dual integral equations as

$$\tau_{xy}^{I}(x,0) = \tau_{xy}^{II}(x,0) = 0, \quad x > 0, \tag{36}$$

$$v^{I}(x,0) = -v^{II}(x,0) = 0, \quad 0 < x < a \text{ or } x > b. \tag{37}$$

Using Equations (36) and (37), one gets

$$\begin{aligned} g_j^{I}(\xi) &= g_j^{II}(\xi), \\ g_2^{I}(\xi) &= -\frac{\gamma_1 + \eta_1}{\gamma_2 + \eta_2} g_1^{I}(\xi). \end{aligned} \tag{38}$$

Applying Equations (20) and (37), one obtains

$$\int_0^{+\infty} \xi g_1^{I}(\xi)\cos(\xi x)d\xi = 0, \quad 0 < x < a \text{ or } x > b, \tag{39}$$

$$\int_0^{+\infty} \xi g_1^{I}(\xi)\cos(\xi x)d\xi = \frac{\sigma_1 x}{\ell_1(b-a)}, \quad a < x < b, \tag{40}$$

where

$$\ell_1 = (c_{12} - c_{22}\gamma_1\eta_1) - \frac{\gamma_1 + \eta_1}{\gamma_2 + \eta_2}(c_{12} - c_{22}\gamma_2\eta_2). \tag{41}$$

In order to solve Equations (39) and (40), the auxiliary function $\phi(x)$ is introduced as

$$\phi(x) = \frac{\partial v^{I}(x,0)}{\partial x}. \tag{42}$$

Applying inverse Fourier transform leads to

$$g_1^{I}(\xi)\xi = -\frac{2(\gamma_2 + \eta_2)}{(\eta_1\gamma_2 - \eta_2\gamma_1)\pi}\int_a^b \phi(s)\sin(\xi s)ds. \tag{43}$$

Inserting Equation (43) into (40), one has

$$\frac{2}{\pi}\int_a^b \phi(s)ds\int_0^{\infty}\sin(\xi s)\cos(\xi x)d\xi = -\frac{\sigma_1(\eta_1\gamma_2 - \eta_2\gamma_1)}{\ell_1(\gamma_2 + \eta_2)(b-a)}x. \tag{44}$$

Recalling the known result [27],

$$\int_0^{\infty}\cos(\xi x)\sin(\xi s)d\xi = \frac{s}{s^2 - x^2}. \tag{45}$$

Based on Equation (45), Equation (44) can be expressed as

$$\frac{1}{\pi}\int_a^b \frac{2s\phi(s)}{s - x}ds = -\frac{\sigma_1(\eta_1\gamma_2 - \eta_2\gamma_1)}{\ell_1(\gamma_2 + \eta_2)(b-a)}x. \tag{46}$$

It is convenient to introduce $s^2 = \bar{s}, x^2 = \bar{x}, 2sds = d\bar{s}$, $a^2 = \bar{a}, b^2 = \bar{b}$, and $\overline{\phi}(\bar{s}) = \phi(s)$. Equation (46) is rewritten as

$$\frac{1}{\pi}\int_{\bar{a}}^{\bar{b}} \frac{\overline{\phi}(\bar{s})}{\bar{s} - \bar{x}}d\bar{s} = \frac{\sigma_1(\eta_1\gamma_2 - \eta_2\gamma_1)}{\ell_1(\gamma_2 + \eta_2)(b-a)}\sqrt{\bar{x}}. \tag{47}$$

According to the singular integral containing the Cauchy kernel4 [28], the solution of Equation (47) is obtained

$$\overline{\phi}(\bar{x}) = \frac{1}{\pi\sqrt{(\bar{x} - \bar{a})(\bar{b} - \bar{x})}}\int_{\bar{a}}^{\bar{b}} \frac{\sqrt{\bar{s}(\bar{s} - \bar{a})(\bar{b} - \bar{s})}}{\bar{x} - \bar{s}}\frac{\sigma_1(\eta_1\gamma_2 - \eta_2\gamma_1)}{\ell_1(\gamma_2 + \eta_2)(b-a)}d\bar{s}. \tag{48}$$

In the application of Equation (42), the closed form of

elastic displacement is obtained

$$v^I(x,0)=\int_{\bar{a}}^{\bar{x}}\frac{\overline{\phi}(\bar{t})}{2\sqrt{\bar{t}}}d\bar{t}. \tag{49}$$

Inserting Equation (48) into (34), the stress field is obtained as

$$\begin{aligned}\sigma_y^{I,II}(x,0)=&-\frac{\sigma_1}{\pi(b-a)\sqrt{(a^2-x^2)(b^2-x^2)}}\\&\times\left[\frac{2x^2(x^2-a^2-b^2)}{b}F(\lambda)+2bx^2E(\lambda)\right]\\&+O(1),\quad 0<x<a,\\\sigma_y^{I,II}(x,0)=&-\frac{\sigma_1}{\pi(b-a)\sqrt{(a^2-x^2)(b^2-x^2)}}\\&\times\left[\frac{2x^2(x^2-a^2-b^2)}{b}F(\lambda)+2bx^2E(\lambda)\right]\\&+O(1),\quad x>b.\end{aligned} \tag{50}$$

$F(\lambda)$ and $E(\lambda)$ denote the first and second kinds of complete elliptical integrals, respectively, where

$$\lambda=\frac{\sqrt{b^2-a^2}}{b}. \tag{51}$$

For simplicity, the detailed procedure of reduction under thermal flux is omitted. The shear stresses are obtained according to [25].

$$\begin{aligned}\tau_{xy}^{I,II}(x,0)=&\frac{c_{66}H_2P}{c_{22}(\gamma_2\eta_2-\gamma_1\eta_1)\sqrt{(x^2-a^2)(b^2-x^2)}}\\&\times\left[\frac{4a^2b^2}{3}+\frac{(a^2-b^2)^2}{2}+\frac{2b^2(a^2+b^2)E(\lambda)}{3F(\lambda)}\right.\\&\left.-(2x^2-a^2-b^2)^2\right]+O(1),\quad 0<x<a,\\\tau_{xy}^{I,II}(x,0)=&\frac{c_{66}H_2P}{c_{22}(\gamma_2\eta_2-\gamma_1\eta_1)\sqrt{(x^2-a^2)(b^2-x^2)}}\\&\times\left[\frac{4a^2b^2}{3}+\frac{(a^2-b^2)^2}{2}+\frac{2b^2(a^2+b^2)E(\lambda)}{3F(\lambda)}\right.\\&\left.-(2x^2-a^2-b^2)^2\right]+O(1),\quad x>b,\end{aligned} \tag{52}$$

where

$$\begin{aligned}P=&\frac{(Q_1-Q_{1c})\ell_2}{(b-a)^2(b+a)\lambda\lambda_y},\ell_2=\frac{H_1}{H_2},H_1\\=&(\gamma_1+\eta_1)(c_{22}\gamma_2\eta_2M_1-c_{22}\lambda M_2-\beta_2)\\&+(\gamma_2+\eta_2)(c_{22}\lambda M_2+\beta_2-c_{22}\gamma_1\eta_1M_1)\\&+c_{22}(M_1\lambda+M_2)(\gamma_1\eta_1-\gamma_2\eta_2)\\H_2=&(\gamma_1+\eta_1)(c_{22}\gamma_2\eta_2-c_{12})\\&+(\gamma_2+\eta_2)(c_{12}-c_{22}\gamma_1\eta_1).\end{aligned} \tag{53}$$

By superposition theory, the exact solutions of the physical quantities are obtained subject to linear thermal flux $(-Q_1x/2(b-a)^2)$ and linear mechanical load $(\sigma_1|x|/(b-a)+\sigma_0)$.

3.3. Crack-Tip Field. Using Equations (2) and (23), one obtains the closed form of heat flux to the crack surface.

$$Q_{1c}=\frac{2\varepsilon Q_1(b-a)^2\lambda+Q_1R_c\sqrt{(x^2-a^2)(b^2-x^2)}}{2(b-a)^2\lambda+R_c\sqrt{(x^2-a^2)(b^2-x^2)}}. \tag{54}$$

We define the value of $R_c=\lambda_y/h_c$ to stand for the dimensionless thermal resistance between crack faces. It is easily found Equation (54) is different from that in [25]. When $R_c=0$ and $R_c\longrightarrow\infty$, one obtains $Q_{1c}=\varepsilon Q_1$ or $Q_{1c}\longrightarrow Q_1$, meaning partially thermally insulated or fully conductive cracks. When $R_c=0$ and $\varepsilon=0$, one has $Q_{1c}=0$, meaning fully thermally insulated cracks.

4. Fracture Parameters

It is important that the stress intensity factors including the mode-I and mode-II should be defined as the analysis of cracked growth.

$$\begin{aligned}K_I^{\mathrm{Inn}}=&\lim_{x\longrightarrow a^-}\sqrt{2\pi(a-x)}\sigma_y^{I,II}(x,0),K_I^{\mathrm{Out}}\\=&\lim_{x\longrightarrow b^+}\sqrt{2\pi(x-b)}\sigma_y^{I,II}(x,0),\end{aligned} \tag{55}$$

$$\begin{aligned}K_{II}^{\mathrm{Inn}}=&\lim_{x\longrightarrow a^-}\sqrt{2\pi(a-x)}\tau_{xy}^{I,II}(x,0),K_{II}^{\mathrm{Out}}\\=&\lim_{x\longrightarrow b^+}\sqrt{2\pi(x-b)}\tau_{xy}^{I,II}(x,0).\end{aligned} \tag{56}$$

Based on Equation (55), one can obtain

$$\begin{aligned}K_I^{\mathrm{Inn}}=&\sqrt{\frac{\pi}{a(b^2-a^2)}}\{2a^2b[F(\lambda)-E(\lambda)]\}\frac{\sigma_1}{\pi(b-a)},\\K_I^{\mathrm{Out}}=&\sqrt{\frac{\pi}{b(b^2-a^2)}}\{2b[b^2E(\lambda)-a^2F(\lambda)]\}\frac{\sigma_1}{\pi(b-a)}.\end{aligned} \tag{57}$$

When $a=0$, it means the mode-I stress intensity factor

Table 1: Tyrannohex.

E_{xx} (MPa)	E_{yy} (MPa)	G_{xy} (MPa)	ν_{xy}	ν_{yx}	α_{xx} $(10^{-7}/°C)$	α_{yy} $(10^{-7}/°C)$	λ_x (w/m°C)	λ_y (w/m°C)
135000	87000	50000	0.15	0.09667	32	32	3.08	2.81

of a single crack with $2b$. It is easily found that

$$K_I^{\text{Out}} = \frac{2\sqrt{\pi b}\sigma_1}{\pi}. \tag{58}$$

According to Equation (56) and Reference [25], one has

$$K_{II}^{\text{Inn}} = \frac{c_{66}H_2P}{2c_{22}(\gamma_2\eta_2 - \gamma_1\eta_1)} \cdot \left(\frac{4a^2b^2}{3} - \frac{\left(a^2-b^2\right)^2}{2} - \frac{2b^2\left(a^2+b^2\right)E(\lambda)}{3F(\lambda)}\right)\sqrt{\frac{\pi}{a\left(b^2-a^2\right)}},$$

$$K_{II}^{\text{Out}} = -\frac{c_{66}H_2P}{2c_{22}(\gamma_2\eta_2 - \gamma_1\eta_1)} \cdot \left(\frac{4a^2b^2}{3} - \frac{\left(a^2-b^2\right)^2}{2} - \frac{2b^2\left(a^2+b^2\right)E(\lambda)}{3F(\lambda)}\right)\sqrt{\frac{\pi}{b\left(b^2-a^2\right)}}. \tag{59}$$

The importance of strain energy in a unit volume of the solid is illustrated for nonisothermal [29, 30].

$$\frac{dW}{dV} = \frac{S}{r}. \tag{60}$$

where the definitions of S and r have been given in [24]. For the orthotropic solid, Equation (60) can also be given based on the above concepts of energy density function

$$\frac{S}{r} = \frac{c_{22}\left(\sigma_x^I\right)^2 + c_{11}\left(\sigma_y^I\right)^2 - 2c_{12}\sigma_x^I\sigma_y^I}{2c_{11}c_{22} - c_{12}^2} + \frac{\left(\tau_{xy}^I\right)^2}{2c_{66}}. \tag{61}$$

The following strain energy density factor on the crack line is defined to study crack growth in fracture mechanics [24].

$$S^{Inn,Out} = \frac{1}{4\pi}\left[\frac{c_{22}\ell^2 + c_{11} - 2c_{12}\ell}{c_{11}c_{22} - c_{12}^2}\left(K_I^{Inn,Out}\right)^2 + \frac{1}{c_{66}}\left(K_{II}^{Inn,Out}\right)^2\right], \tag{62}$$

where

$$\ell = \frac{1}{\ell_1}\sum_{j=1}^{2}(-1)^j\frac{\gamma_1+\eta_1}{\gamma_j+\eta_j}\left(c_{11} - c_{12}\gamma_j\eta_j\right). \tag{63}$$

5. Numerical Results

For the sake of simplicity, some numerical examples are employed to demonstrate R_c and ε have great effects on Q_{1c}, K_{II}, and S subject to linear thermal flux$(-Q_1x/2(b-a)^2$) and linear mechanical load $(\sigma_0|x|/(b-a))$. The orthotropic material like Tyrannohex is selected as in [31] (Table 1).

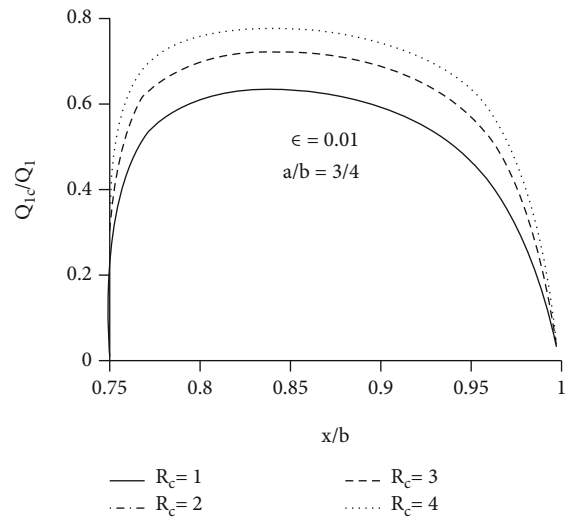

Figure 2: Q_{1c}/Q_1 versus x/b with $R_c = 1, 2, 3, 4$ for ε =0.01 and $a/b = 3/4$.

Figure 2 shows Q_{1c}/Q_1 versus x/b with $R_c = 1, 2, 3, 4$ for $\varepsilon = 0.01$ and $a/b = 3/4$. Q_{1c}/Q_1 increases with an increase of R_c for a fixed x/b as shown in Figure 2. The case of $R_c = 1$ implies the heat conduction between the upper and blow crack faces is the same as that of external material of crack. The cases of $R_c = 2, 3, 4$ imply to the heat conduction between the upper and blow crack faces are twice, triple, and quadruple as much as thermal conductivities of the external material of crack. Figure 3 displays Q_{1c}/Q_1 versus x/b with $\varepsilon = -0.02, 0, 0.02, 0.04$ for $R_c = 2$ and $a/b = 3/4$. As the dimensionless thermal resistance R_c increases, Q_{1c}/Q_1 increases. The constant ε is considered to be an adjustment quantity. The bigger the value of constant ε, the greater the heat flux per thickness through crack. It means making use of the extended partially insulated crack model involving the greater R_c or ε will overestimate the heat flux per thickness to the crack surface. Furthermore, it is suitable to decease or increase stress field near outer and inn cracks tip by the way of filling certain materials into the region between the upper and below crack faces according to Figures 2 and 3.

Figure 4 displays $K_{II}^{\text{Inn}}/K_{II0}^{\text{Inn}}$ or $K_{II}^{\text{Out}}/K_{II0}^{\text{Out}}$ versus x/b with $a/b = 0.25, 0.5, 0.75$ where K_{II0}^{Inn} and K_{II0}^{Out} denote K_{II}^{Inn} and K_{II}^{Out} for $Q_{1c} = 0$, respectively. $K_{II}^{\text{Inn}}/K_{II0}^{\text{Inn}}$ or $K_{II}^{\text{Out}}/K_{II0}^{\text{Out}}$ decreases when R_c increases for a fixed x/b. Figure 5 displays $K_{II}^{\text{Inn}}/K_{II0}^{\text{Inn}}$ or $K_{II}^{\text{Out}}/K_{II0}^{\text{Out}}$ versus x/b with $R_c = 1, 2, 3, 4$ for $\varepsilon = 0.01$ and $a/b = 3/4$. As the

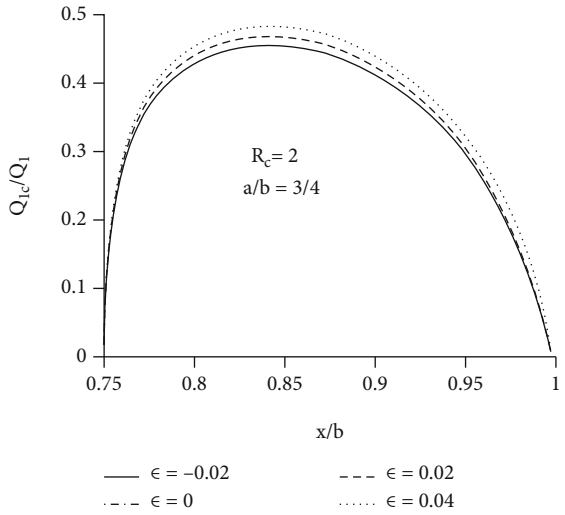

Figure 3: Q_{1c}/Q_1 versus x/b with $\varepsilon = -0.02, 0, 0.02, 0.04$ for $R_c = 2$ and $a/b = 3/4$.

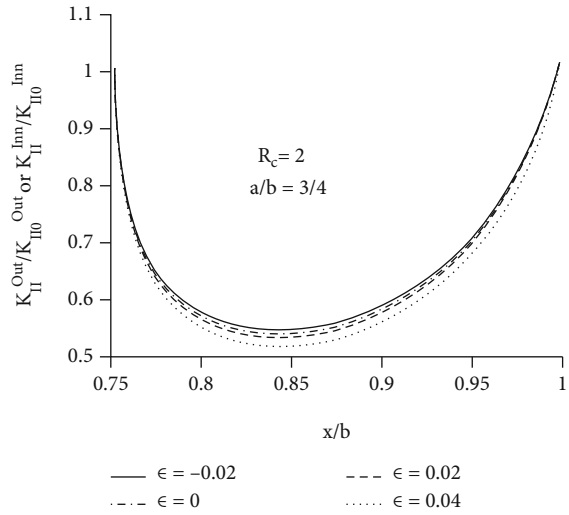

Figure 5: $K_{II}^{Inn}/K_{II0}^{Inn}$ or $K_{II}^{Out}/K_{II0}^{Out}$ versus x/b with $\varepsilon = -0.02, 0, 0.02, 0.04$ for $R_c = 2$ and $a/b = 3/4$.

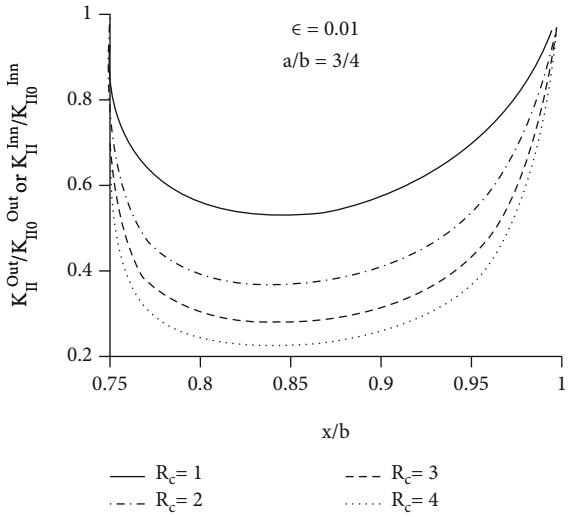

Figure 4: $K_{II}^{Inn}/K_{II0}^{Inn}$ or $K_{II}^{Out}/K_{II0}^{Out}$ versus x/b with $R_c = 1, 2, 3, 4$ for $\varepsilon = 0.01$ and $a/b = 3/4$.

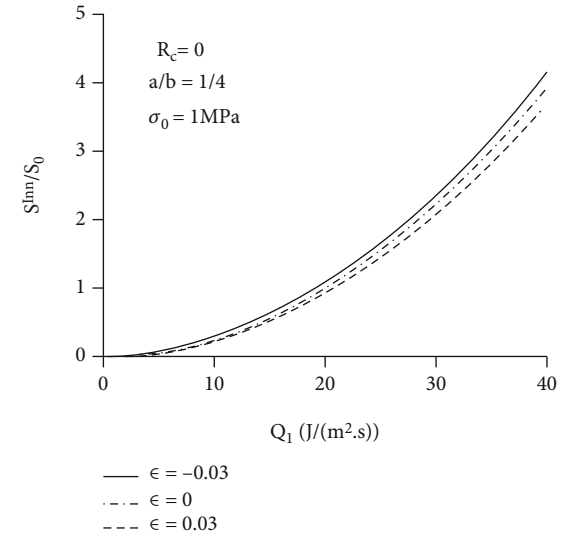

Figure 6: S^{Inn}/S_0 versus Q_1 with $\varepsilon = -0.03, 0, 0.03$ for $R_c = 0$, $\sigma_0 = 1$ MPa, and $a/b = 1/4$.

dimensionless thermal resistance R_c increases, the mode-II stress intensity factors decrease. The bigger the value of constant ε, the smaller the mode-II stress intensity factors. It means making use of the extended partially insulated crack model involving the greater R_c and ε will underestimate the mode-II stress intensity factors. The obtained results reveal that the crack face boundary conditions, the thermal properties of crack, and the raised coefficients have great influences on the heat flux per thickness to the crack surface and the mode-II stress intensity factors.

In order to present the influence of the thermal properties of crack on $S^{Inn,Out}$, the value of S_0 is easily defined.

$$S_0 = \frac{c_{22}\ell^2 + c_{11} - 2c_{12}\ell}{4(c_{11}c_{22} - {c_{11}}^2)}\sigma_0^2, \tag{64}$$

which denotes the strain energy density factor of a crack with $2b$ under mechanical load σ_0. Figures 6 and 7 show S^{Inn}/S_0 and S^{Out}/S_0 versus Q_1 with $\varepsilon = -0.03, 0, 0.03$ for $R_c = 2$, $\sigma_0 = 1$ MPa, and $a/b = 1/4$. Figures 6 and 7 respond to the two cases of strain energy density factor near outer and inn cracks for partially thermally insulated cracks. It is easily seen that S^{Inn}/S_0 and S^{Out}/S_0 are made up of the mode-II stress intensity factor under thermal flux $(-Q_1 x/2(b-a)^2)$ and the mode-I stress intensity factor induced by mechanical load $(\sigma_0|x|/(b-a))$. The corresponding S^{Inn}/S_0 and S^{Out}/S_0 increase with an increase of thermal flux and mechanical load. The strain energy density factor on the crack line is greatly influenced by the adjustment quantity ε. The bigger the value of constant ε, the smaller S^{Inn}/S_0 and S^{Out}/S_0. So,

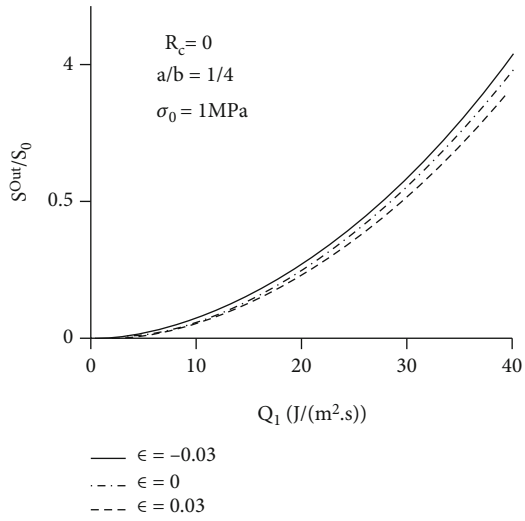

FIGURE 7: S^{Out}/S_0 versus Q_1 with $\varepsilon = -0.03, 0, 0.03$ for $R_c = 0$, $\sigma_0 = 1$ MPa, and $a/b = 1/4$.

applying the bigger value of constant ε will underestimate S^{Inn}/S_0 and S^{Out}/S_0.

From the above figures, it is revealed R_c and ε have significant impacts on the analysis of a cracked solid. In other words, some physical quantities (i.e., R_c and ε) should be given enough attention to the analysis of the thermoelastic field.

6. Conclusions

This paper addresses two collinear cracks in an orthotropic solid under linear thermal flux and linear mechanical load in this paper. Some physical quantities and fracture parameters are obtained in explicit forms with application of the proposed extended partially insulated crack model, Fourier transform, and superposition theory. The results show that R_c and ε have vital effects on Q_{1c} and some fracture parameters. The obtained results reveal the boundary conditions of crack face, thermal properties of crack, and the raised coefficients should be concerned about the analysis of a cracked solid under the thermal load.

Conflicts of Interest

The authors declare that they have no conflicts of interest.

Acknowledgments

The work was supported by the Hebei University Scientific Research Foundation for higher-level talent (No. 521100221019), the Project Funded by China Postdoctoral Science Foundation (No. 2019M662946), and the Ningxia Key Research and Development Program (Introduction of Talents Project) (No. 2020BEB04039).

References

[1] W. Nowacki, *Thermoelasticity*, Pergamon Press, New York, 1962.

[2] R. W. Goldstein and V. M. Vainshelbaum, "Axisymmetric problem of a crack at the interface of layers in a multilayered medium," *International Journal of Engineering Science*, vol. 14, no. 4, pp. 335–352, 1976.

[3] J. L. Nowinski, *Theory of Thermoelasticity with Applications*, Sijthoff and Noordhoff, The Netherlands, 1978.

[4] G. C. Sih, "Thermomechanics of solids: nonequilibrium and irreversibility," *Theoretical and Applied Fracture Mechanics*, vol. 9, no. 3, pp. 175–198, 1988.

[5] Z. Olesiak and I. N. Sneddon, "The distribution of thermal stress in an infinite elastic solid containing a penny-shaped crack," *Archive for Rational Mechanics and Analysis*, vol. 4, no. 1, pp. 238–254, 1959.

[6] V. I. Fabrikant, *Mixed Boundary Value Problem of Potential Theory and Their Applications in Engineering*, vol. 42, no. 5, 1991, Kluwer Academic Publishers, The Netherlands, 1991.

[7] Y. M. Tsai, "Orthotropic thermoelastic problem of uniform heat flow disturbed by a central crack," *Journal of Composite Materials*, vol. 18, no. 2, pp. 122–131, 1984.

[8] H. Ju and R. E. Rowlands, "Mixed-mode thermoelastic fracture analysis of orthotropic composites," *International Journal of Fracture*, vol. 120, no. 4, pp. 601–621, 2003.

[9] B. X. Chen and X. Z. Zhang, "Thermoelasticity problem of an orthotropic plate with two collinear cracks," *International Journal of Fracture*, vol. 38, no. 3, pp. 161–192, 1988.

[10] N. Noda, "Transient thermal stress problem in an orthotropic thin plate with a Griffith crack," *Archive of Applied Mechanics*, vol. 57, no. 3, pp. 175–181, 1987.

[11] A. A. Rizk, "Orthotropic semi-infinite medium with a crack under thermal shock," *Theoretical and Applied Fracture Mechanics*, vol. 46, no. 3, pp. 217–231, 2006.

[12] J. Kim and G. Paulino, "Mixed-mode fracture of orthotropic functionally graded materials using finite elements and the modified crack closure method," *Engineering Fracture Mechanics*, vol. 69, no. 14-16, pp. 1557–1586, 2002.

[13] L. M. Brock, "Reflection and diffraction of plane temperature-step waves in orthotropic thermoelastic solids," *Journal of Thermal Stresses*, vol. 33, no. 9, pp. 879–904, 2010.

[14] S. Dag, "Thermal fracture analysis of orthotropic functionally graded materials using an equivalent domain integral approach," *Engineering Fracture Mechanics*, vol. 73, no. 18, pp. 2802–2828, 2006.

[15] B. Wu, D. Peng, and R. Jones, "Fracture analysis for a crack in orthotropic material subjected to combined 2*i*-order symmetrical thermal flux and 2*j*-order symmetrical mechanical loading," *Applied Mechanics*, vol. 2, no. 1, pp. 127–146, 2021.

[16] X. C. Zhong, X. Y. Long, and L. H. Zhang, "An extended thermal-medium crack model," *Applied Mathematical Modelling*, vol. 56, pp. 202–216, 2018.

[17] C. H. Wu, "Plane anisotropic thermoelasticity," *Journal of Applied Mechanics*, vol. 51, no. 4, pp. 724–726, 1984.

[18] M. Nagai, T. Ikeda, and N. Miyazaki, "Stress intensity factor analysis of an interface crack between dissimilar anisotropic materials under thermal stress using the finite element analysis," *International Journal of Fracture*, vol. 146, no. 4, pp. 233–248, 2007.

[19] L. Liu and G. A. A. Kardomateas, "A dislocation approach for the thermal stress intensity factors of a crack in an infinite anisotropic medium under uniform heat flow," *Composites: Part A*, vol. 37, no. 7, pp. 989–996, 2006.

[20] Z. Xue, A. G. Evans, and J. W. Hutchinson, "Delamination susceptibility of coatings under high thermal flux," *Journal of Applied Mechanics*, vol. 76, no. 4, pp. 728–731, 2009.

[21] Y. T. Zhou, X. Li, and D. H. Yu, "A partially insulated interface crack between a graded orthotropic coating and a homogeneous orthotropic substrate under heat flux supply," *International Journal of Solids and Structures*, vol. 47, no. 6, pp. 768–778, 2010.

[22] S. Thangjitham and H. J. Choi, "Thermal stress singularities in an anisotropic slab containing a crack," *Mechanics of Materials*, vol. 14, no. 3, pp. 223–238, 1993.

[23] A. Y. Kuo, "Effects of crack surface heat conductance on stress intensity factors," *Journal of Applied Mechanics*, vol. 57, no. 2, pp. 354–358, 1990.

[24] X. C. Zhong, B. Wu, and K. S. Zhang, "Thermally conducting collinear cracks engulfed by thermomechanical field in a material with orthotropy," *Theoretical and Applied Fracture Mechanics*, vol. 65, pp. 61–68, 2013.

[25] B. Wu, J. G. Zhu, D. Peng, R. Jones, S. H. Gao, and Y. Y. Lu, "Thermoelastic analysis for two collinear cracks in an orthotropic solid disturbed by antisymmetrical linear heat flow," *Mathematical Problems in Engineering*, vol. 2017, Article ID 5093404, 10 pages, 2017.

[26] B. Wu, ,D. Peng, and R. Jones, "On the analysis of cracking under a combined quadratic thermal flux and a quadratic mechanical loading," *Applied Mathematical Modelling*, vol. 68, pp. 182–197, 2019.

[27] I. S. Gradshteyn and I. M. Ryzhik, *Table of Integrals, Series, and Products, Elsevier*, Academic Press, California, 2007.

[28] N. I. Mushkelishvili, *Singular Integral Equations*, Wolters-Noorhoff, Groningen, 1953.

[29] G. C. Sih, J. Michaopoloulos, and S. C. Chou, *Hygrothermoelasticity*, Martinus Niijhoof Publishing, Leiden, The Netherland, 1986.

[30] G. C. Sih, *Mechanics of Fracture Initiation and Propagation*, Kluwer Academic Publishers, Boston, MA, USA, 1991.

[31] S. Itou, "Thermal stress intensity factors of an infinite orthotropic layer with a crack," *International Journal of Fracture*, vol. 103, no. 3, pp. 279–291, 2000.

Hindawi
Advances in Mathematical Physics
Volume 2022, Article ID 2318436, 22 pages
https://doi.org/10.1155/2022/2318436

Research Article

A Parametric Analysis of the Effect of Hybrid Nanoparticles on the Flow Field and Homogeneous-Heterogeneous Reaction between Squeezing Plates

Wajid Ullah Jan,[1] Muhammad Farooq,[1] Aamir Khan,[2] Asma Alharbi,[3] Rehan Ali Shah,[4] Rashid Jan,[5] and Sahar Ahmed Idris[6,7]

[1]*Department of Mathematics, Abdul Wali Khan University Mardan, Mardan, 23200 KP, Pakistan*
[2]*Department of Pure and Applied Mathematics, The University of Haripur, Haripur, KP, Pakistan*
[3]*Department of Mathematics, College of Science and Arts, Qassim University, Ar Rass, Saudi Arabia*
[4]*Department of Basic Sciences and Islamiat, University of Engineering and Technology, Peshawar, KP, Pakistan*
[5]*Department of Mathematics, University of Swabi, Swabi 23561, KP, Pakistan*
[6]*College of Industrial Engineering, King Khalid University, Abha 62529, Saudi Arabia*
[7]*Department of Mathematics, College of Sciences, University of Juba, Juba, South Sudan*

Correspondence should be addressed to Sahar Ahmed Idris; sa6044690@gmail.com

Received 21 October 2021; Accepted 13 January 2022; Published 9 February 2022

Academic Editor: David Carf

Different strategies have been utilized by investigators with the intention of upgrading the thermal characteristics of ordinary liquids like water and kerosene oil. The focus is currently on hybrid nanomaterials since they are more efficient than nanofluids, so as to increase the thermal conductivity of fluids and mixtures. In a similar manner, this investigation is performed with the aim of breaking down the consistent mixed convection flow close to a two-dimensional unstable flow between two squeezing plates with homogeneous and heterogeneous reaction in the presence of hybrid nanoparticles of the porous medium. A sustainable suspension in the ethylene glycol with water is set by dissolving inorganic substances, iron oxide (Fe_3O_4) and cobalt (Co), to form $Fe_3O_4 - Co/C_2H_6O_2 - H_2O$ hybrid nanofluid. The numerical and analytical model portraying the fluid flow has been planned, and similitude conditions have been determined with the assistance of the same transformations. The shooting technique has been used to solve nonlinear numerical solution. To check the validity of the results obtained from the shooting mode, the Matlab built-in function BVP4c and Mathematica built-in function homotopy analysis method (HAM) are used. The influence of rising parameters on velocity, temperature, skin friction factor, Nusselt number, and Sherwood number is evaluated with the help of graphs and tables. It has been found in this work that to acquire a productive thermal framework, the hybrid nanoparticles should be considered instead of a single sort of nanoparticles. In addition, the velocities of both the hybrid nanofluids and simple nanofluids are upgraded by the mixed convection boundary, whereas they are decreased by the porosity. An augmentation in volumetric fraction of nanoparticles correlates to an increment in the heat transmission rate. It is also found that heat transfer rate for $Fe_3O_4 - Co/C_2H_6O_2 - H_2O$ hybrid nanofluids (HNF) is better than that of the $Fe_3O_4 - C_2H_6O_2 - H_2O$ of single nanofluids (SNF). This research shows that hybrid nanofluids play a significant part in the transfer of heat and in the distribution of nanofluids at higher temperatures.

1. Introduction

Pressure flows have many engineering, scientific, and technical applications in the industry such as lubrication system, moveable pistons, hydrodynamic engines, hydraulic lifts, scattering and formulation, chemical equipment processing, food processing, film damage, and frost damage syringes and nasogastric tubes. The initial study of squeezing flow was published by Stefan [1] who reported the lubrication method in his research. New doors were opened by

Stephen's rewarding work for researchers on squeezing flows. Different researchers studied the flow of compression and followed him. From different research perspectives, this study has been pushed forward in recent years to compress the flow. Hayat et al. [2] have examined the squeezed flow of MHD fluid between two horizontal disks using homotopy analysis. The result of their investigation was found to be an increase in the velocity field of for augmenting values of micropolar parameter. Mustafa et al. [3] analyzed the fluid flow with magnetic effects upon thermal and mass transmission behavior of an incompressible viscous Casson fluid flow amid parallel plates. They have noticed in this work that flow has been augmented with escalating values of squeezing parameter. The two-dimensional magnetized laminar constant Marangoni convection of the incompressible viscous fluid was explored by Mahanthesh et al. [4] by implementing the Runge–Kutta–Fehlberg technique. The authors have found that the boundary layer thickness and the increasing meridian convection have increased the fluid velocity within the flow area.

Ferroliquids are magnetic nanofluids suspended in nondirecting liquids such as water, hydrocarbons, and kerosene. These ferrofluids have various applications in medical science like cell partition, focusing of drug medication, and imaging of magnetic characters. The thermal and magnet functions of the ferrofluid flow were investigated by Neuringer [5]. Khan et al. [6] examined the influence of a homogeneous heat stream on flat-surface slip flows with heat transfer. They evaluated three distinct ferrofluids with two distinct basic fluids ($CoFe_2O_4$, Fe_3O_4, and $Mn - ZnFe_2O_4$) (water and kerosene). Rashad [7] examined the magnetic slip-flow function containing nonisothermal convection and radiation wedge kerosene based cobalt ferrofluid. Zaib et al. [8] investigated a mixed convective flow entropy of a vertical plate of magnetite ferrofluid. Ali et al. [9] recently discussed the magnetic dipole impact on micropolar fluid consisting of the EG and the water-based ferrofluids Fe and Fe_3O_4 from a stretched sheet.

Hybrid nanoliquids, however, are deliberately captured by blending several different nanoparticles with better thermal and rheological characteristics. The introduction of hybrid ferroliquids is to increase heat transfer efficiency in fluid flow. It has several scientific applications such as dynamic sealing, naval sealing, dampening, and microfluidics. Suresh et al. [10] investigated the effect of dissipation on time-based flux comprising a rounded pipe of hybrid nanoliquid. They have achieved a lower friction factor for nanolytes than for hybrid nanol. The pressurization decline in the volume percentage of the water-based $Cu - TiO_2$ hybrid nanolic was examined by Madhesh and Kalaiselvam [11]. Minea [12] revealed the association with the date of the temperature gradient of alumina hybrids and nanofluids. The fluid flow characteristics of hybrid nanoliquids from water-based Ag–CuO were evaluated by Hayat and Nadeem [13]. Mebarek-Oudina [14] examined the thermal and hydrodynamic parameters of Titania nanoliquids that satisfy a cylinder annulus, the impact of annulus, Mahanthesh et al. [15] An exponential spatially dependent magneto slip heat source flow from an extendable rotation consisting of carbon nanofluids. Marzougui et al. [16] investigated the surface effects. $Al_2O_3 - CuO$ stability roughness and radiation nanolic hybrid through the widespread use of the model. Recently, Wakif et al. [17] examined the entropy examination through convective flow including nanoliquid by means of MHD with chamfers in a hole. The investigation of the attractive capacity has significant sales in MHD orientation; topography, astronomy, siphons, generators, medication, control of limit layer, and so on are many noticeable MHD applications. Alshomrani and Gul [18] inspected the slight film flow of water-based Al_2O_3 and Cu nanofluid through an extended chamber under the effect of attractive capacity. The characteristics of magneto thermal transport, comprising a time dependent flux of liquid nanofluid thin film flow to a starched surface, were examined by Sandeep and Malvandi [19]. Sandeep [20] examined the characteristics of the hybrid nanolytic flux with various heat and drag forces. Ahmad and Nadeem [21] examined the magnetic effects of hybrid nanofluid with a heat sink/source on micropolitan fluid and achieved numerous findings for hybrid nanofluid and micropolar fluid. Hamrelaine et al. [22] examined the magnetic effect of Jeffery–Hamel flow between nonparallel permeable walls or permeable plates. The attractive impact on the radiative progression of the hybrid nanoliquid thin film with sporadic warmth sink/source was examined by Anantha Kumar et al. [23]. Zaib et al. [24] got the comparability of various outcomes from magnetite ferroliquid passing on non-Newtonian blood stream with entropy age. Wakif et al. [25] assessed the impact of the magnetic field on progressions of Stokes' second issue with entropy generation. Recently, Kameswaran et al. [26] investigated homogeneous-heterogeneous reactions in nanofluid flow due to a microscopic stretch sheet. They showed that the velocity profiles decrease with an increasing volume of the nanoparticles, while the liquid concentration is reversed by the volume of the nanoparticles for both Cu-water and Ag-water nanofluids.

The cited literature and similar other works show that no study is conducted to examine the combined effects of unstable flow between two squeezing plates in the presence of hybrid nanoparticles. Therefore, using all the studies mentioned above, we analyzed the multifaceted and homogeneous chemical reaction effects on the flow between two compression plates in the presence of hybrid nanoparticles. Navier–Stokes equations, heat transfer, and homogeneous and multifaceted reactions are solved by the HAM and BVP4c. In this work, we analyzed, discussed, and obtained the effects of different parameters on velocity, temperature, concentration, skin friction coefficient, and Nusselt and Sherwood numbers through graphs and tables.

2. Mathematical Formulation

Figure 1 shows a laminar, unsteady incompressible, and two-dimensional and hybrid nanofluid flowing between horizontally parallel and squeezing plates with homogeneous and heterogeneous reactions. Hybrid nanoparticles comprise Fe_3O_4 and $Fe_3O_4 + Co$ in the ethylene glycol with water as base fluid suspension. The plates are separated by a

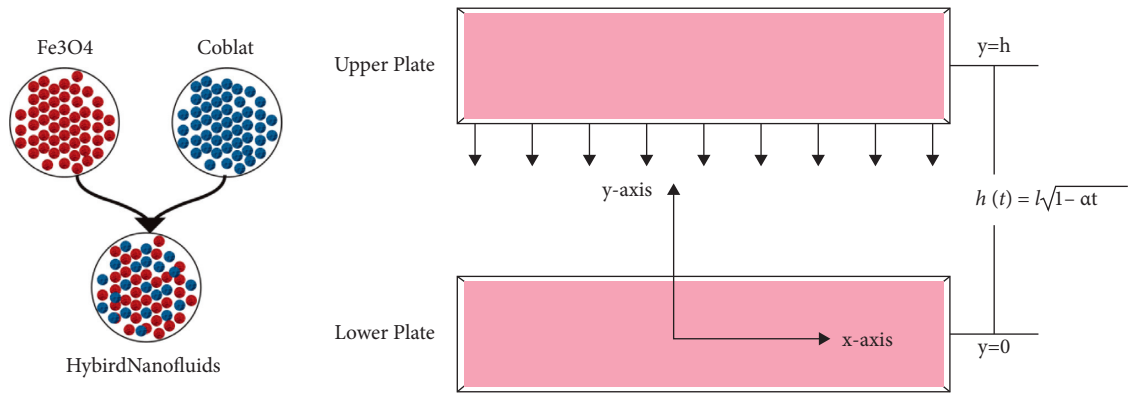

Figure 1: Geometrical view of flow problem.

gap of $h(t) = l\sqrt{1-\alpha t}$ with α as squeezed parameter. For $\alpha > 0$, the plates are squeezing but when $t = (1/\alpha)$ and $\alpha < 0$, the two plates are separated. The velocity field is often impacted by a uniform magnetic field $B(t) = B_0/\sqrt{1-\alpha t}$ distributed along the y-axis. The upper and lower plates are held at steady temperature T_u and T_l, respectively. The proposed model of Chaudhary and Merkin [27] for homogeneous as well as heterogeneous reaction has been used in this study as described below.

The homogeneous reaction for cubic autocatalyst surface is

$$N1 + 2N2 \longrightarrow 3N2. \tag{1}$$

The heterogeneous reaction upon catalyst surface is

$$N1 \longrightarrow A2. \tag{2}$$

The quantities of the chemical sorts $N1$ and $N2$ are signified by a and b, respectively, while the initial conditions are denoted by k_c. The reaction rate vanishes in exterior flow and beyond the boundary layer bottom, as shown by the equations above. The equations that governed the flow system are presented as [28, 29].

Continuity equation is as follows:

$$\frac{\partial u}{\partial x} + \frac{\partial v}{\partial y} = 0. \tag{3}$$

Navier–Stokes equation is as follows:

$$\frac{\partial u}{\partial t} + u\frac{\partial u}{\partial x} + v\frac{\partial u}{\partial y} = -\frac{1}{\rho_{hnf}}\frac{\partial p}{\partial x} + \frac{\mu_{hnf}}{\rho_{hnf}}\left(\frac{\partial^2 u}{\partial x^2} + \frac{\partial^2 u}{\partial y^2}\right) - \sigma_{hnf}B^2 u,$$

$$\frac{\partial v}{\partial t} + u\frac{\partial v}{\partial x} + v\frac{\partial v}{\partial y} = -\frac{1}{\rho_{hnf}}\frac{\partial p}{\partial y} + \frac{\mu_{hnf}}{\rho_{hnf}}\left(\frac{\partial^2 v}{\partial x^2} + \frac{\partial^2 v}{\partial y^2}\right). \tag{4}$$

Energy equation is as follows:

$$\frac{\partial T}{\partial t} + u\frac{\partial T}{\partial x} + v\frac{\partial T}{\partial y} = \frac{k_{hnf}}{(\rho c_p)_{hnf}}\left(\frac{\partial^2 T}{\partial x^2} + \frac{\partial^2 T}{\partial y^2}\right) + \frac{1}{(\rho c_p)_{hnf}}\frac{16\sigma^* T_0^3}{3\kappa^*}\frac{\partial^2 T}{\partial y^2} + \frac{Q^*}{(\rho c_p)_{hnf}}(T - T_0). \tag{5}$$

Homogeneous and heterogeneous equations are as follows:

$$\frac{\partial a}{\partial t} + u\frac{\partial a}{\partial x} + v\frac{\partial a}{\partial y} = D_A\frac{\partial^2 a}{\partial y^2} - K_c ab^2,$$

$$\frac{\partial b}{\partial t} + u\frac{\partial b}{\partial x} + v\frac{\partial b}{\partial y} = D_B\frac{\partial^2 b}{\partial y^2} + K_c ab^2. \tag{6}$$

In the above equations, T represents temperature, P represents pressure, ρ_{hnf} represents effective density, $(\rho c_p)_{hnf}$ represents effective heat power, and σ_{hnf} represents electrical conductivity of nanofluid. The quantities (u, v) denote the fluid's nanofluid velocity component, T is the temperature, and D_A and D_B are the respective diffusion constants of the chemical sorts a and b. The permeability is provided by K^*. k_{hnf} nanofluid thermal conductivity, Q^* heat generation, k_{hnf} nanofluid thermal conductivity, k_{hnf} nanofluid thermal conductivity, k_{hnf} nanofluid thermal conduct.

2.1. Boundary Conditions. The squeezing flow under consideration has the undermentioned conditions at boundaries:

$$u = 0, v = 0, T = T_l, D_A\frac{\partial a}{\partial y} = k_3 a, D_B\frac{\partial b}{\partial y} = -k_3 a \text{ at } y = 0,$$

$$u = 0, v = \frac{-\alpha D}{2\sqrt{1-\alpha t}}, T = T_u, a = a_0, b = 0 \text{ at } y = h(t). \tag{7}$$

Use the transformations [2]

$$u = \frac{\alpha x f'(\eta)}{2(1-\alpha t)},$$
$$v = \frac{-\alpha l f(\eta)}{(1-\alpha t)},$$
$$T = \theta(\eta) T_H, \tag{7a}$$
$$\eta = \frac{y}{l\sqrt{1-\alpha t}},$$
$$a = a_0 H(\eta),$$
$$b = a_0 G(\eta),$$
$$B(t) = \frac{B_0}{\sqrt{1-at}}, \tag{7b}$$
$$\theta = \frac{T - T_u}{T_l - T_u}.$$

Implementing equations (7a) and (7b), we have the following system of equations:

$$f''' - S\left(\frac{A_1}{A_4}\right)\left(\eta f''' + 2f'' + f'' f' - f f'''\right) - \left(\frac{A_5}{A_4}\right) Ha^2 L f'' = 0, \tag{8}$$

$$\theta''\left(1 + \frac{4}{3}R\right) + P_r S\left(f\theta' - 2\eta\theta + Q\theta\right) = 0, \tag{9}$$

$$H'' - S_c K_1 H G^2 - S_c S\left(\eta H' - f H\right) = 0, \tag{10}$$

$$G''\delta - S_c K_1 H G^2 - S_c S\left(\eta G' - f G'\right) = 0, \tag{11}$$

and the boundary conditions are reduced to

$$\begin{aligned} &f(0) = 0, f'(0) = 0, \theta(0) = 1, H'(0) \\ &\quad = K_2 H(0), \delta G'(0) = -K_2 H(0), \\ &f(1) = 0.5, f'(1) = 0, \theta(1) = 0, H(1) = 1, G(1) = 0. \end{aligned} \tag{12}$$

Here, $S = (\alpha l^2/2\nu_f)$ is the squeezed Reynolds number, $P_r = (\mu c_p/K)$ is the Prandtl number, $Ha = lB_0\sqrt{\sigma_{hnf}/\mu_f}$ is the Hartmann number, $R = (4\sigma^* T_0^3/KK^*)$ is the radiation parameter, $Q = 2Q^*(1-\alpha t)/\alpha(\rho c_p)_{hnf}$ is the heat generation parameter, $L = (\alpha\sigma_{nf}/x)$ is the length parameter, $S_c = (\nu_f/D_A)$ is the Schmidt number, $K_1 = 8k_c a_0^2(1-\alpha t)/\alpha^3$ is the homogeneous reaction strength, $K_2 = (k_s/D_A)$ is the heterogeneous reaction strength, and $\delta = (D_A/D_B)$ is the ratio of the diffusion coefficients. Here, it is considered that A and B diffusion coefficients of chemical species are of comparable size. The other hypothesis is that D_A and D_B are equivalent, so $\delta = (D_A/D_B) = 1$, and $G(\eta) + H(\eta) = 1$ [30].

2.2. Coefficients of Interest. The local Nusselt number (Nu), Sherwood number (Sh), and skin friction coefficient (Cf) are some of the coefficients of interest in engineering.

$$\begin{aligned} C_f^* &= \frac{S}{h} C_f = f''(0), \\ -\theta'(0) &= \mathrm{Nu}, \\ -G'(0) &= -H'(0) = \mathrm{Sh}. \end{aligned} \tag{13}$$

By using A_i for the dimensionless constant, the result will be as follows:

$$A_1 = \frac{\mu_{nf}}{\mu_f} = \frac{1}{(1-\phi)^{2.5}}, \phi = \phi 1 + \phi 2,$$
$$A_4 = \frac{\rho_{nf}}{\rho_f} = (1-\phi) + \phi 1\left(\frac{\rho_1}{\rho_f}\right) + \phi 2\left(\frac{\rho_2}{\rho_f}\right),$$
$$A_5 = \frac{\sigma_{nf}}{\sigma_f} = \left(1 + 3\left(\sigma_1\phi_1 + \sigma_2\phi_2\right)\sigma_f^{-1} - \phi\right)$$
$$+\left(\left(\sigma_1 + \sigma_2\right)\sigma_f^{-1} + 2\right)^{-1} - \left(\left(\sigma_1\phi_1 + \sigma_2\phi_2\right)\sigma_f^{-1} + \phi 1\right)^{-1}. \tag{14}$$

The total volume fraction of nanoparticles is represented by ϕ. The volume fractions of the discrete nanoparticles are represented by the symbols $\phi 1$ and $\phi 2$; the density of first, second, and base fluids of nanoparticles is ρ_1, ρ_2, and ρ_f; and the electrical conductivity of 1st, 2nd, and base fluids of nanoparticles is σ_1, σ_2 and σ_f.

3. Approximate Analytical Solution

To solve system of equations (8)–(11), the analytic method HAM is used. Due to HAM, the functions $f(\varrho)$, $\theta(\varrho)$, $H(\varrho)$, and $G(\varrho)$ can be stated by a set of base functions $\varrho^c, c \geq 0$ as

$$f_\Psi(\varrho) = \sum_{\xi=0}^{\infty} a_\xi \varrho^\xi, \tag{15}$$

$$\theta_\Psi(\varrho) = \sum_{\xi=0}^{\infty} b_\xi \varrho^\xi, \tag{16}$$

$$H_\Psi(\varrho) = \sum_{\xi=0}^{\infty} c_\xi \varrho^\xi, \tag{17}$$

$$G_\Psi(\varrho) = \sum_{\xi=0}^{\infty} d_\xi \varrho^\xi, \tag{18}$$

where a_ξ, b_ξ, c_ξ, and d_ξ are the constant coefficients to be determined. Initial approximations are chosen as follows:

$$f_0(\varrho) = \frac{3}{2}\varrho^2 - \varrho^3, \tag{19}$$

$$\theta_0(\varrho) = \left(S_r - 1\right)\varrho + 1, \tag{20}$$

$$H_0(\varrho) = 1 - \varrho, \tag{21}$$

$$G_0(\varrho) = 1 - \varrho. \tag{22}$$

The auxiliary operators are chosen as

$$\begin{aligned} \ell_f &= \frac{\partial^4}{\partial \varrho^4}, \\ \ell_\theta &= \frac{\partial^2}{\partial \varrho^2}, \\ \ell_H &= \frac{\partial^2}{\partial \varrho^2}, \\ \ell_G &= \frac{\partial^2}{\partial \varrho^2}, \end{aligned} \tag{23}$$

with the following properties:

$$\ell_f\left(\xi_1 \varrho^3 + \xi_2 \varrho^2 + \xi_3 \varrho + \xi_4\right) = 0, \tag{24}$$

$$\ell_\theta\left(\xi_5 \varrho + \xi_6\right) = 0, \tag{25}$$

$$\ell_H\left(\xi_7 \varrho + \xi_8\right) = 0, \tag{26}$$

$$\ell_G\left(\xi_9 \varrho + \xi_{10}\right) = 0, \tag{27}$$

where ξ_1, ξ_2, ξ_3, ξ_4, ξ_5, ξ_6, ξ_7, ξ_8, ξ_9, and ξ_{10} are arbitrary constants.

The zeroth order deformation problems can be obtained as

$$(1;\varpi)\ell_f\left[\overline{f}(\varrho;\varpi) - f_0(\varrho)\right] = q\hbar_f N_f[\overline{f}(\varrho;\varpi), \overline{\theta}(\varrho;\varpi), \overline{m}(\varrho;\varpi), \overline{n}(\varrho;\varpi)], \tag{28}$$

$$(1;\varpi)\ell_\theta\left[\overline{\theta}(\varrho;\varpi) - \theta_0(\varrho)\right] = q\hbar_\theta N_\theta[\overline{f}(\varrho;\varpi), \overline{\theta}(\varrho;\varpi), \overline{m}(\varrho;\varpi), \overline{n}(\varrho;\varpi)], \tag{29}$$

$$(1;\varpi)\ell_H\left[\overline{H}(\varrho;\varpi) - H_0(\varrho)\right] = q\hbar_H N_H[\overline{f}(\varrho;\varpi), \overline{H}(\varrho;\varpi), \overline{G}(\varrho;\varpi)], \tag{30}$$

$$(1;\varpi)\ell_G\left[\overline{G}(\varrho;\varpi) - G_0(\varrho)\right] = q\hbar_G N_G[\overline{f}(\varrho;\varpi), \overline{H}(\varrho;q), \overline{G}(\varrho;\varpi)]. \tag{31}$$

The nonlinear operators of (17)–(20) are defined as

$$\begin{aligned} N_f[\overline{f}(\varrho;\varpi), \overline{\theta}(\varrho;\varpi)] &= \frac{\partial^4 \overline{f}(\varrho;\varpi)}{\partial \varrho^4} - S\left[\varrho \frac{\partial^3 \overline{f}(\varrho;\varpi)}{\partial \varrho^3} + 2\frac{\partial^2 \overline{f}(\varrho;\varpi)}{\partial \varrho^2} + \frac{\partial^2 \overline{f}(\varrho;\varpi)}{\partial \varrho^2}\frac{\partial \overline{f}(\varrho;\varpi)}{\partial \varrho} - f\frac{\partial^3 \overline{f}(\varrho;\varpi)}{\partial \varrho^3}\right] \\ &\quad - Ha^2 L \frac{\partial^2 \overline{f}(\varrho;\varpi)}{\partial \varrho^2}, \\ N_\theta[\overline{f}(\varrho;\varpi), \overline{\theta}(\varrho;\varpi)] &= \frac{\partial^2 \overline{\theta}(\varrho;\varpi)}{\partial \varrho^2}\left(1 + \frac{4}{3}R\right) + PrS\left[f\frac{\partial \overline{\theta}(\varrho;\varpi)}{\partial \varrho} - 2\varrho\overline{\theta}(\varrho;\varpi) + Q\overline{\theta}(\varrho;\varpi)\right], \\ N_H[\overline{f}(\varrho;\varpi), \overline{H}(\varrho;\varpi), \overline{G}(\varrho;\varpi)] &= \frac{\partial^2 \overline{H}(\varrho;\varpi)}{\partial \varrho^2} - S_c K_1 \overline{H}(\varrho;\varpi)\frac{\partial^2 \overline{G}(\varrho;\varpi)}{\partial \varrho^2} - S_c S\left[\varrho\frac{\partial \overline{H}(\varrho;\varpi)}{\partial \varrho} - f\overline{H}(\varrho;\varpi)\right], \\ N_G[\overline{f}(\varrho;\varpi), \overline{H}(\varrho;\varpi), \overline{G}(\varrho;\varpi)] &= \frac{\partial^2 \overline{G}(\varrho;\varpi)}{\partial \varrho^2}\delta - S_c K_1 \overline{H}(\varrho;\varpi)\frac{\partial^2 \overline{G}(\varrho;\varpi)}{\partial \varrho^2} - S_c S\left[\varrho\frac{\partial \overline{G}(\varrho;\varpi)}{\partial \varrho} - f\frac{\partial \overline{G}(\varrho;\varpi)}{\partial \varrho}\right], \end{aligned} \tag{32}$$

where ϖ is an embedding parameter; $\hbar_f$, $\hbar_\theta$, $\hbar_H$, and $\hbar_G$ are the nonzero auxiliary parameter; and N_f, N_θ, N_H, and N_G are the nonlinear parameters.

For $\varpi = 0$ and 1, we have

$$\begin{aligned}
&\overline{f}(\varrho,0) = f_o(\varrho), \overline{f}(\varrho,1) = f(\varrho),\\
&\overline{\theta}(\varrho,0) = \theta_o(\varrho), \overline{\theta}(\varrho,1) = \theta(\varrho),\\
&\overline{H}(\varrho,0) = H_o(\varrho), \overline{H}(\varrho,1) = H(\varrho),\\
&\overline{G}(\varrho,0) = G_o(\varrho), \overline{G}(\varrho,1) = G(\varrho),
\end{aligned} \tag{33}$$

so we can say that as ϖ varies from 0 to 1, $\overline{f}(\varrho,0)$, $\overline{\theta}(\varrho,0)$, $\overline{H}(\varrho,0)$, and $\overline{G}(\varrho,0)$ vary from initial guesses $f_0(\varrho)$, $\theta_0(\varrho)$, $H_0(\varrho)$, and $G_0(\varrho)$ to exact solutions $f(\varrho)$, $\theta(\varrho)$, $H(\varrho)$, and $G(\varrho)$, respectively.

Taylor's series expansion of these functions yields

$$\begin{aligned}
f(\varrho;\varpi) &= f_0(\varrho) + \sum_{\Psi=1}^{\infty} \varpi^{\Psi} f_{\Psi}(\varrho),\\
\theta(\varrho;\varpi) &= \theta_0(\varrho) + \sum_{\Psi=1}^{\infty} \varpi^{\Psi} \theta_{\Psi}(\varrho),\\
H(\varrho;\varpi) &= H_0(\varrho) + \sum_{\Psi=1}^{\infty} \varpi^{\Psi} H_{\Psi}(\varrho),\\
G(\varrho;\varpi) &= G_0(\varrho) + \sum_{\Psi=1}^{\infty} \varpi^{\Psi} G_{\Psi}(\varrho),\\
f_{\Psi}(\varrho) &= \frac{1}{\Psi!} \frac{\partial^{\Psi} f(\varrho;\varpi)}{\partial \varrho^{\Psi}}\bigg|_{\varpi=0},\\
\theta_{\Psi}(\varrho) &= \frac{1}{\Psi!} \frac{\partial^{\Psi} \theta(\varrho;\varpi)}{\partial \varrho^{\Psi}}\bigg|_{\varpi=0},\\
H_{\Psi}(\varrho) &= \frac{1}{\Psi!} \frac{\partial^{\Psi} H(\varrho;\varpi)}{\partial \varrho^{\Psi}}\bigg|_{\varpi=0},\\
G_{\Psi}(\varrho) &= \frac{1}{\Psi!} \frac{\partial^{\Psi} G(\varrho;\varpi)}{\partial \varrho^{\Psi}}\bigg|_{\varpi=0}.
\end{aligned} \tag{34}$$

The convergence is strongly supported by $\hbar_f$, $\hbar_\theta$, $\hbar_H$, and $\hbar_G$.

For $\varpi = 1$, we have

$$f(\varrho) = f_0(\varrho) + \sum_{\Psi=1}^{\infty} f_{\Psi}(\varrho), \tag{35}$$

$$\theta(\varrho) = \theta_0(\varrho) + \sum_{\Psi=1}^{\infty} \theta_{\Psi}(\varrho), \tag{36}$$

$$H(\varrho) = H_0(\varrho) + \sum_{\Psi=1}^{\infty} H_{\Psi}(\varrho), \tag{37}$$

$$G(\varrho) = G_0(\varrho) + \sum_{\Psi=1}^{\infty} G_{\Psi}(\varrho). \tag{38}$$

Differentiating the deformation equations (25)–(28) Ψ – times with respect to ϖ and putting $\varpi = 0$, we have

$$\ell_f\left[f_{\Psi}(\varrho) - \chi_{\Psi} f_{\Psi-1}(\varrho)\right] = \hbar_f R_{f,\Psi}(\varrho), \tag{39}$$

$$\ell_\theta\left[\theta_{\Psi}(\varrho) - \chi_{\Psi} \theta_{\Psi-1}(\varrho)\right] = \hbar_\theta R_{g,\Psi}(\varrho), \tag{40}$$

$$\ell_H\left[H_{\Psi}(\varrho) - \chi_{\Psi} H_{\Psi-1}(\varrho)\right] = \hbar_H R_{H,\Psi}(\varrho), \tag{41}$$

$$\ell_G\left[G_{\Psi}(\varrho) - \chi_{\Psi} G_{\Psi-1}(\varrho)\right] = \hbar_\phi R_{G,\Psi}(\varrho), \tag{42}$$

subject to the boundary conditions

$$\begin{aligned}
&f_{\Psi}(0) = 0, f'_{\Psi}(0) = 0, \theta_{\Psi}(0) = 1,\\
&H'_{\Psi}(0) = k_2 H(0), \delta G'_{\Psi}(0) = -k_2 H(0),\\
&f_{\Psi}(1) = 0.5, f'_{\Psi}(1) = 0, \theta_{\Psi}(1) = 0,\\
&H_{\Psi}(1) = 1, G f'_{\Psi}(1) = 0,
\end{aligned} \tag{43}$$

where

$$R_{f,\Psi}(\varrho) = f'''_{\Psi-1}(\varrho) - S\left(\frac{A_1}{A_4}\right)\left[\varrho f'''_{\Psi-1}(\varrho) + 2f''_{\Psi-1}(\varrho) + 2\sum_{j=0}^{\Psi-1} f_j(\varrho) f'''_{\Psi-j-1}(\varrho) - \sum_{j=0}^{\Psi-1} f_j(\varrho) f''_{\Psi-j-1}(\varrho)\right] - \left(\frac{A_5}{A_4}\right) Ha^2 L f''_{\Psi-1}(\varrho), \tag{44}$$

$$R_{\theta,\Psi}(\varrho) = \theta''_{\Psi-1}(\varrho)\left(1 + \frac{4}{3}R\right) + PrS\left[\sum_{j=0}^{\Psi-1} f_j(\varrho)\theta'_{\Psi-j-1}(\varrho) - 2\varrho\theta_{\Psi-1}(\varrho) + Q\theta_{\Psi-1}(\varrho)\right], \tag{45}$$

$$R_{H,\Psi}(\varrho) = H''_{\Psi-1}(\varrho) + S_c K_1 \sum_{j=0}^{\Psi-1} H_j(\varrho) G''_{\Psi-j-1}(\varrho) - S_c S\left[\varrho H'_{\Psi-1}(\varrho) - \sum_{j=0}^{\Psi-1} f_j(\varrho) H_{\Psi-j-1}(\varrho)\right], \tag{46}$$

$$R_{G,\Psi}(\varrho) = G''_{\Psi-1}(\varrho)\delta - S_c K_1 \sum_{j=0}^{\Psi-1} H_j(\varrho) G^2_{\Psi-j-1}(\varrho) - S_c S\left[\varrho G'_{\Psi-1}(\varrho) - \sum_{j=0}^{\Psi-1} f_j(\varrho) G'_{\Psi-j-1}(\varrho)\right], \tag{47}$$

and $\chi_{\Psi} = \{1, \text{if } \Psi > 1, \text{and } 0, \text{if } \Psi = 1\}$.

Finally, the general solution of (36)–(39) can be written as

$$f_\Psi(\varrho) = \int_0^\varrho \int_0^\varrho \int_0^\varrho \int_0^\varrho \hbar_f R_{f,\Psi}(z)\mathrm{d}z\mathrm{d}z\mathrm{d}z\mathrm{d}z + \chi_\Psi f_{\Psi-1} + \xi_1\varrho^3 + \xi_2\varrho^2 + \xi_3\varrho + \xi_4, \tag{48}$$

$$\theta_\Psi(\varrho) = \int_0^\varrho \int_0^\varrho \hbar_\theta R_{\theta,\Psi}(z)\mathrm{d}z\mathrm{d}z + \chi_\Psi\theta_{\Psi-1} + \xi_5\varrho + \xi_6, \tag{49}$$

$$H_\Psi(\varrho) = \int_0^\varrho \int_0^\varrho \hbar_H R_{H,\Psi}(z)\mathrm{d}z\mathrm{d}z + \chi_\Psi H_{\Psi-1} + \xi_{11}\varrho + \xi_{12}, \tag{50}$$

$$G_\Psi(\varrho) = \int_0^\varrho \int_0^\varrho \hbar_G R_{G,\Psi}(z)\mathrm{d}z\mathrm{d}z + \chi_\Psi G_{\Psi-1} + \xi_{13}\varrho + \xi_{14}, \tag{51}$$

and so the exact solutions $f(\varrho)$, $\theta(\varrho)$, $H(\varrho)$, and $H(\varrho)$ become

$$\begin{aligned} f(\varrho) &\approx \sum_{n=0}^{\Psi} f_n(\varrho), \\ \theta(\varrho) &\approx \sum_{n=0}^{\Psi} \theta_n(\varrho), \\ H(\varrho) &\approx \sum_{n=0}^{\Psi} H_n(\varrho), \\ G(\varrho) &\approx \sum_{n=0}^{\Psi} G_n(\varrho). \end{aligned} \tag{52}$$

4. Optimizing the Convergence of Control Parameter

It is important to note that the series solutions (46)–(49) include $\hbar_f$, $\hbar_\theta$, $\hbar_H$, and $\hbar_G$ nonzero auxiliary parameters that define the convergence area as well as rate of the homotopy series solutions. The residual error to obtain the maximum values of $\hbar_f$, $\hbar_\theta$, $\hbar_H$, and $\hbar_G$ was used as

$$\begin{aligned} \epsilon_\Psi^f &= \frac{1}{\xi+1}\sum_{j=0}^{\xi}\left[N_f\sum_{i=0}^{\Psi}\overline{f}(\varrho), \sum_{i=0}^{\Psi}\overline{\theta}(\varrho)\right]^2 \mathrm{d}\varrho, \\ \epsilon_\Psi^\theta &= \frac{1}{\xi+1}\sum_{j=0}^{\xi}\left[N_\theta\left(\sum_{i=0}^{\Psi}\overline{f}(\varrho), \sum_{i=0}^{\Psi}\overline{\theta}(\varrho)\right)_{n=jD_u n}\right]^2 \mathrm{d}\varrho, \\ \epsilon_\Psi^H &= \frac{1}{\xi+1}\sum_{j=0}^{\xi}\left[N_H\left(\sum_{i=0}^{\Psi}\overline{f}(\varrho), \sum_{i=0}^{\Psi}\overline{H}(\varrho), \sum_{i=0}^{\Psi}\overline{G}(\varrho)\right)_{n=jD_u n}\right]^2 \mathrm{d}\varrho, \\ \epsilon_\Psi^G &= \frac{1}{\xi+1}\sum_{j=0}^{\xi}\left[N_G\left(\sum_{i=0}^{\Psi}\overline{f}(\varrho), \varpi\sum_{i=0}^{\Psi}\overline{H}(\varrho), \sum_{i=0}^{\Psi}\overline{G}(\varrho)\right)_{n=jD_u n}\right]^2 \mathrm{d}\varrho. \end{aligned} \tag{53}$$

Due to Liao

$$\epsilon_\Psi^t = \epsilon_\Psi^f + \epsilon_\Psi^\theta + \epsilon_\Psi^H + \epsilon_\Psi^G, \tag{54}$$

where ϵ_Ψ^t is the total squared residual error.

5. Analysis of Error

An error analysis is conducted to ensure a minimum residual error for the efficiency of the analysis. HAM and BVP4c solve the problem analytically and numerically. The analysis is conducted using an approximation order of the 40th order. For this analysis, the validity of HAM techniques is also evaluated using the Mathematica software BVPh 2.0 for maximum residual error 10^{-40}. The results are compared with the numerical solution of BVP4c using Matlab for the authentication and consistency of the HAM solution. The reliability of the two methods for various concerning physical parameters is investigated by error analysis in Figure 2 and Tables 1–12. Figure 2 shows that up to the 16th transition series, the maximum average residual errors of $f''(\eta)$, $-\theta'(\eta)$, $-H'(\eta)$, and $-G'(\eta)$ are almost gradually decreased. The cumulative residual error for the various approximation orders of fixed $P_r = -0.5$, $S = -0.5$, $L = 0.01$, $Q = 5$, $R = 0.7$, $\delta = 1$, $Sc = 2.5$, $K1 = 0.1$, $K2 = 1$, and $Ha = 0.1$ values is shown in Table 1. Table 2 shows various orders of approximation with distinct average squared residual error for $f''(\eta)$, $-\theta'(\eta)$, $-H'(\eta)$, and $-G'(\eta)$ with fixed values as $P_r = 0.5$, $S = -0.5$, $L = 0.01$, $\delta = 1$, $Q = 0.01$, $R = 0.1$, $Sc = 2.5$, $K1 = 0.3$, $K2 = 0.1$, $Ha = 0.2$ $\phi = 0.02$, $\phi 1 = \phi 2 = 0.01$, $\rho 1 = 5180$, $\rho 2 = 8900$, $\rho 3 = 1056$, $\sigma 1 = 0.74 \times 10^6$, $\sigma 2 = 1.602 \times 10^7$, $\sigma 3 = 0.00509$. The comparison of the analytical and numerical values by HAM and BVP4c is shown in Table 3 for various values of η and fixed values of other parameters, $P_r = 0.5$, $S = -0.5$, $L = 0.01$, $\delta = 1$, $Q = 0.01$, $R = 0.1$, $Sc = 2.5$, $K1 = 0.3$, $K2 = 0.1$, $Ha = 0.2$, $\phi = 0.02$, $\phi 1 = \phi 2 = 0.01$, $\rho 1 = 5180$, $\rho 2 = 8900$, $\rho 3 = 1056$, $\sigma 1 = 0.74 \times 10^6$, $\sigma 2 = 1.602 \times 10^7$, and $\sigma 3 = 0.00509$.

6. Results and Discussion

For various values of parameters S, Ha, P_r, Q, R, Sc, $K1$, $K2$, and ϕ, the system of nonlinear equations (8)–(11), resulting in the boundary conditions equation (12), is numerically

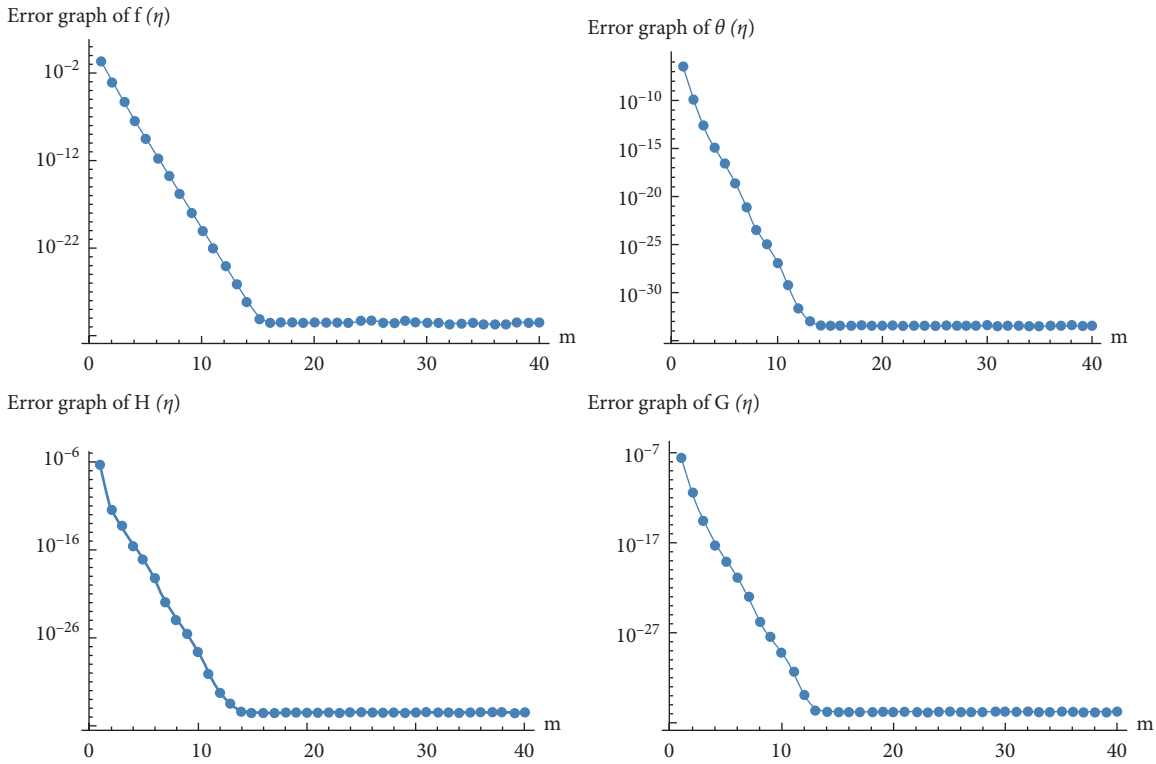

FIGURE 2: Error analysis on $f(\eta)$, $\theta(\eta)$, $G(\eta)$, and $H(\eta)$ with $P_r = -0.5$, $S = -0.5$, $L = 0.01$, $Q = 5$, $R = 0.7$, $\delta = 1$, $Sc = 2.5$, $K1 = 0.1$, $K2 = 1$, and $Ha = 0.1$.

TABLE 1: Thermophysical properties of iron oxide, cobalt, and ethylene glycol with water at 20°C [7].

Physical properties	ρ (kg/m^3)	c_p (J/kgK)	k (W/mK)	$\beta \times 10^{-5}$ (K^{-1})	σ (sm^{-1})
Fe_3O_4	5180	670	9.7	1.3	0.74×10^6
Co (cobalt)	8900	420	100	1.3×10^{-5}	1.602×10^7
$C_2H_6O_2 - H_2O$	1056	3630	0.387	58	0.00509

TABLE 2: Total residual error of $f(\eta)$, $\theta(\eta)$, $G(\eta)$, and $H(\eta)$ with $P_r = -0.5$, $S = -0.5$, $L = 0.01$, $Q = 5$, $R = 0.7$, $\delta = 1$, $Sc = 2.5$, $K1 = 0.1$, $K2 = 1$, and $Ha = 0.1$.

n	$\epsilon^f n$	$\epsilon^\theta n$	$\epsilon^H n$	$\epsilon^G n$
1	0.186129	2.4373×10^{-7}	3.17987×10^{-7}	2.30094×10^{-9}
5	2.936895×10^{-10}	2.30705×10^{-17}	7.84948×10^{-18}	8.67775×10^{-20}
10	1.34057×10^{-20}	1.16169×10^{-27}	3.02765×10^{-28}	6.44809×10^{-30}
15	1.3174×10^{-30}	3.18812×10^{-34}	3.27408×10^{-35}	1.86574×10^{-36}
16	3.64848×10^{-31}	3.20099×10^{-34}	3.17778×10^{-35}	1.86574×10^{-36}
20	3.64848×10^{-31}	3.20099×10^{-34}	3.17778×10^{-35}	1.86574×10^{-36}
25	3.64848×10^{-31}	3.20099×10^{-34}	3.17778×10^{-35}	1.86574×10^{-36}
30	3.64848×10^{-31}	3.20099×10^{-34}	3.17778×10^{-35}	1.86574×10^{-36}
35	3.64848×10^{-31}	3.20099×10^{-34}	3.17778×10^{-35}	1.86574×10^{-36}
40	3.64848×10^{-31}	3.20099×10^{-34}	3.17778×10^{-35}	1.86574×10^{-36}

resolved using HAM and BVP4c numerical routines. The local skin friction coefficient as well as the local rates of heat and mass transfer at the surface of the squeezing plates, both of which are extremely important in terms of physical properties, is also computed. Because there are so many physical parameters in the current problem, a wide range of results can be obtained. The distributions of temperature, velocity, pressure, and mass transfer are obtained by solving (8)–(11) and are shown in Figures 1–10 for various physical parameters. The impact of the squeeze number S on the velocity and temperature distribution for both heating and cooling surfaces is plotted on $f(\eta)$, $f'(\eta)$, $\theta(\eta)$, $H(\eta)$, and $G(\eta)$ in Figure 5 in the case of both $Fe_3O_4 - C_2H_6O_2 - H_2O$ single nanofluids (SNF) and $Fe_3O_4 - Co/C_2H_6O_2 - H_2O$ hybrid nanofluids (HNF). The values of the squeeze number have been set to be higher than zero in this case, indicating

Table 3: Computation of nanoparticles (iron oxide, cobalt) and ethylene glycol for $f(\eta)$, $\theta(\eta)$, $H(\eta)$, and $G(\eta)$ with $P_r = 0.5$, $S = -0.5$, $L = 0.01$, $\delta = 1$, $Q = 0.01$, $R = 0.1$, $Sc = 2.5$, $K1 = 0.3$, $K2 = 0.1$, $Ha = 0.2$, $\phi = 0.02$, $\phi1 = \phi2 = 0.01$, $\rho1 = 5180$, $\rho2 = 8900$, $\rho3 = 1056$, $\sigma1 = 0.74 \times 10^6$, $\sigma2 = 1.602 \times 10^7$, and $\sigma3 = 0.00509$.

	HAM results				Numerical results			
η	$f(\eta)$	$\theta(\eta)$	$H(\eta)$	$G(\eta)$	$f(\eta)$	$\theta(\eta)$	$H(\eta)$	$G(\eta)$
0.0000	0.0000	1.0000	1.0193	0.1242	0.0000	1.0000	1.0193	0.1242
0.1001	0.0146	0.9229	1.0308	0.1106	0.0146	0.9229	1.0308	0.1106
0.2002	0.0542	0.8441	1.0447	0.0966	0.0542	0.8441	1.0447	0.0966
0.3003	0.1122	0.7621	1.0602	0.0825	0.1122	0.7621	1.0602	0.0825
0.4004	0.1820	0.6752	1.0757	0.0685	0.1820	0.6752	1.0757	0.0685
0.5005	0.2570	0.5822	1.0892	0.0550	0.2570	0.5822	1.0892	0.0550
0.6006	0.3310	0.4820	1.0980	0.0422	0.3310	0.4820	1.0980	0.0422
0.7007	0.3978	0.3736	1.0986	0.0301	0.3978	0.3736	1.0986	0.0301
0.8008	0.4517	0.2567	1.0865	0.0189	0.4517	0.2567	1.0865	0.0189
0.9009	0.4873	0.1315	1.0560	0.0088	0.4873	0.1315	1.0560	0.0088
0.0000	0.5000	0.0000	1.0000	0.0000	0.5000	0.0000	1.0000	0.0000

Table 4: Convergence of homotopy solution for different orders of calculation of nanoparticles (iron oxide, cobalt) and ethylene glycol for $f''(\eta)$, $-\theta'(\eta)$, $-H'(\eta)$, and $-G'(\eta)$ with $P_r = 0.5$, $S = -0.5$, $L = 0.01$, $\delta = 1$, $Q = 0.01$, $R = 0.1$, $Sc = 2.5$, $K1 = 0.3$, $K2 = 0.1$, $Ha = 0.2$, $\phi = 0.02$, $\phi1 = \phi2 = 0.01$, $\rho1 = 5180$, $\rho2 = 8900$, $\rho3 = 1056$, $\sigma1 = 0.74 \times 10^6$, $\sigma2 = 1.602 \times 10^7$, and $\sigma3 = 0.00509$.

η	$f''(0)$	$-\theta'(0)$	$-H'(0)$	$-G'(0)$
0.0000	3.1331	0.7679	−0.1019	0.1019
0.1001	2.4908	0.7758	−0.1279	0.0911
0.2002	1.8362	0.8006	−0.1486	0.0800
0.3003	1.1779	0.8413	−0.1576	0.0689
0.4004	0.5255	0.8963	−0.1490	0.0579
0.5005	−0.1106	0.9637	0.1166	0.0472
0.6066	−0.7555	1.0459	0.0484	0.0362
0.7007	−1.2931	1.1247	0.0492	0.0268
0.8008	−1.8216	1.2101	0.2020	0.0173
0.9009	−2.2987	1.2912	0.4208	0.0082
1.0000	−2.7161	1.3595	0.7259	0.0000

Table 5: Computation of nanoparticles (iron oxide and ethylene glycol) and hybrid nanoparticles (iron oxide, cobalt, and ethylene glycol with water) for skin friction $f''(0)$.

Different fluid model parameters			Nanoparticles	Hybrid nanoparticles
S	Ha	ϕ	$f''(0)$	$f''(0)$
−0.5	1	0.1	0.057180	3.083700
−1			0.053850	3.077570
−1.5			0.050680	3.072110
−2	1		3.057180	3.028170
	3		3.057180	3.028170
	5		3.057180	3.028170
	7	0.1	3.019960	3.029040
		0.2	3.019620	3.028170
		0.3	3.019160	3.026870

that the upper plate is moving away from the lower stationary plate and the opposite inequality of the squeeze number indicating that the lower plate is moving away from the upper plate. Effect of S on $f(\eta)$ and $f'(\eta)$ is depicted in Figure 3 in the case of both SNF and HNF. In reality, for larger S, the upper plate slides downward, which puts more stress on nanoparticles, and consequently velocity components $f(\eta)$, $f'(\eta)$ are amplified. Effect of S on $\theta(\eta)$ is demonstrated in Figure 3. For bigger S, the top plate shift downwards, and interatomic collision nanoparticles increase; hence, the temperature increases. The influence on concentration profiles $H(\eta)$ and $G(\eta)$ of the parameter S can be observed in Figure 3 in both SNF and HNF. The concentration profile $H(\eta)$ decreases and $G(\eta)$ increases. It has been discovered that as S increases, the homogeneous chemical reaction increases, resulting in a decrease in viscosity. However, the $H(\eta)$ indicates the reverse of the $G(\eta)$ above can seen in Figure 3. The impact of Hartmann number Ha show in Figure 3 on $f(\eta)$ against the similarity variable η for the phenomenon of both SNF and HNF are decreases. When the HNF flow is applied, the fluid velocity is reduced by moving down the horizontal axis and the SNF flow

Table 6: Computation of nanoparticles (iron oxide and ethylene glycol) and hybrid nanoparticles (iron oxide, cobalt) and ethylene glycol with water for Nusselt number $-\theta'(0)$.

Different fluid model parameters					Nanoparticles	Hybrid nanoparticles
S	P_r	Q	R	ϕ	$-\theta'(0)$	$-\theta'(0)$
−0.5	1	1	1	0.1	1.101390	1.101380
−1					1.201800	1.201760
−1.5					1.301230	1.301160
−2	1				1.201810	1.201790
	2				1.399750	1.399710
	3				1.593820	1.593760
	4	1			1.008540	1.008530
		2			1.039600	1.039590
		3			1.070550	1.070540
		4	1		1.094100	1.094100
			2		1.079550	1.079550
			3		1.064990	1.064990
			4	0.1	1.054580	1.054580
				0.2	1.054580	1.054580
				0.3	1.054580	1.054580

Table 7: Computation of nanoparticles (iron oxide and ethylene glycol) and hybrid nanoparticles (iron oxide, cobalt) and ethylene glycol with water for Sherwood numbers (homogeneous-heterogeneous) $H''(0)$ and $G''(0)$.

Variation in parameters					Nanoparticles		Hybrid nanoparticles	
S	Sc	$k1$	$k2$	ϕ	$-H'(0)$	$-G'(0)$	$-H'(0)$	$-G'(0)$
−0.5	1	0.1	1	0.1	−0.333233	0.167006	−0.333230	0.167016
−1					−0.332977	0.167346	−0.332968	0.167332
0.5					−0.332720	0.167686	−0.332700	0.167680
−2	1				−0.333233	0.167006	−0.333230	0.167005
	2				−0.333135	0.167346	−0.333129	0.167345
	3				−0.333038	0.167688	−0.333029	0.167686
	4	0.1			−0.333283	0.166396	−0.333286	0.166396
		0.2			−0.332976	0.166531	−0.332979	0.166532
		0.3			−0.332669	0.166531	−0.332672	0.166667
		0.4	1		−0.499141	0.249089	−0.499141	0.249089
			6		−0.852392	0.430977	−0.852392	0.430977
			11		−0.911060	0.460473	−0.911060	0.460473
			4	0.1	−0.333387	0.166454	−0.333387	0.166454
				0.2	−0.333387	0.166454	−0.333387	0.166454
				0.3	−0.333387	0.166454	−0.333387	0.166454

Table 8: Computation for $f''(0)$, $-\theta'(0)$, $-H'(0)$, and $-G'(0)$ with $P_r = 0.5$, $S = -0.5$, $L = 0.01$, $\delta = 1$, $Q = 0.01$, $R = 0.1$, $Sc = 2.5$, $K1 = 0.3$, $K2 = 0.1$, $Ha = 0.2$, $\phi = 0.02$, $\phi1 = \phi2 = 0.01$, $\rho1 = 5180$, $\rho2 = 8900$, $\rho3 = 1056$, $\sigma1 = 0.74 \times 10^6$, $\sigma2 = 1.602 \times 10^7$, and $\sigma3 = 0.00509$ and varied values of S.

HAM results					Numerical results			
S	$f''(0)$	$-\theta'(0)$	$-H'(0)$	$-G'(0)$	$f''(0)$	$-\theta'(0)$	$-H'(0)$	$-G'(0)$
−1.1	3.1283	0.8762	−0.1209	0.1209	3.1283	0.8762	−0.1209	0.1209
−1.2	3.1357	0.8641	−0.1324	0.1324	3.1357	0.8641	−0.1324	0.1324
−1.3	3.1443	0.8519	−0.1411	0.1411	3.1443	0.8519	−0.1411	0.1411
−1.4	3.1540	0.8395	−0.1515	0.1515	3.1540	0.8395	−0.1515	0.1515

Table 9: Computation for $f''(0)$, $-\theta'(0)$, $-H'(0)$, and $-G'(0)$ with $P_r = 0.5$, $S = -0.5$, $L = 0.01$, $\delta = 1$, $Q = 0.01$, $R = 0.1$, $Sc = 2.5$, $K1 = 0.3$, $K2 = 0.1$, $Ha = 0.2$, $\phi = 0.02$, $\phi1 = \phi2 = 0.01$, $\rho1 = 5180$, $\rho2 = 8900$, $\rho3 = 1056$, $\sigma1 = 0.74 \times 10^6$, $\sigma2 = 1.602 \times 10^7$, and $\sigma3 = 0.00509$ and varied values of P_r.

HAM results					Numerical results			
P_r	$f''(0)$	$-\theta'(0)$	$-H'(0)$	$-G'(0)$	$f''(0)$	$-\theta'(0)$	$-H'(0)$	$-G'(0)$
0.5	3.1059	1.2983	−0.0996	0.0398	3.1059	1.2983	−0.0996	0.0398
0.6	3.1059	1.3545	−0.0996	0.0398	3.1059	1.3545	−0.0996	0.0398
0.7	3.1059	1.4096	−0.0996	0.0398	3.1059	1.4096	−0.0996	0.0398
0.8	3.1059	1.4638	−0.0996	0.0398	3.1059	1.4638	−0.0996	0.0398

Table 10: Computation for $f''(0)$, $-\theta'(0)$, $-H'(0)$, and $-G'(0)$ with $P_r = 0.5$, $S = -0.5$, $L = 0.01$, $\delta = 1$, $Q = 0.01$, $R = 0.1$, $Sc = 2.5$, $K1 = 0.3$, $K2 = 0.1$, $Ha = 0.2$, $\phi = 0.02$, $\phi1 = \phi2 = 0.01$, $\rho1 = 5180$, $\rho2 = 8900$, $\rho3 = 1056$, $\sigma1 = 0.74 \times 10^6$, $\sigma2 = 1.602 \times 10^7$, and $\sigma3 = 0.00509$ and varied values of δ.

	HAM results				Numerical results			
δ	$f''(0)$	$-\theta'(0)$	$-H'(0)$	$-G'(0)$	$f''(0)$	$-\theta'(0)$	$-H'(0)$	$-G'(0)$
1	3.1059	1.2983	−0.0994	0.0994	3.1059	1.2983	−0.0994	0.0994
2	3.1059	1.2983	−0.0996	0.0398	3.1059	1.2983	−0.0996	0.0398
3	3.1059	1.2983	−0.0996	0.0332	3.1059	1.2983	−0.0996	0.0332
4	3.1059	1.2983	−0.0996	0.0249	3.1059	1.2983	−0.0996	0.0249

Table 11: Computation for $f''(0)$, $-\theta'(0)$, $-H'(0)$, and $-G'(0)$ with $P_r = 0.5$, $S = -0.5$, $L = 0.01$, $\delta = 1$, $R = 0.1$, $Sc = 2.5$, $K1 = 0.3$, $K2 = 0.1$, $Ha = 0.2$, $\phi = 0.02$, $\phi1 = \phi2 = 0.01$, $\rho1 = 5180$, $\rho2 = 8900$, $\rho3 = 1056$, $\sigma1 = 0.74 \times 10^6$, $\sigma2 = 1.602 \times 10^7$, and $\sigma3 = 0.00509$ and varied values of Q.

	HAM results				Numerical results			
Q	$f''(0)$	$-\theta'(0)$	$-H'(0)$	$-G'(0)$	$f''(0)$	$-\theta'(0)$	$-H'(0)$	$-G'(0)$
0.01	3.1059	0.9457	−0.0994	0.0994	3.1059	0.9457	−0.0994	0.0994
0.02	3.1059	0.9465	−0.0994	0.0994	3.1059	0.9465	−0.0994	0.0994
0.03	3.1059	0.9472	−0.0994	0.0994	3.1059	0.9472	−0.0994	0.0994
0.04	3.1059	0.9480	−0.0994	0.0994	3.1059	0.9480	−0.0994	0.0994

Table 12: Computation for $f''(0)$, $-\theta'(0)$, $-H'(0)$, and $-G'(0)$ with $P_r = 0.5$, $S = -0.5$, $L = 0.01$, $\delta = 1$, $Q = 0.01$, $R = 0.1$, $Sc = 2.5$, $K1 = 0.3$, $K2 = 0.1$, $Ha = 0.2$, $\phi = 0.02$, $\phi1 = \phi2 = 0.01$, $\rho1 = 5180$, $\rho2 = 8900$, $\rho3 = 1056$, $\sigma1 = 0.74 \times 10^6$, $\sigma2 = 1.602 \times 10^7$, and $\sigma3 = 0.00509$ and varied values of R.

	HAM results				Numerical results			
R	$f''(0)$	$-\theta'(0)$	$-H'(0)$	$-G'(0)$	$f''(0)$	$-\theta'(0)$	$-H'(0)$	$-G'(0)$
0.1	3.1059	0.9457	−0.0994	0.0994	3.1059	0.9457	−0.0994	0.0994
0.2	3.1059	0.9515	−0.0994	0.0994	3.1059	0.9515	−0.0994	0.0994
0.3	3.1059	0.9562	−0.0994	0.0994	3.1059	0.9562	−0.0994	0.0994
0.4	3.1059	0.9601	−0.0994	0.0994	3.1059	0.9601	−0.0994	0.0994

velocity is increased for continued positive changes in Ha values while the same behavior is displayed as in the figure, for both situations. It is also found that the maximum velocity of HNF is greater than that of SNF. The impact on the temperature profile of the Prandtl number P_r is seen in Figure 4. It is examined to show $\theta(\eta)$ in the case of SNF and the inclining performance for high values of P_r in the case of HNF. Essentially, larger P_r values enhance the boundary layer thickness that stimulates the nanoparticle's cooling effect due to thermal diffusion ratio. As contrast to in the HNF nanoparticles are tightly packed SNF. The impact on the temperature profile of Q (heat generation parameter) is seen in Figure 4. For rising values of heat parameter Q, $T_u > T_l$ indicates a further transfer of heat from the surface into the fluid, thus raising the fluid temperature for both SNF and HNF. The growing temperature behavior in SNF and HNF for the larger value of R is shown in Figure 4. However, it is commonly recognized that the heat transfer phenomena of their radiation process emit the energy via fluid particles, so that more heat is created during flow. Thus, the thermal boundary layer with more R is defined as a development. Figure 5 indicates a rise in the Schmidt number Sc for SNF and HNF concentration profile of $H(\eta)$ and $G(\eta)$ and, as a result, reduction in the thickness of concentration boundary layer. The reactant concentration is observed to be increasing at a quicker rate when the diffusion coefficient of species is reduced; i.e., higher Sc values lead to a more rapid increase of the flow field concentration. The impact of homogeneous parameter $k1$ and a heterogeneous parameter $k2$ on the concentration profile $H(\eta)$ can be seen in Figure 6. Increase in the concentration profiles $H(\eta)$ it is observed that due to increase in $k1$. According to this an increase in the homogeneous chemical reaction parameter which decreases viscosity. The concentration profile increases as the thickness of the boundary layer decreases for lower strength values of homogeneous reaction parameter. It is also proved that concentration profile is lower for the situation of HNF when compared with SNF. In both situations of SNF and HNF, the concentration boundary layer of the reactants decreases. However, they coincide for smaller values of η which physically means that the homogeneous and heterogeneous reactions have no effect on the concentration of the reactants. The strong conduct of heterogeneous reaction parameters $K2$ on the distribution is studied in Figure 6. The distribution of the concentration is increasing towards the surface of the plate and decreasing away from the surface with smaller values of $K2$. When compared to HNF, the concentration distribution is smaller (SNF). It is noticed in Figure 6 that the behavior of concentration profile $G(\eta)$ and $H(\eta)$ is opposite. This shows the effects of the homogeneous chemical reaction parameter $k1$ and the heterogeneous chemical reaction parameter $k2$ on

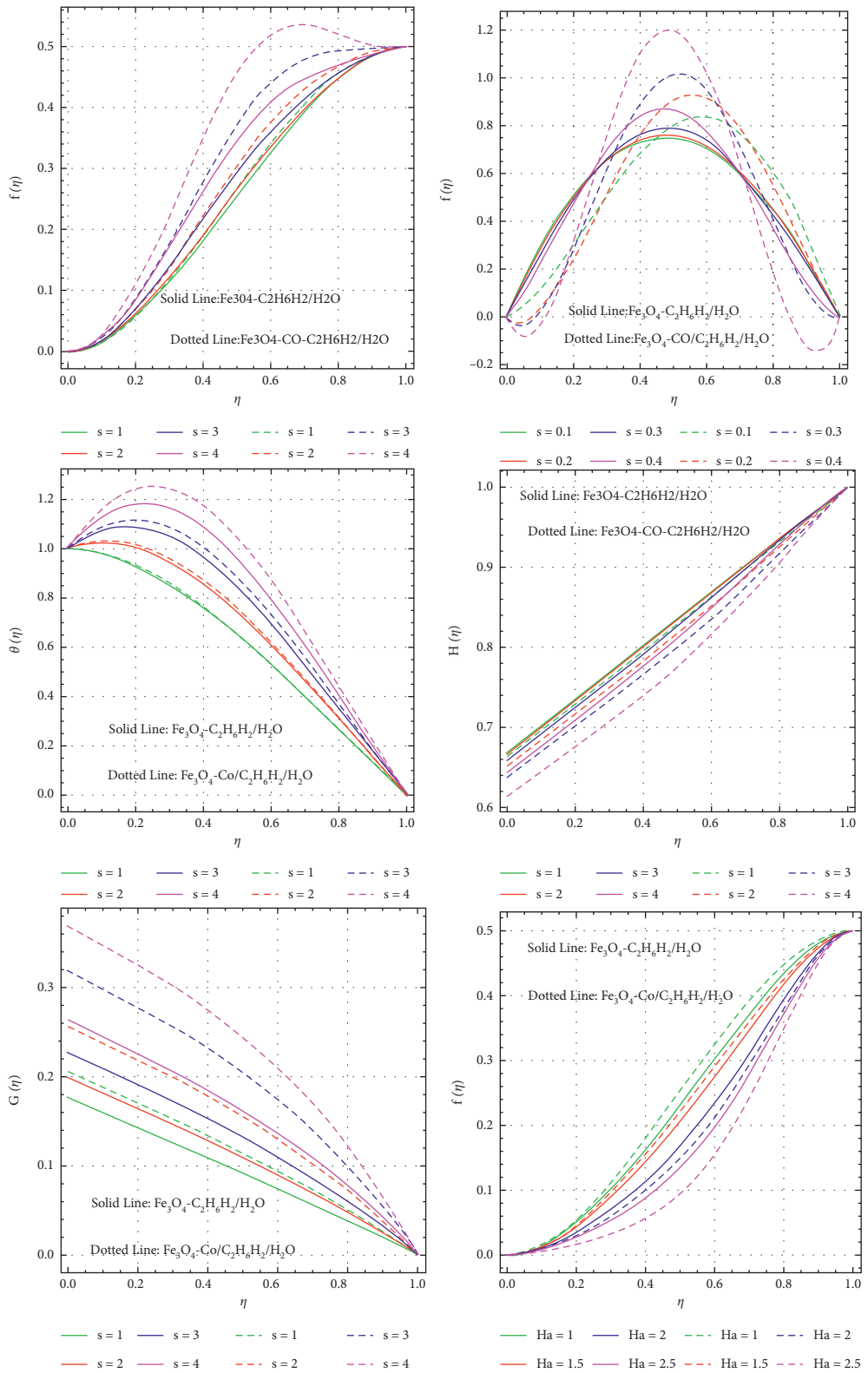

FIGURE 3: Impact of S for $Fe_3O_4 - C_2H_6O_2 - H_2O$ and $Fe_3O_4 - Co/C_2H_6O_2 - H_2O$ on $f(\eta)$, $f'(\eta)$, $\theta(\eta)$, $H(\eta)$, $G(\eta)$ and impact of Ha on $f(\eta)$ with $L = 2$, $\delta = 1$, $Q = 4$, $R = 2$, $Sc = P_r = Ha = K1 = K2 = 0.5$, $\phi = 0.02$, $\phi 1 = \phi 2 = 0.01$, $\rho 1 = 5180$, $\rho 2 = 8900$, $\rho 3 = 1056$, $\sigma 1 = 0.74 \times 10^6$, and $\sigma 2 = 1.602 \times 10^7$, $\sigma 3 = 0.00509$.

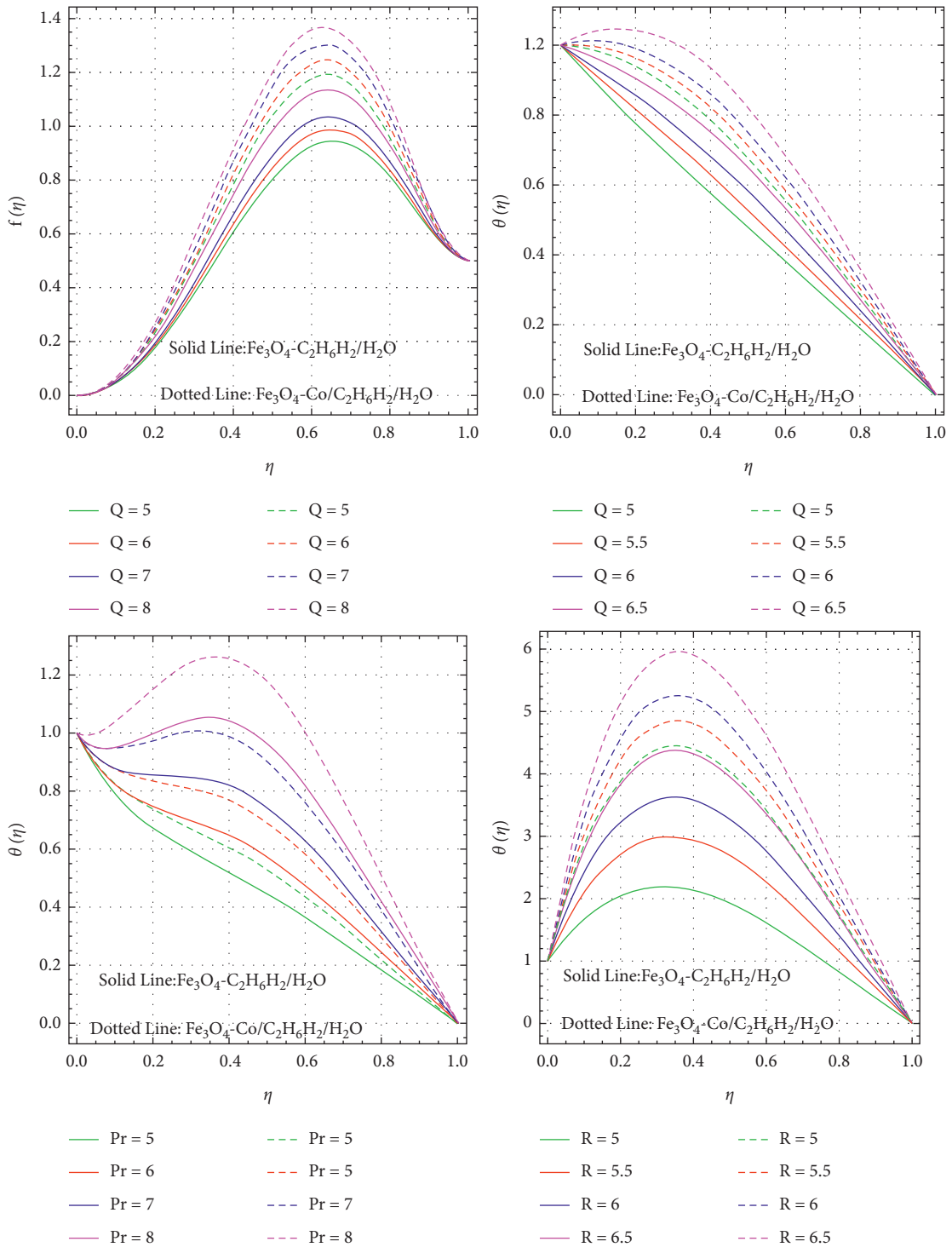

FIGURE 4: Impact of Q for $Fe_3O_4 - C_2H_6O_2 - H_2O$ and $Fe_3O_4 - Co/C_2H_6O_2 - H_2O$ on $f(\eta)$ and $\theta(\eta)$ and impacts of P_r and R on $\theta(\eta)$ with $L = 2$, $\delta = 1$, $Q = 4$, $R = 2$, $Sc = P_r = Ha = K1 = K2 = 0.5$, $\phi = 0.02$, $\phi 1 = \phi 2 = 0.01$, $\rho 1 = 5180$, $\rho 2 = 8900$, $\rho 3 = 1056$, $\sigma 1 = 0.74 \times 10^6$, $\sigma 2 = 1.602 \times 10^7$, and $\sigma 3 = 0.00509$.

the concentration profiles $H(\eta)$ and $G(\eta)$. It has been observed that increasing $k1$ causes the concentration profiles $H(\eta)$ and $G(\eta)$ to increase. This is due to the fact that as the homogeneous chemical reaction parameter rises, the viscosity declines. However, the heterogeneous parameter $k2$ yields the opposite result, as shown in Figure 6. This is because as $k2$ increases, diffusion decreases, and the concentration of less diffused particles grows. The impacts of nanoparticles volume fraction ϕ on the velocity profiles $f(\eta)$, $\theta(\eta)$, $H(\eta)$, and $G(\eta)$ in case of SNF and HNF are shown in Figure 7. It can be clearly seen that the volume fraction parameter ϕ is increased with the increase in the

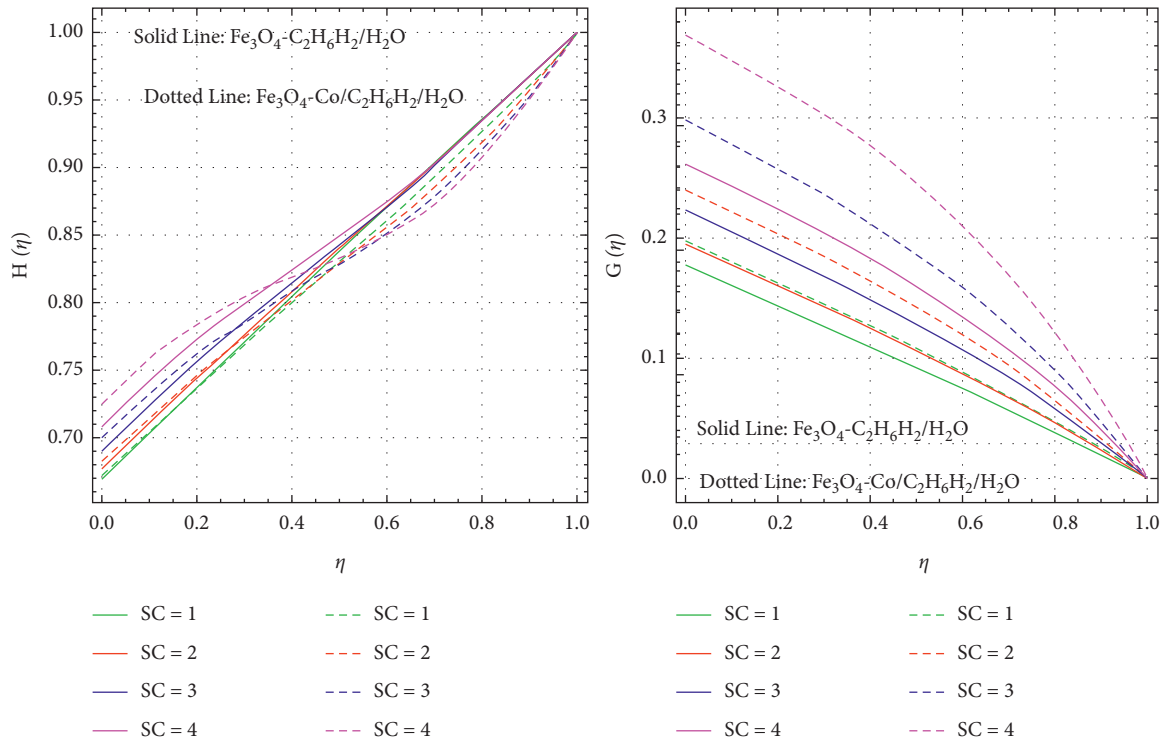

Figure 5: Impact of Sc for $Fe_3O_4 - C_2H_6O_2 - H_2O$ and $Fe_3O_4 - Co/C_2H_6O_2 - H_2O$ on $H(\eta)$ and $G(\eta)$ with $L = 2$, $\delta = 1$, $Q = 4$, $R = 2$, $S = P_r = Ha = K1 = K2 = 0.5$, $\phi = 0.02$, $\phi1 = \phi2 = 0.01$, $\rho1 = 5180$, $\rho2 = 8900$, $\rho3 = 1056$, $\sigma1 = 0.74 \times 10^6$, $\sigma2 = 1.602 \times 10^7$, and $\sigma3 = 0.00509$.

velocity for both SNF and HNF. In this physical problem the increase in velocity is because of the converse relationship that exists between the dynamic viscosity of nanofluid and the volume fraction. Consequently, the consistency of regular liquid is reduced against an increase in ϕ, and therefore the fluid flow is supported up. The quantities related to the local coefficient of skin friction, the local Nusselt number, and the Sherwood number (homogeneous-heterogeneous reactions), that is, $f(\eta)$, $\theta(\eta)$, $H(\eta)$, and $G(\eta)$, for various values of ϕ are depicted in Figure 7. The values of $f(\eta)$ increase with increasing ϕ, whereas the heat transfer rate $\theta(\eta)$ decreases. The values of homogeneous $H(\eta)$ increase with the increase in ϕ, whereas the values of heterogeneous $G(\eta)$ decrease. It is also seen from these figures that the values of $f(\eta)$, $\theta(\eta)$, $H(\eta)$, and $G(\eta)$ are always positive. The influence on concentration profiles $f(\eta)$, $\theta(\eta)$, $H(\eta)$, and $G(\eta)$ of the parameter S can be observed in Figure 8 in nanoparticles. All the concentration profiles are increased while $G(\eta)$ decreases, it is observed that due to increase in S. Figure 9 indicates that the $f(\eta)$ and $H(\eta)$ concentration profiles have increased with rising values of Schmidt number Sc, while $\theta(\eta)$ and $G(\eta)$ decrease. Figure 10 displays the effects of the homogeneous and heterogeneous chemical reaction parameters $k1$ and $k2$ on the concentration profiles $f(\eta)$, $H(\eta)$, and $G(\eta)$. It has been observed that $k1$ increases and $k2$ decreases on the concentration profile $f(\eta)$; both decrease on the concentration profile $H(\eta)$; and both increase on $G(\eta)$. The purpose of Tables 5–12 is to test the impact of various physical parameters numerically. As can be seen from the tables, all of the results are in good settlement with the BVP4c and HAM results. It is observed that effects of skin friction coefficient, velocity, temperature, and Nusselt and Sherwood numbers, both homogeneous as well as the heterogeneous parameters cause increment in the mass transfer rate. A decrease in the skin friction coefficient, as well as the heat and mass transfer rate, is caused by an increment in the internal heat generation parameter. A similar set of results has been observed when the squeezing parameter S is increased. As the squeezing parameter S is enhanced, the friction factor reduces and the local Nusselt and Sherwood numbers increase. The skin friction coefficient showed a downward trend, showing that the fluid was being drawn by the floor. Tables 3–12, respectively, show the results of $f(\eta)$, $\theta(\eta)$, $H(\eta)$, $G(\eta)$, $f'(\eta)$, $-\theta'(\eta)$, $-H'(\eta)$, and $-G'(\eta)$.

It is acknowledged from Table 5 that perhaps the skin friction factor $f'(\eta)$ tends to increase the squeezing number S; the disruptive effect can be seen for the Hartmann number Ha and the volume fraction ϕ of nanoparticles and hybrid nanoparticles. From Table 6, it has been noticed that the squeezing number S has declining influence on heat transfer efficiency, but Prandtl number P_r, Q (heat generation parameter), radiation R, and volume fraction ϕ of nanoparticles and hybrid nanoparticles are greatly influencing the heat transfer efficiency. Table 7 depicts the behavior of nanoparticles and hybrid nanoparticles on $-H'(\eta)$ and $-G'(\eta)$ when $\delta = 1$. It shows the decreasing values of $-H'(\eta)$ and increasing values of squeezing number S, Schmidt number Sc, and homogeneous reaction strength $K1$, but values of

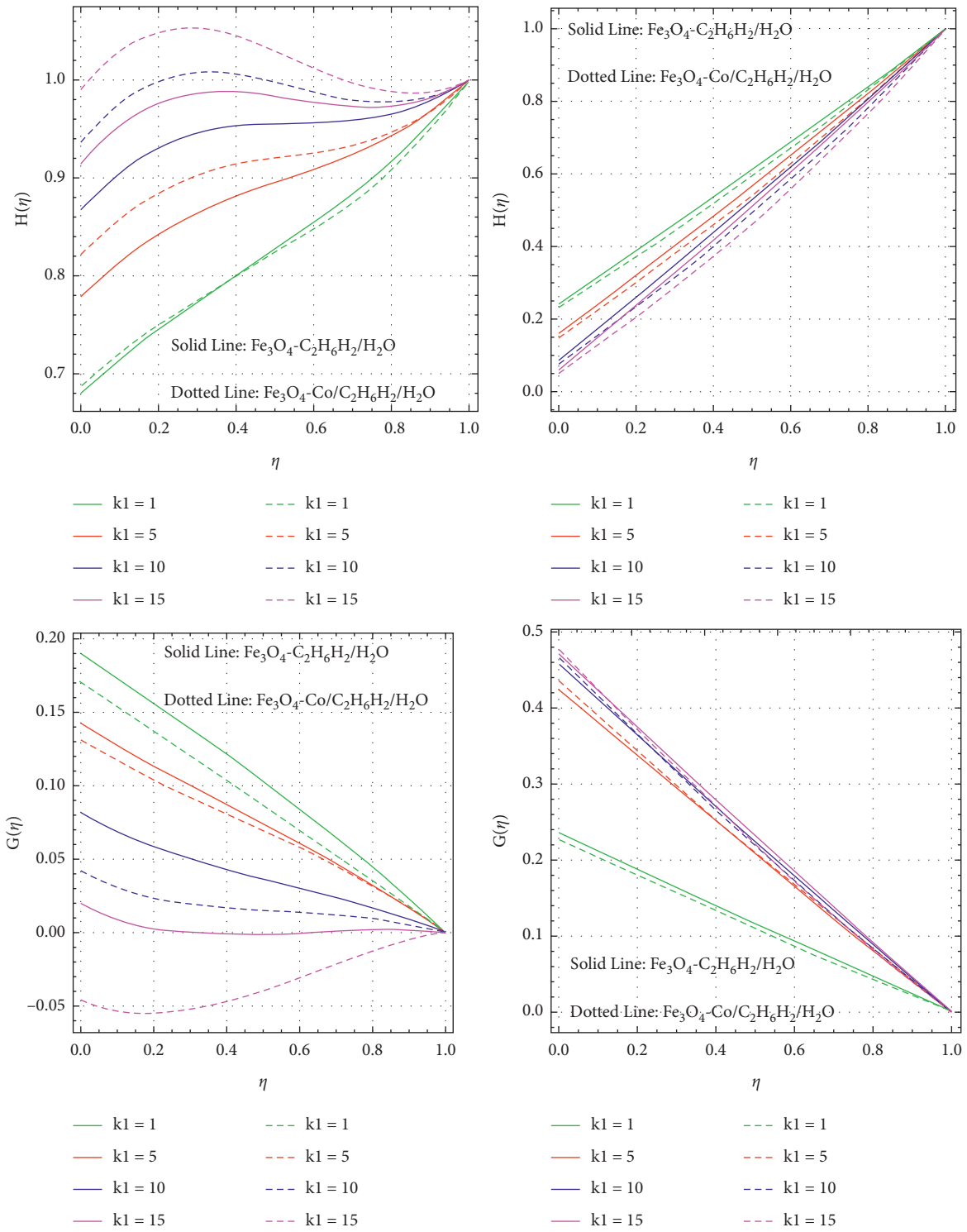

FIGURE 6: Impact of $K1$ and $K2$ for $Fe_3O_4 - C_2H_6O_2 - H_2O$ and $Fe_3O_4 - Co/C_2H_6O_2 - H_2O$ on $H(\eta)$ and $G(\eta)$ with $L = 2$, $\delta = 1$, $Q = 4$, $R = 2$, $Sc = P_r = Ha = 0.5$, $\phi = 0.02$, $\phi 1 = \phi 2 = 0.01$, $\rho 1 = 5180$, $\rho 2 = 8900$, $\rho 3 = 1056$, $\sigma 1 = 0.74 \times 10^6$, $\sigma 2 = 1.602 \times 10^7$, and $\sigma 3 = 0.00509$.

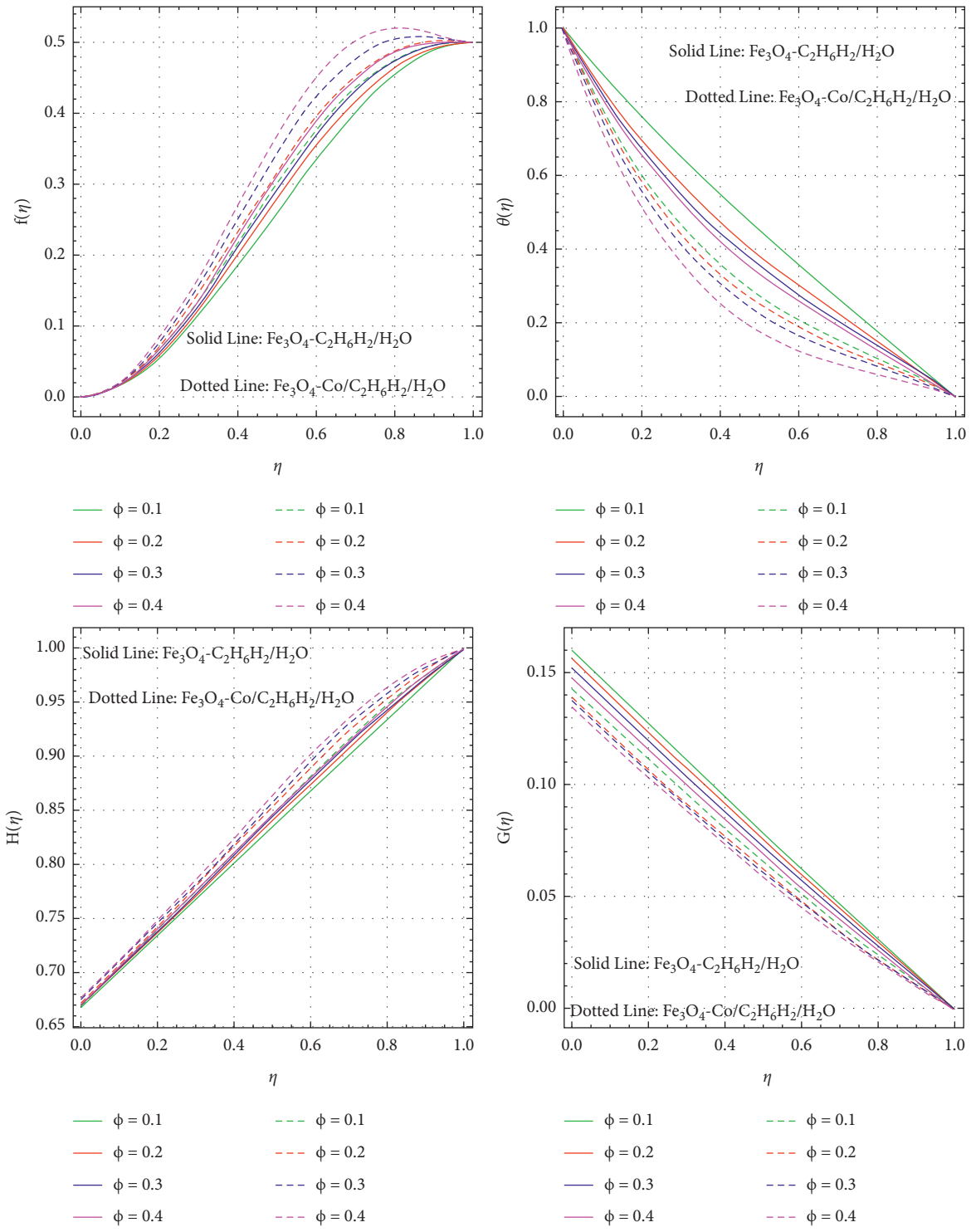

Figure 7: Impact of ϕ for $Fe_3O_4 - C_2H_6O_2 - H_2O$ and $Fe_3O_4 - Co/C_2H_6O_2 - H_2O$ on $f(\eta)$, $\theta(\eta)$, $H(\eta)$, and $G(\eta)$ with $L = 2$, $\delta = 1$, $Q = 4$, $R = 2$, $Sc = P_r = Ha = K1 = K2 = 0.5$, $\phi = 0.02$, $\phi 1 = \phi 2 = 0.01$, $\rho 1 = 5180$, $\rho 2 = 8900$, $\rho 3 = 1056$, $\sigma 1 = 0.74 \times 10^6$, $\sigma 2 = 1.602 \times 10^7$, and $\sigma 3 = 0.00509$.

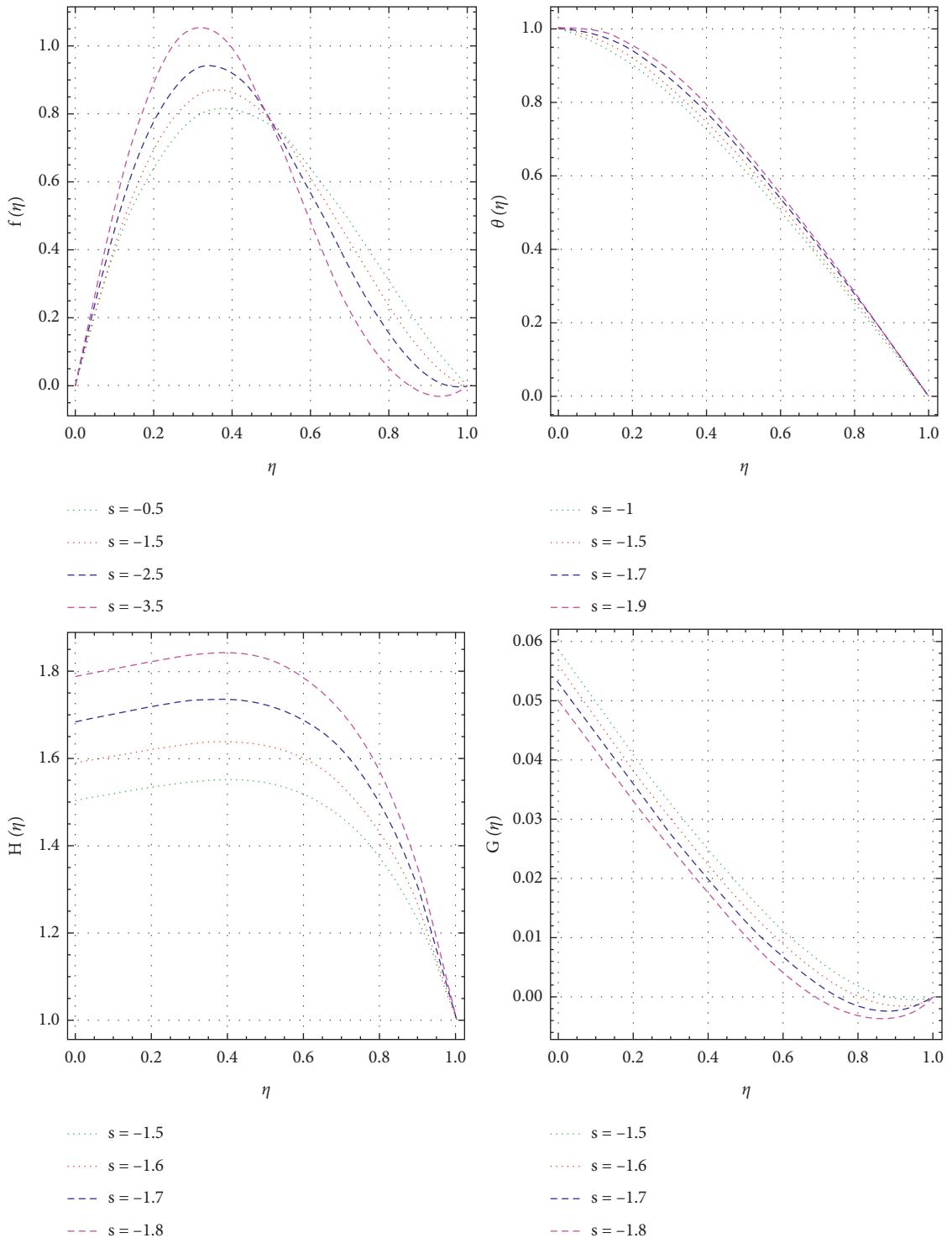

Figure 8: Impact of S on $f(\eta)$, $\theta(\eta)$, $H(\eta)$, and $G(\eta)$ with $P_r = 0.5$, $S = -0.5$, $L = 0.01$, $\delta = 1$, $Q = 0.01$, $R = 0.1$, $Sc = 2.5$, $K1 = 0.3$, $K2 = 0.1$, $Ha = 0.2$, $\phi = 0.02$, $\phi 1 = \phi 2 = 0.01$, $\rho 1 = 5180$, $\rho 2 = 8900$, $\rho 3 = 1056$, $\sigma 1 = 0.74 \times 10^6$, $\sigma 2 = 1.602 \times 10^7$, and $\sigma 3 = 0.00509$.

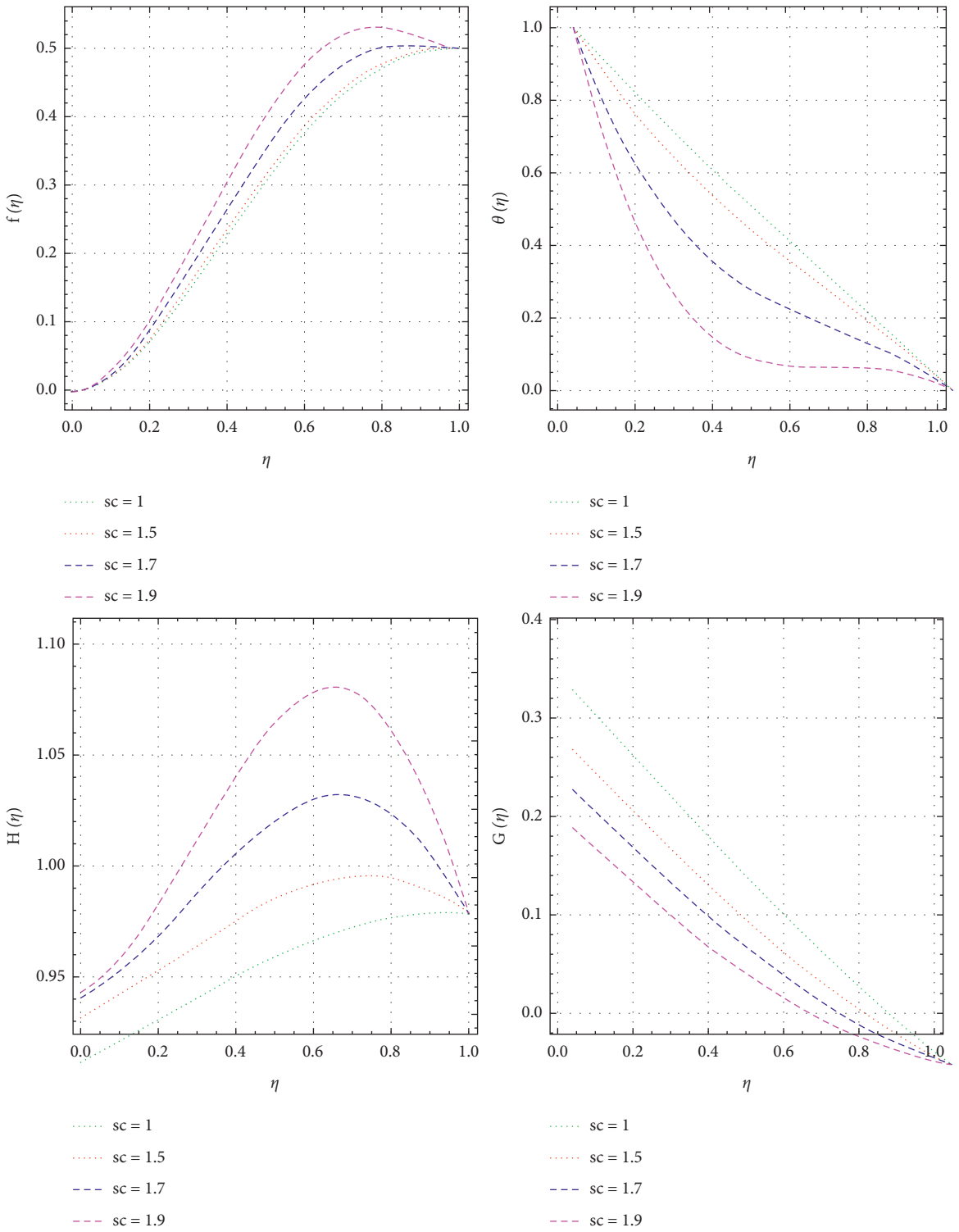

FIGURE 9: Impact of Sc on $f(\eta)$, $\theta(\eta)$, $H(\eta)$, and $G(\eta)$ with $P_r = 0.5$, $S = -0.5$, $L = 0.01$, $R = 1$, $Ha = 0.1$, $Sc = 2.5$, $K1 = 0.3$, $K2 = 0.1$, $\delta = 1$, $\phi = 0.02$, $\phi 1 = \phi 2 = 0.01$, $\rho 1 = 5180$, $\rho 2 = 8900$, $\rho 3 = 1056$, $\sigma 1 = 0.74 \times 10^6$, $\sigma 2 = 1.602 \times 10^7$, and $\sigma 3 = 0.00509$.

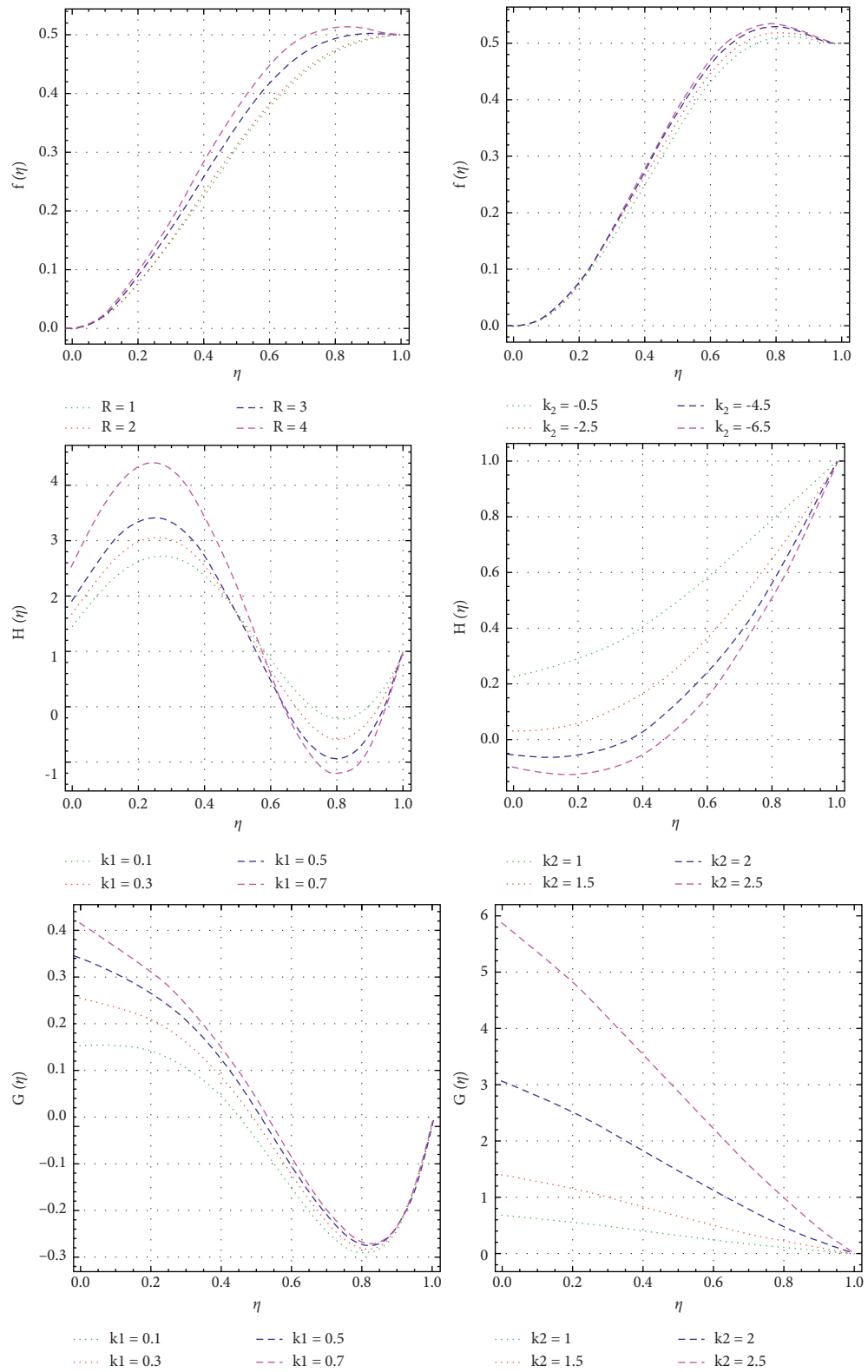

Figure 10: Impact of $K1$ and $K2$ on $f(\eta)$, $H(\eta)$, and $G(\eta)$ with $P_r = 1$, $S = -5$, $L = 0.5$, $Q = 5$, $R = 1$, $\delta = 1$, $Sc = 2.5$, $K1 = 5$, $K2 = 5$, $Ha = 0.5$, $\phi = 0.02$, $\phi 1 = \phi 2 = 0.01$, $\rho 1 = 5180$, $\rho 2 = 8900$, $\rho 3 = 1056$, $\sigma 1 = 0.74 \times 10^6$, $\sigma 2 = 1.602 \times 10^7$, and $\sigma 3 = 0.00509$.

Table 13: Computation for $f''(0)$, $-\theta'(0)$, $-H'(0)$, and $-G'(0)$ with $P_r = 0.5$, $S = -0.5$, $L = 0.01$, $\delta = 1$, $Q = 0.01$, $R = 0.1$, $Sc = 2.5$, $K1 = 0.3$, $K2 = 0.1$, $Ha = 0.2$, $\phi = 0.02$, $\phi1 = \phi2 = 0.01$, $\rho1 = 5180$, $\rho2 = 8900$, $\rho3 = 1056$, $\sigma1 = 0.74 \times 10^6$, $\sigma2 = 1.602 \times 10^7$, and $\sigma3 = 0.00509$ and varied values of Sc.

	HAM results				Numerical results			
Sc	$f''(0)$	$-\theta'(0)$	$-H'(0)$	$-G'(0)$	$f''(0)$	$-\theta'(0)$	$-H'(0)$	$-G'(0)$
2.5	3.1059	0.9457	−0.0994	0.0994	3.1059	0.9457	−0.0994	0.0994
3.5	3.1059	0.9457	−0.1044	0.1044	3.1059	0.9457	−0.1044	0.1044
4.5	3.1059	0.9457	−0.1106	0.1106	3.1059	0.9457	−0.1106	0.1106
5.5	3.1059	0.9457	−0.1200	0.1200	3.1059	0.9457	−0.1200	0.1200

Table 14: Computation for $f''(0)$, $-\theta'(0)$, $-H'(0)$, and $-G'(0)$ with $P_r = 0.5$, $S = -10$, $L = 0.01$, $\delta = 1$, $Q = 0.01$, $R = 0.1$, $Sc = 2.5$, $K2 = 0.1$, $Ha = 0.2$, $\phi = 0.02$, $\phi1 = \phi2 = 0.01$, $\rho1 = 5180$, $\rho2 = 8900$, $\rho3 = 1056$, $\sigma1 = 0.74 \times 10^6$, $\sigma2 = 1.602 \times 10^7$, and $\sigma3 = 0.00509$ and varied values of $K1$.

	HAM results				Numerical results			
$K1$	$f''(0)$	$-\theta'(0)$	$-H'(0)$	$-G'(0)$	$f''(0)$	$-\theta'(0)$	$-H'(0)$	$-G'(0)$
1.1	3.1059	0.9457	−0.0994	0.0994	3.1059	0.9457	−0.0994	0.0994
1.5	3.1059	0.9457	−0.0995	0.0995	3.1059	0.9457	−0.0995	0.0995
1.9	3.1059	0.9457	−0.0997	0.0997	3.1059	0.9457	−0.0997	0.0997
2.5	3.1059	0.9457	−0.0999	0.0999	3.1059	0.9457	−0.0999	0.0999

Table 15: Computation for $f''(0)$, $-\theta'(0)$, $-H'(0)$, and $-G'(0)$ with $P_r = 0.5$, $S = -10$, $L = 0.01$, $\delta = 1$, $Q = 0.01$, $R = 0.1$, $Sc = 2.5$, $K1 = 0.3$, $Ha = 0.2$, $\phi = 0.02$, $\phi1 = \phi2 = 0.01$, $\rho1 = 5180$, $\rho2 = 8900$, $\rho3 = 1056$, $\sigma1 = 0.74 \times 10^6$, $\sigma2 = 1.602 \times 10^7$, and $\sigma3 = 0.00509$ and varied values of $K2$.

	HAM results				Numerical results			
$K2$	$f''(0)$	$-\theta'(0)$	$-H'(0)$	$-G'(0)$	$f''(0)$	$-\theta'(0)$	$-H'(0)$	$-G'(0)$
0.01	3.1059	0.9457	−0.0994	0.0994	3.1059	0.9457	−0.0994	0.0994
0.02	3.1059	0.9457	−0.1758	0.1758	3.1059	0.9457	−0.1758	0.1758
0.03	3.1059	0.9457	−0.2362	0.2362	3.1059	0.9457	−0.2362	0.2362
0.04	3.1059	0.9457	−0.2850	0.2850	3.1059	0.9457	−0.2850	0.2850

heterogeneous reaction strength $k2$, for both $-H'(\eta)$ and $-G'(\eta)$, show incremental behavior. The volume fraction ϕ of nanoparticles and hybrid nanoparticles has the same values' behavior.

7. Conclusion

This investigation gives a mathematical answer for dissecting the impacts of flow between two squeezing plates with a homogeneous and heterogeneous reaction in the presence of hybrid nanoparticles. The impact of dimensional overseeing boundaries on velocity, temperature, profiles with skin friction, and local Nusselt and Sherwood numbers is examined with the assistance of graphs and tables. The effects of the current examination are listed below:

(i) The skin friction coefficient augmenting for growing values of solid volume fraction ϕ.

(ii) The increasing values of the squeezing parameter S reduced the friction factor and local Nusselt numbers, but from Table 7 Sherwood numbers are decreasing and increasing on the $-H(0)$ and $-G(0)$.

(iii) The Prandtl number, heat generation, and radiation parameters appear to increase in the local Nusselt numbers, as shown in Tables 9, 11, and 12.

(iv) Homogeneous-heterogeneous parameters assist in observing the flow's utility profiles.

(v) The local Nusselt and friction factor in fluid viscosity are similar as Sc increases and the homogeneous parameter decreases while heterogeneous parameter increases, as shown in Table 13.

(vi) Tables 14 and 15 show that homogeneous reaction strength and heterogeneous reaction strength are decreasing and increasing on the profile of $-H(0)$ and $-G(0)$.

Nomenclature

T: Temperature
T_u: Upper plate's temperature
T_l: Lower plate's temperature
P: Pressure
ρ_{hnf}: Effective density
$(\rho c_p)_{hnf}$: Effective heat capacity
σ_{hnf}: Electrical conductivity of nanofluid
u, v: Nanofluid velocity
D_A, D_B: Diffusion coefficients of the chemical species
δ: Ratio of the diffusion coefficients
K^*: Permeability
k_{hnf}: Nanofluid thermal conductivity

K_1: Homogeneous reaction strength
K_2: Heterogeneous reaction strength
S: Squeeze number
P_r: Prandtl number
Ha: Hartmann number
R: Radiation parameter
Q: Heat generation parameter
L: Length
C_f: Skin friction coefficient
Nu: Local Nusselt number
Sh: Local Sherwood number
$N1$, $N2$: Chemical species.

Data Availability

No data were used in this study.

Conflicts of Interest

The authors declare that there are no conflicts of interest.

Acknowledgments

The authors extend their appreciation to the Deanship of Scientific Research at King Khalid University, Saudi Arabia, for funding this work through research groups program under grant R.G.P.2/11/43.

References

[1] J. Stefan, "Versuchuber die scheinbare adhesion,Sitzunqsber Sachs kadwissein," *Math-Nat Wiss Kl*, vol. 69, pp. 713–721, 1874.
[2] T. Hayat, M. Nawaz, A. A. Hendi, and S. Asghar, "MHD squeezing flow of a micropolar fluid between parallel disks," *Journal of Fluids Engineering*, vol. 133, pp. 111206–111210, 2011.
[3] M. Mustafa, T. Hayat, and S. Obaidat, "On heat and mass transfer in the unsteady squeezing flow between parallel plates," *Meccanica*, vol. 47, no. 7, pp. 1581–1589, 2012.
[4] B. Mahanthesh, B. J. Gireesha, N. S. Shashikumar, T. Hayat, and A. Alsaedi, "Marangoni convection in Casson liquid flow due to an infinite disk with exponential space dependent heat source and cross-diffusion effects," *Results in Physics*, vol. 9, pp. 78–85, 2018.
[5] J. L. Neuringer, "Some viscous flows of a saturated ferrofluid under the combined influence of thermal and magnetic field gradients," *International Journal of Non-Linear Mechanics*, vol. 1, pp. 123–137, 1996.
[6] W. A. Khan, Z. H. Khan, and R. U. Haq, "Flow and heat transfer of ferrofluids over a flat plate with uniform heat flux," *The European Physical Journal Plus*, vol. 130, no. 4, Article ID 86, 2015.
[7] A. M. Rashad, "Impact of thermal radiation on MHD slip flow of a ferrofluid over a non-isothermal wedge," *Journal of Magnetism and Magnetic Materials*, vol. 422, pp. 25–31, 2017.
[8] A. Zaib, U. Khan, Z. Shah, P. Kumam, and P. Thounthong, "Optimization of entropy generation in flow of micropolar mixed convective magnetite (Fe3O4) ferroparticle over a vertical plate," *Alexandria Engineering Journal*, vol. 58, no. 4, pp. 1461–1470, 2019.
[9] L. Ali, X. Liu, B. Ali, S. Mujeed, S. Abdal, and S. A. Khan, "Analysis of magnetic properties of nano-particles due to a magnetic dipole in micropolar fluid flow over a stretching sheet," *Coatings*, vol. 10, no. 2, Article ID 170, 2020.
[10] S. Suresh, K. P. Venkitaraj, P. Selvakumar, and M. Chandrasekar, "Effect of Al_2O_3-Cu/water hybrid nanofluid in heat transfer," *Experimental Thermal and Fluid Science*, vol. 38, pp. 54–60, 2012.
[11] D. Madhesh and S. Kalaiselvam, "Experimental study on heat transfer and rheological characteristics of hybrid nanofluids for cooling applications," *Journal of Experimental Nanoscience*, vol. 10, no. 15, pp. 1194–1213, 2015.
[12] A. A. Minea, "Hybrid nanofluids based on Al_2O_3, TiO_2 and SiO_2: numerical evaluation of different approaches," *International Journal of Heat and Mass Transfer*, vol. 104, pp. 852–860, 2017.
[13] T. Hayat and S. Nadeem, "Heat transfer enhancement with Ag-CuO/water hybrid nanofluid," *Results in Physics*, vol. 7, pp. 2317–2324, 2017.
[14] F. Mebarek-Oudina, "Convective heat transfer of Titania nanofluids of different base fluids in cylindrical annulus with discrete heat source," *Heat Transfer-Asian Research*, vol. 48, no. 1, pp. 135–147, 2019.
[15] B. Mahanthesh, B. J. Gireesha, I. L. Animasaun, T. Muhammad, and N. S. Shashikumar, "MHD flow of SWCNT and MWCNT nanoliquids past a rotating stretchable disk with thermal and exponential space dependent heat source," *Physica Scripta*, vol. 94, no. 8, Article ID 85214, 2019.
[16] S. Marzougui, F. Mebarek-Oudina, A. Assia, M. Magherbi, Z. Shah, and K. Ramesh, "Entropy generation on magneto-convective flow of copper-water nanofluid in a cavity with chamfers," *Journal of Thermal Analysis and Calorimetry*, vol. 143, no. 3, pp. 2203–2214, 2020.
[17] A. Wakif, A. Chamkha, T. Thumma, I. L. Animasaun, and R. Sehaqui, "Thermal radiation and surface roughness effects on the thermo-magneto-hydrodynamic stability of alumina-copper oxide hybrid nanofluids utilizing the generalized Buongiorno's nanofluid model," *Journal of Thermal Analysis and Calorimetry*, vol. 143, no. 2, pp. 1201–1220, 2020.
[18] A. S. Alshomrani and T. Gul, "A convective study of Al_2O_3-H_2O and Cu-H_2O nano-liquid films sprayed over a stretching cylinder with viscous dissipation," *The European Physical Journal Plus*, vol. 132, no. 11, Article ID 495, 2017.
[19] N. Sandeep and A. Malvandi, "Enhanced heat transfer in liquid thin film flow of non-Newtonian nanofluids embedded with graphene nanoparticles," *Advanced Powder Technology*, vol. 27, no. 6, pp. 2448–2456, 2016.
[20] N. Sandeep, "Effect of aligned magnetic field on liquid thin film flow of magnetic-nanofluids embedded with graphene nanoparticles," *Advanced Powder Technology*, vol. 28, no. 3, pp. 865–875, 2017.
[21] A. Ahmed and S. Nadeem, "Effects of magnetohydrodynamics and hybrid nanoparticles on a micropolar fluid with 6-types of stenosis," *Results in Physics*, vol. 7, pp. 4130–4139, 2017.
[22] S. Hamrelaine, F. Mebarek-Oudina, and M. R. Sari, "Analysis of MHD Jeffery Hamel flow with suction/injection by homotopy analysis method," *Journal of Advanced Research in Fluid Mechanics and Thermal Sciences*, vol. 58, pp. 173–186, 2019.
[23] K. Anantha Kumar, N. Sandeep, V. Sugunamma, and I. L. Animasaun, "Effect of irregular heat source/sink on the radiative thin film flow of MHD hybrid ferrofluid," *Journal of Thermal Analysis and Calorimetry*, vol. 139, no. 3, pp. 2145–2153, 2020.
[24] A. Zaib, U. Khan, A. Wakif, and M. Zaydan, "Numerical entropic analysis of mixed MHD convective flows from a non-

isothermal vertical flat plate for radiative tangent hyperbolic blood biofluids conveying magnetite ferroparticles: dual similarity solutions," *Arabian Journal for Science and Engineering*, vol. 45, no. 7, pp. 5311–5330, 2020.

[25] A. Wakif, M. Qasim, M. I. Afridi, S. Saleem, and M. M. Al-Qarni, "Numerical examination of the entropic energy harvesting in a magnetohydrodynamic dissipative flow of Stokes' second problem: utilization of the gear-generalized differential quadrature method," *Journal of Non-equilibrium Thermodynamics*, vol. 44, no. 4, pp. 385–403, 2019.

[26] P. K. Kameswaran, S. Shaw, P. Sibanda, and P. V. S. N. Murthy, "Homogeneous-heterogeneous reactions in a nanofluid flow due to a porous stretching sheet," *International Journal of Heat and Mass Transfer*, vol. 57, no. 2, pp. 465–472, 2013.

[27] M. A. Chaudhary and J. H. Merkin, "Free-convection stagnation-point boundary layers driven by catalytic surface reactions: I the steady states," *Journal of Engineering Mathematics*, vol. 28, no. 2, pp. 145–171, 1994.

[28] R. Jawad and M. R. Azizah, "Numerical investigation of copper-water (Cu-water) nanofluid with different shapes of nanoparticles in a channel with stretching wall: slip effects," *Mathematical and Computational Applications*, vol. 21, pp. 43–58, 2016.

[29] J. H. Merkin, "A model for isothermal homogeneous-heterogeneous reactions in boundary-layer flow," *Mathematical and Computer Modelling*, vol. 24, no. 8, pp. 125–136, 1996.

[30] M. Sheikholeslami, M. M. Rashidi, D. M. Al Saad, F. Firouzi, B. RokiniH, and G. Domairrry, "Steady nanofluid flow between parallel plates considering thermophoresis and Brownian effects," *Journal of King Saud University Science*, vol. 49, 2015.

Hindawi
Advances in Mathematical Physics
Volume 2022, Article ID 1243018, 13 pages
https://doi.org/10.1155/2022/1243018

Research Article

A New Bivariate Extended Generalized Inverted Kumaraswamy Weibull Distribution

Mahmoud Ragab [1,2,3] **and Ahmed Elhassanein** [4,5]

[1]*Information Technology Department, Faculty of Computing and Information Technology, King Abdulaziz University, Jeddah 21589, Saudi Arabia*
[2]*Mathematics Department, Faculty of Science, Al-Azhar University, Naser City, 11884 Cairo, Egypt*
[3]*Centre of Artificial Intelligence for Precision Medicines, King Abdulaziz University, Jeddah 21589, Saudi Arabia*
[4]*Department of Mathematics, College of Science, University of Bisha, Bisha, Saudi Arabia*
[5]*Department of Mathematics, Faculty of Science, Damanhour University, Damanhour, Egypt*

Correspondence should be addressed to Mahmoud Ragab; mragab@kau.edu.sa

Received 5 September 2021; Revised 1 November 2021; Accepted 25 November 2021; Published 27 January 2022

Academic Editor: David Carf

This article presents a new bivariate extended generalized inverted Kumaraswamy Weibull (BIEGIKw-Weibull) distribution with nine parameters. Statistical properties of the new distribution are discussed. Forms of copulas, moments, conditional moments, bivariate reliability function, and bivariate hazard rate function are derived. Maximum likelihood estimators are formulated. Simulation is conducted for three different sets of parameters to verify the theoretical results and to discuss the new distribution properties. The performance of the maximum likelihood method is investigated via Monte Carlo simulation depending on the bias and the standard error. Simulated lifetime data is used as an application of the new model.

1. Introduction

The inverse Weibull (IW) distribution is widely used because of its applicability in various fields, like medicine, statistics, engineering, physics, and fluid mechanics [1–11]. To enhance such distributions, researchers introduced new generators by supplementing shape parameters to the base line distribution. The inverted Kumaraswamy (IK) with two shape parameters has been derived by Abd AL-Fattah et al. [12]. To accommodate both monotonic and nonmonotonic failure rates, the IK distribution has been generalized to involve three shape parameters (GIKum) by Iqbal et al. [13]. A new version with five parameters (GIKw-W) has been introduced by Jamal et al. [14]. Although the univariate continuous models suit many types of data sets, they cannot be used to model dependent sets of data; therefore, a lot of efforts have been done to develop bivariate distributions. Muhammed [15] proposed a bivariate generalized Kumaraswamy distribution. A bivariate inverse Weibull distribution has been developed by Mondal and Kundu [16]. Darwish and Shahbaz [17] formulated a bivariate transmuted Burr distribution; see also [18–25]. Most of the developed bivariate distributions have different shapes for the joint pdf and have singular part. In some cases, their joint probability distribution function can be expressed in compact forms. The maximum likelihood estimators cannot be expressed in explicit forms in most of the cases. Ganji et al. [26] generalized the method introduced by Alzaatreh et al. [27] to generate bivariate distributions with marginals having $T-X$ families. Let $g_{X,Y}(x,y)$ be the pdf of the bivariate random variable (X,Y), with $x \in a_1, b_1]$, $y \in a_2, b_2]$, $-\infty < a_1 < b_1 < \infty$,$-\infty < a_2 < b_2 < \infty$. Consider $F_1(G_U(u))$ and $F_2(G_V(v))$ be functions of the cdfs of a random variables U and V, respectively, such that

(1) $F_1(G_U(u)) \in [a_1, b_1]$ and $F_2(G_V(v)) \in [a_2, b_2]$

(2) $F_1(G_U(u))$ and $F_2(G_V(v))$ are differentiable and monotonically nondecreasing functions

(3) $F_1(G_U(u)) \longrightarrow a_1$ as $u \longrightarrow -\infty$, $F_1(G_U(u)) \longrightarrow b_1$ as $u \longrightarrow \infty$, $F_2(G_V(v)) \longrightarrow a_2$ as $v \longrightarrow -\infty$, and $F_2(G_V(v)) \longrightarrow b_2$ as $v \longrightarrow \infty$

The cdf of the random variable (U, V) is given by

$$F_{U,V}(F_1(G_X(u)), F_2(G_Y(z))) = \int_{c_1}^{F_1(G_X(u))} \int_{c_2}^{F_2(G_Y(v))} g_{X,Y}(x,y)dxdy. \tag{1}$$

In this paper, we introduce a new bivariate extended generalized inverted Kumaraswamy Weibull (BIEGIKw-Weibull) distribution; its joint pdf is absolutely continuous, takes only one form with no singular parts, and offers different shapes for different values of parameters, and its hazard function shows different shapes. Almost all statistical quantities of the new distribution can be obtained in closed forms including the maximum likelihood estimators. The new model is developed using the new six parameter distribution that is more flexible with so favorable properties [28]. Theoretical properties of the proposed distribution including marginal distributions, copulas, moments, conditional moments, bivariate reliability function, and bivariate hazard function are computed. Theoretical properties are investigated via simulation. Monte Carlo simulation is used to discuss the goodness of fit and the availability of the maximum likelihood method. A real data application is presented that proves the applicability of the new distribution. The paper is organized as follows. The new distribution is formulated in Section 2. In Section 3, closed forms of moments are derived. Reliability and hazard function are computed in Section 4. Estimation is performed in Section 5. Simulation for different three sets of parameters is performed in Section 6. A real data application is discussed in Section 7. Conclusion is given in Section 8.

2. Model Description

A one-dimensional random variable Z is said to have a GIKw-Weibull distribution if its cumulative distribution function (cdf) is given by

$$F(z) = \left(1 - \left\{1 + \left(\left[1 - e^{-\delta z^{\varphi}}\right]^{-\lambda} - 1\right)^{-\gamma}\right\}^{-\alpha}\right)^{\beta}, \tag{2}$$

where $z > 0$, α, β, $\gamma, \delta, \lambda, \varphi > 0$ are shape parameters [29]. Using (2) as a baseline distribution and $g_{X,Y}(x,y) = 1 + \delta_1 (1-x) + \delta_2(1-y) + 2\delta_3(1-x-y)$ in (1), where $x, y \in 0, 1]$, $\delta_1, \delta_2, \delta_3 \in -1, 1]$, $-1 \le \delta_1 + \delta_3 \le 1$, and $-1 \le \delta_2 + \delta_3 \le 1$, we formulate the following definition.

Definition 1. A bivariate random variable (U, V) is said to be a BIEGIKw-Weibull random variable if its cumulative probability function (cdf) and probability density function (pdf) are given by

$$\begin{aligned} F_{U,V}(u,v) = {} & \left(1 - \left\{1 + \left(\left[1 - e^{-\delta u^{\varphi}}\right]^{-\lambda} - 1\right)^{-\gamma}\right\}^{-\alpha}\right)^{\beta} \\ & \times \left(1 - \left\{1 + \left(\left[1 - e^{-\delta v^{\varphi}}\right]^{-\lambda} - 1\right)^{-\gamma}\right\}^{-\alpha}\right)^{\beta} \\ & \cdot \left\{1 + (\delta_1 + \delta_3) \times \left(1 - \left(1 - \left\{1 + \left(\left[1 - e^{-\delta u^{\varphi}}\right]^{-\lambda} - 1\right)^{-\gamma}\right\}^{-\alpha}\right)^{\beta}\right)\right. \\ & \left. + (\delta_2 + \delta_3) \times \left(1 - \left(1 - \left\{1 + \left(\left[1 - e^{-\delta v^{\varphi}}\right]^{-\lambda} - 1\right)^{-\gamma}\right\}^{-\alpha}\right)^{\beta}\right)\right\}, \end{aligned} \tag{3}$$

$$\begin{aligned} f_{U,V}(u,v) = {} & (\alpha\beta\gamma\lambda\delta\varphi)^2 (uv)^{\varphi-1} e^{-\delta(u^{\varphi}+v^{\varphi})} \\ & \left(\left[1 - e^{-\delta u^{\varphi}}\right]\left[1 - e^{-\delta v^{\varphi}}\right]\right)^{-(\lambda+1)} \times \\ & \left\{\left(\left[1 - e^{-\delta u^{\varphi}}\right]^{-\lambda} - 1\right)\left(\left[1 - e^{-\delta v^{\varphi}}\right]^{-\lambda} - 1\right)\right\}^{-(\gamma+1)} \times \\ & \left\{\left(1 + \left(\left[1 - e^{-\delta u^{\varphi}}\right]^{-\lambda} - 1\right)^{-\gamma}\right)\left(1 + \left(\left[1 - e^{-\delta v^{\varphi}}\right]^{-\lambda} - 1\right)^{-\gamma}\right)\right\}^{-(\alpha+1)} \\ & \times \left\{\left(1 - \left\{1 + \left(\left[1 - e^{-\delta u^{\varphi}}\right]^{-\lambda} - 1\right)\right\}^{-\alpha}\right) \times \left(1 - \left\{1 + \left(\left[1 - e^{-\delta v^{\varphi}}\right]^{-\lambda}\right.\right.\right.\right. \\ & \left.\left.\left.\left. - 1\right)^{-\gamma}\right\}^{-\alpha}\right)\right\}^{\beta-1} \times \left\{1 + (\delta_1 + \delta_3)(1 - 2\right. \\ & \left.(1 - \left\{1 + \left(\left[1 - e^{-\delta u^{\varphi}}\right]^{-\lambda} - 1\right)^{-\gamma}\right\}^{-\alpha}\right)^{\beta}) + (\delta_2 + \delta_3)(1 - 2 \\ & \left.(1 - \left\{1 + \left(\left[1 - e^{-\delta v^{\varphi}}\right]^{-\lambda} - 1\right)^{-\gamma}\right\}^{-\alpha}\right)^{\beta})\right\}, \end{aligned} \tag{4}$$

where $u, v > 0$, $\alpha, \beta, \gamma, \delta > 0$, $\delta_1, \delta_2, \delta_3 \in -1, 1]$, $-1 \le \delta_1 + \delta_3 \le 1$, and $-1 \le \delta_2 + \delta_3 \le 1$.

3. Marginals and Moments

Lemma 2. *Let (U, V) be a BIEGIKw-Weibull random variable with cdf and pdf given in (3) and (4). Then, the marginals are*

$$F_U(u) = \left(1 - \left\{1 + \left(\left[1 - e^{-\delta u^{\varphi}}\right]^{-\lambda} - 1\right)^{-\gamma}\right\}^{-\alpha}\right)^{\beta} \times \left\{1 + (\delta_1 + \delta_3)\left(1 - \left(1 - \left\{1 + \left(\left[1 - e^{-\delta u^{\varphi}}\right]^{-\lambda} - 1\right)^{-\gamma}\right\}^{-\alpha}\right)^{\beta}\right)\right\}, \tag{5}$$

$$F_V(v) = \left(1 - \left\{1 + \left(\left[1 - e^{-\delta v^{\varphi}}\right]^{-\lambda} - 1\right)^{-\gamma}\right\}^{-\alpha}\right)^{\beta} \times \left\{1 + (\delta_2 + \delta_3)\left(1 - \left(1 - \left\{1 + \left(\left[1 - e^{-\delta v^{\varphi}}\right]^{-\lambda} - 1\right)^{-\gamma}\right\}^{-\alpha}\right)^{\beta}\right)\right\}, \tag{6}$$

$$\begin{aligned} f_U(u) = {} & \alpha\beta\gamma\lambda\delta\varphi u^{\varphi-1} e^{-\delta u^{\varphi}} \left[1 - e^{-\delta u^{\varphi}}\right]^{-(\lambda+1)} \left(\left[1 - e^{-\delta u^{\varphi}}\right]^{-\lambda} - 1\right)^{-(\gamma+1)} \\ & \times \left\{1 + \left(\left[1 - e^{-\delta u^{\varphi}}\right]^{-\lambda} - 1\right)^{-\gamma}\right\}^{-(\alpha+1)} \\ & \times \left(1 - \left\{1 + \left(\left[1 - e^{-\delta u^{\varphi}}\right]^{-\lambda} - 1\right)^{-\gamma}\right\}^{-\alpha}\right)^{\beta-1} \\ & \times \left\{1 + \delta_1 + \delta_3 - 2(\delta_1 + \delta_3)\left(1 - \left\{1 + \left(\left[1 - e^{-\delta u^{\varphi}}\right]^{-\lambda} - 1\right)^{-\gamma}\right\}^{-\alpha}\right)^{\beta}\right\}, \end{aligned} \tag{7}$$

$$f_V(v) = \alpha\beta\gamma\lambda\delta\varphi v^{\varphi-1}e^{-\delta v^{\varphi}}\left[1-e^{-\delta v^{\varphi}}\right]^{-(\lambda+1)}\left(\left[1-e^{-\delta v^{\varphi}}\right]^{-\lambda}-1\right)^{-(\gamma+1)} \times\left\{1+\left(\left[1-e^{-\delta v^{\varphi}}\right]^{-\lambda}-1\right)^{-\gamma}\right\}^{-(\alpha+1)} \times\left(1-\left\{1+\left(\left[1-e^{-\delta v^{\varphi}}\right]^{-\lambda}-1\right)^{-\gamma}\right\}^{-\alpha}\right)^{\beta-1} \times\left\{1+\delta_2+\delta_3-2(\delta_2+\delta_3)\left(1-\left\{1+\left(\left[1-e^{-\delta v^{\varphi}}\right]^{-\lambda}-1\right)^{-\gamma}\right\}^{-\alpha}\right)^{\beta}\right\}. \tag{8}$$

For $\delta_1 = \delta_2 = -\delta_3$, we get the baseline distribution EGIKw-Weibull.

Copula function is commonly used to investigate the dependence between two random variables.

Definition 3 (see [30]). Let (U, V) be a BIGIKw-Weibull random variable with cpf $F_{U,V}(u, v)$ and marginals $F_U(u)$ and $F_V(v)$, and then, its copula function can be defied as $F_{U,V}(u, v) \triangleq C(\upsilon, \phi)$, where $\upsilon = F_U(u)$, $\phi = F_V(v)$, and $\upsilon, \phi \in (0, 1)$and the copula density function is defined as $c(\upsilon, \phi) = \partial^2 C(\upsilon, \phi)/\partial\upsilon\partial\phi$.

Using chain rule, we obtain

$$f_{U,V}(u, v) = \frac{\partial^2 F(u, v)}{\partial u\partial v} = \frac{\partial^2 C(F_U(u), F_V(v))}{\partial u\partial v} = \frac{\partial^2 C(\upsilon, \phi)}{\partial\upsilon\partial\phi}\frac{\partial F_U(u)}{\partial u}\frac{\partial F_V(v)}{\partial v} \triangleq c(\upsilon, \phi)f_U(u)f_V(v). \tag{9}$$

Lemma 4. *Let (U, V) be a BIEGIKw-Weibull random variable with pdf and marginals given in (4), (7), and (8). Then, the copula density function is given by*

$$c(\upsilon, \phi) = \frac{1}{H(u, \delta_1)H(v, \delta_2)} \cdot\left\{1+(\delta_1+\delta_3)\times\left(1-2\left(1-\left\{1+\left(\left[1-e^{-\delta u^{\varphi}}\right]^{-\lambda}-1\right)^{-\gamma}\right\}^{-\alpha}\right)^{\beta}\right) +(\delta_2+\delta_3)\left(1-2\left(1-\left\{1+\left(\left[1-e^{-\delta v^{\varphi}}\right]^{-\lambda}-1\right)^{-\gamma}\right\}^{-\alpha}\right)^{\beta}\right)\right\}. \tag{10}$$

Lemma 5. *Let (U, V) be a BIEGIKw-Weibull random variable with pdf and marginals given in (4), (7), and (8). Then, the conditional density functions are*

$$f_{\frac{U}{V}}(u/v) = \frac{\alpha\beta\gamma\lambda\delta\varphi u^{\varphi-1}e^{-\delta u^{\varphi}}\left[1-e^{-\delta u^{\varphi}}\right]^{-(\lambda+1)}}{H(v, \delta_2)} \times\left(1-\left[1-e^{-\delta u^{\varphi}}\right]^{\lambda}\right)^{-(\gamma+1)}\left\{1+\left(\left[1-e^{-\delta u^{\varphi}}\right]^{-\lambda}-1\right)^{-\gamma}\right\}^{-(\alpha+1)} \times\left(1-\left\{1+\left(\left[1-e^{-\delta u^{\varphi}}\right]^{-\lambda}-1\right)^{-\gamma}\right\}^{-\alpha}\right)^{\beta-1} \times\left\{1+(\delta_1+\delta_3)\left(1-2\left(1-\left\{1+\left(\left[1-e^{-\delta u^{\varphi}}\right]^{-\lambda}-1\right)^{-\gamma}\right\}^{-\alpha}\right)^{\beta}\right) +(\delta_2+\delta_3)\left(1-2\left(1-\left\{1+\left(\left[1-e^{-\delta v^{\varphi}}\right]^{-\lambda}-1\right)^{-\gamma}\right\}^{-\alpha}\right)^{\beta}\right)\right\}, \tag{11}$$

$$f_{\frac{V}{U}}(v/u) = \frac{\alpha\beta\gamma\lambda\delta\varphi v^{\varphi-1}e^{-\delta v^{\varphi}}\left[1-e^{-\delta v^{\varphi}}\right]^{-(\lambda+1)}}{H(u, \delta_1)}\left(1-\left[1-e^{-\delta v^{\varphi}}\right]^{\lambda}\right)^{-\gamma-1} \times\left\{1+\left(1-e^{-\delta v^{\varphi}}\right]^{-\lambda}-1\right)^{-\gamma}\right\}^{-\alpha-1} \times\left(1-\left\{1+\left(1-e^{-\delta v^{\varphi}}\right]^{-\lambda}-1\right)^{-\gamma}\right\}^{-\alpha}\right)^{\beta-1} \cdot\left\{1+(\delta_1+\delta_3)\left(1-2\left(1-\left\{1+\left(\left[1-e^{-\delta u^{\varphi}}\right]^{-\lambda}-1\right)^{-\gamma}\right\}^{-\alpha}\right)^{\beta}\right) +(\delta_2+\delta_3)\left(1-2\left(1-\left\{1+\left(\left[1-e^{-\delta v^{\varphi}}\right]^{-\lambda}-1\right)^{-\gamma}\right\}^{-\alpha}\right)^{\beta}\right)\right\}, \tag{12}$$

where

$$H(x, \delta) = 1+\delta+\delta_3 3.7-2(\delta+\delta_3) \cdot\left(1-2\left(1-\left\{1+\left(\left[1-e^{-\delta x^{\varphi}}\right]^{-\lambda}-1\right)^{-\gamma}\right\}^{-\alpha}\right)^{\beta}\right). \tag{13}$$

Lemma 6. *Let (U, V) be a BIEGIKw-Weibull random variable whose conditionals are given in (11) and (13). Then, the conditional moments are given by*

$$m^r_{\frac{U}{V}}(v) = E\left(\frac{U^r}{V}=v\right) = \frac{1}{H(v, \delta_2)}\left\{\frac{1}{\delta^{r/\varphi}}(1+\delta_1+\delta_2+2\delta_3 -2(\delta_2+\delta_3)(1-2\left(1-\left\{1+\left(\left[1-e^{-\delta v^{\varphi}}\right]^{-\lambda}-1\right)^{-\gamma}\right\}^{-\alpha}\right)^{\beta}\right) \times\sum_{i,j,k=0}^{\infty}\sum_{l=0}^{\lambda(\gamma j+k)-1}(-1)^l\xi_{i,j,k}\binom{\lambda(\gamma j+k)-1}{l}\frac{\Gamma((r/\varphi)+1)}{(l+1)^{(r/\varphi)+1}} -\frac{2(\delta_1+\delta_3)}{\delta^{r/\varphi}}\sum_{i,j,k=0}^{\infty}\sum_{l=0}^{2\lambda(\gamma j+k)-1}(-1)^l\xi_{i,j,k}\binom{\lambda(\gamma j+k)-1}{l}\times\frac{\Gamma((r/\varphi)+1)}{(l+1)^{(r/\varphi)+1}}\Bigg\},$$

$$m^r_{V/U}(u) = E\left(\frac{V^r}{U}=u\right) = \frac{1}{H(u, \delta_1)} \cdot\left\{\frac{1}{\delta^{r/\varphi}}(1+\delta_1+\delta_2+2\delta_3-2(\delta_2+\delta_3) \cdot\left(1-2\left(1-\left\{1+\left(\left[1-e^{-\delta u^{\varphi}}\right]^{-\lambda}-1\right)^{-\gamma}\right\}^{-\alpha}\right)^{\beta}\right)\right) \times\sum_{i,j,k=0}^{\infty}\sum_{l=0}^{\lambda(\gamma j+k)-1}(-1)^l\xi_{i,j,k}(\beta)\binom{\lambda(\gamma j+k)-1}{l}\frac{\Gamma((r/\varphi)+1)}{(l+1)^{(r/\varphi)+1}} -\frac{2(\delta_1+\delta_3)}{\delta^{r/\varphi}}\sum_{i,j,k=0}^{\infty}\sum_{l=0}^{\lambda(\gamma j+k)-1}(-1)^l\xi_{i,j,k}(2\beta) \cdot\binom{\lambda(\gamma j+k)-1}{l}\times\frac{\Gamma((r/\varphi)+1)}{(l+1)^{(r/\varphi)+1}}\Bigg\}, \tag{14}$$

where

$$\xi_{i,j,k}(\rho) = (-1)^{i+j}\lambda(\gamma j+k)\binom{\rho}{i}\binom{\alpha i+j-1}{j}\binom{\gamma j+k-1}{k}. \tag{15}$$

γ is a positive integer and H is given by (13); for more details, see [28].

Lemma 7. *Let (U, V) be a BIEGIKw-Weibull random variable whose density function is given in (4). Then, the joint moments are given by*

$$
\begin{aligned}
m_{r,s} = E(U^r V^s) = {} & \frac{(1+\delta_1+\delta_2+2\delta_3)}{\delta^{r/\varphi}\delta^{s/\varphi}} \\
& \times \left\{ \sum_{i,j,k=0}^{\infty} \sum_{l=0}^{\lambda(\gamma j+k)-1} (-1)^l \xi_{i,j,k}(\beta) \binom{\lambda(\gamma j+k)-1}{l} \frac{\Gamma((r/\varphi)+1)}{(l+1)^{(r/\varphi)+1}} \right. \\
& \left. \times \sum_{o,p,q=0}^{\infty} \sum_{t=0}^{\lambda(\gamma p+q)-1} (-1)^t \xi_{i,j,k}(\beta) \binom{\lambda(\gamma p+q)-1}{t} \frac{\Gamma((s/\varphi)+1)}{(t+1)^{(s/\varphi)+1}} \right] \\
& - \frac{2}{\delta^{r/\varphi}\delta^{s/\varphi}} \left[\sum_{i,j,k=0}^{\infty} \sum_{l=0}^{\lambda(\gamma j+k)-1} (-1)^l \xi_{i,j,k}(2\beta) \binom{2\lambda(\gamma j+k)-1}{l} \frac{\Gamma((r/\varphi)+1)}{(l+1)^{(r/\varphi)+1}} \right. \\
& \left. \times \sum_{o,p,q=0}^{\infty} \sum_{t=0}^{\lambda(\gamma p+q)-1} (-1)^t \xi_{o,p,q}(\beta) \binom{\lambda(\gamma p+q)-1}{t} \frac{\Gamma((s/\varphi)+1)}{(t+1)^{(s/\varphi)+1}} \right] \\
& - \frac{2(\delta_2+\delta_3)}{\delta^{r/\varphi}\delta^{s/\varphi}} \left[\sum_{i,j,k=0}^{\infty} \sum_{l=0}^{\lambda(\gamma j+k)-1} (-1)^l \xi_{i,j,k}(\beta) \binom{\lambda(\gamma j+k)-1}{l} \frac{\Gamma((r/\varphi)+1)}{(l+1)^{(r/\varphi)+1}} \right. \\
& \left. \times \sum_{o,p,q=0}^{\infty} \sum_{t=0}^{\lambda(\gamma j+q)-1} (-1)^t \xi_{o,p,q}(2\beta) \binom{2\lambda(\gamma p+q)-1}{t} \frac{\Gamma((s/\varphi)+1)}{(t+1)^{(s/\varphi)+1}} \right\},
\end{aligned}
\tag{16}
$$

where γ is a positive integer and $\xi_{i,j,k}(\rho)$ is given by Equation (15).

4. Reliability and Hazard Functions

Bivariate hazard function can be used to characterize bivariate distributions. It describes the failure characteristics of the individual variables and their joint failure behavior. Here, we compute the bivariate reliability function and the hazard function defined by Navarro [30].

Lemma 8. *Let (U, V) be a BIEGIKw-Weibull random variable whose cumulative and marginals are given in (3), (5), and (6), respectively. Then, its bivariate reliability function is given by*

$$R(u,v) = R_1(u,v) + R_2(u,v), \tag{17}$$

where

$$
\begin{aligned}
R_1(u,v) = {} & 1 - \left(1 - \left\{1 + \left(\left[1-e^{-\delta u^{\varphi}}\right]^{-\lambda} - 1\right)^{-\gamma}\right\}^{-\alpha}\right)^{\beta} \\
& \times \left(1 + (\delta_1+\delta_3)\left(1 - \left\{1 + \left(\left[1-e^{-\delta u^{\varphi}}\right]^{-\lambda} - 1\right)^{-\gamma}\right\}^{-\alpha}\right)^{\beta}\right) \\
& - \left(1 - \left\{1 + \left(\left[1-e^{-\delta v^{\varphi}}\right]^{-\lambda} - 1\right)^{-\gamma}\right\}^{-\alpha}\right)^{\beta} \\
& \times \left(1 + (\delta_2+\delta_3)\left(1 - \left\{1 + \left(\left[1-e^{-\delta v^{\varphi}}\right]^{-\lambda} - 1\right)^{-\gamma}\right\}^{-\alpha}\right)^{\beta}\right),
\end{aligned}
$$

$$
\begin{aligned}
R_2(u,v) = {} & (\alpha\beta\gamma\lambda\delta\varphi)^2 (uv)^{\varphi-1} e^{-\delta(u^{\varphi}+v^{\varphi})} \left(\left[1-e^{-\delta u^{\varphi}}\right]\left[1-e^{-\delta v^{\varphi}}\right]\right)^{-(\lambda+1)} \\
& \times \left(\left(\left[1-e^{-\delta u^{\varphi}}\right]^{-\lambda} - 1\right)\left(\left[1-e^{-\delta v^{\varphi}}\right]^{-\lambda} - 1\right)\right)^{-(\gamma+1)} \\
& \times \left\{\left(1 + \left(\left[1-e^{-\delta u^{\varphi}}\right]^{-\lambda} - 1\right)^{-\gamma}\right)\left(1 + \left(\left[1-e^{-\delta v^{\varphi}}\right]^{-\lambda} - 1\right)^{-\gamma}\right)\right\}^{-(\alpha+1)} \\
& \times \left\{\left(1 - \left\{1 + \left(\left[1-e^{-\delta u^{\varphi}}\right]^{-\lambda} - 1\right)^{-\gamma}\right\}^{-\alpha}\right)\right. \\
& \times \left.\left(1 - \left\{1 + \left(\left[1-e^{-\delta v^{\varphi}}\right]^{-\lambda} - 1\right)^{-\gamma}\right\}^{-\alpha}\right)\right\}^{\beta-1} \\
& \times \left\{1 + (\delta_1+\delta_3)\left(1 - 2\left(1 - \left\{1 + \left(\left[1-e^{-\delta u^{\varphi}}\right]^{-\lambda} - 1\right)^{-\gamma}\right\}^{-\alpha}\right)^{\beta}\right)\right. \\
& \left. + (\delta_2+\delta_3)\left(1 - 2\left(1 - \left\{1 + \left(\left[1-e^{-\delta v^{\varphi}}\right]^{-\lambda} - 1\right)^{-\gamma}\right\}^{-\alpha}\right)^{\beta}\right)\right\}.
\end{aligned}
\tag{18}
$$

Lemma 9. *Let (U, V) be a BIEGIKw-Weibull random variable whose density and reliability functions are given in (4) and (17). Then, its bivariate hazard rate function is given by*

$$
\begin{aligned}
h(u,v) = {} & \left\{(\alpha\beta\gamma\lambda\delta\varphi)^2 (uv)^{\varphi-1} e^{-\delta(u^{\varphi}+v^{\varphi})} \left(\left[1-e^{-\delta u^{\varphi}}\right]\left[1-e^{-\delta v^{\varphi}}\right]\right)^{-(\lambda+1)}\right. \\
& \times \left\{\left(\left[1-e^{-\delta u^{\varphi}}\right]^{-\lambda} - 1\right)\left(\left[1-e^{-\delta v^{\varphi}}\right]^{-\lambda} - 1\right)\right\}^{-(\gamma+1)} \\
& \times \left\{\left(1 + \left(\left[1-e^{-\delta u^{\varphi}}\right]^{-\lambda} - 1\right)^{-\gamma}\right)\left(1 + \left(\left[1-e^{-\delta v^{\varphi}}\right]^{-\lambda} - 1\right)^{-\gamma}\right)\right\}^{-(\alpha+1)} \\
& \times \left\{\left(1 - \left\{1 + \left(\left[1-e^{-\delta u^{\varphi}}\right]^{-\lambda} - 1\right)^{-\gamma}\right\}^{-\alpha}\right)\right. \\
& \times \left.\left(1 - \left\{1 + \left(\left[1-e^{-\delta v^{\varphi}}\right]^{-\lambda} - 1\right)^{-\gamma}\right\}^{-\alpha}\right)\right\}^{\beta-1} \\
& \times \left\{1 + (\delta_1+\delta_3)\left(1 - 2\left(1 - \left\{1 + \left(\left[1-e^{-\delta u^{\varphi}}\right]^{-\lambda} - 1\right)^{-\gamma}\right\}^{-\alpha}\right)^{\beta}\right)\right. \\
& \left.\left. + (\delta_2+\delta_3)\left(1 - 2\left(1 - \left\{1 + \left(\left[1-e^{-\delta v^{\varphi}}\right]^{-\lambda} - 1\right)^{-\gamma}\right\}^{-\alpha}\right)^{\beta}\right)\right\}\right. \\
& \cdot \left\{1 - \left(1 - \left\{1 + \left(\left[1-e^{-\delta u^{\varphi}}\right]^{-\lambda} - 1\right)^{-\gamma}\right\}^{-\alpha}\right)^{\beta}\right. \\
& \times \left(1 + (\delta_1+\delta_3)\left(1 - \left\{1 + \left(\left[1-e^{-\delta u^{\varphi}}\right]^{-\lambda} - 1\right)^{-\gamma}\right\}^{-\alpha}\right)^{\beta}\right) \\
& - \left(1 - \left\{1 + \left(\left[1-e^{-\delta v^{\varphi}}\right]^{-\lambda} - 1\right)^{-\gamma}\right\}^{-\alpha}\right)^{\beta} \\
& \times \left.\left(1 + (\delta_2+\delta_3)\left(1 - \left\{1 + \left(\left[1-e^{-\delta v^{\varphi}}\right]^{-\lambda} - 1\right)^{-\gamma}\right\}^{-\alpha}\right)^{\beta}\right)\right. \\
& + (\alpha\beta\gamma\lambda\delta\varphi)^2 (uv)^{\varphi-1} e^{-\delta(u^{\varphi}+v^{\varphi})} \left(\left[1-e^{-\delta u^{\varphi}}\right]\left[1-e^{-\delta v^{\varphi}}\right]\right)^{-(\lambda+1)} \\
& \times \left(\left(\left[1-e^{-\delta u^{\varphi}}\right]^{-\lambda} - 1\right)\left(\left[1-e^{-\delta v^{\varphi}}\right]^{-\lambda} - 1\right)\right)^{-(\gamma+1)} \\
& \times \left\{\left(1 + \left(\left[1-e^{-\delta u^{\varphi}}\right]^{-\lambda} - 1\right)^{-\gamma}\right)\left(1 + \left(\left[1-e^{-\delta v^{\varphi}}\right]^{-\lambda} - 1\right)^{-\gamma}\right)\right\}^{-(\alpha+1)} \\
& \times \left\{\left(1 - \left\{1 + \left(\left[1-e^{-\delta u^{\varphi}}\right]^{-\lambda} - 1\right)^{-\gamma}\right\}^{-\alpha}\right)\right. \\
& \times \left.\left(1 - \left\{1 + \left(\left[1-e^{-\delta v^{\varphi}}\right]^{-\lambda} - 1\right)^{-\gamma}\right\}^{-\alpha}\right)\right\}^{\beta-1} \\
& \times \left\{1 + (\delta_1+\delta_3)\left(1 - 2\left(1 - \left\{1 + \left(\left[1-e^{-\delta u^{\varphi}}\right]^{-\lambda} - 1\right)^{-\gamma}\right\}^{-\alpha}\right)^{\beta}\right)\right. \\
& \left.\left. + (\delta_2+\delta_3)\left(1 - 2\left(1 - \left\{1 + \left(\left[1-e^{-\delta v^{\varphi}}\right]^{-\lambda} - 1\right)^{-\gamma}\right\}^{-\alpha}\right)^{\beta}\right)\right\}\right\}^{-1}.
\end{aligned}
\tag{19}
$$

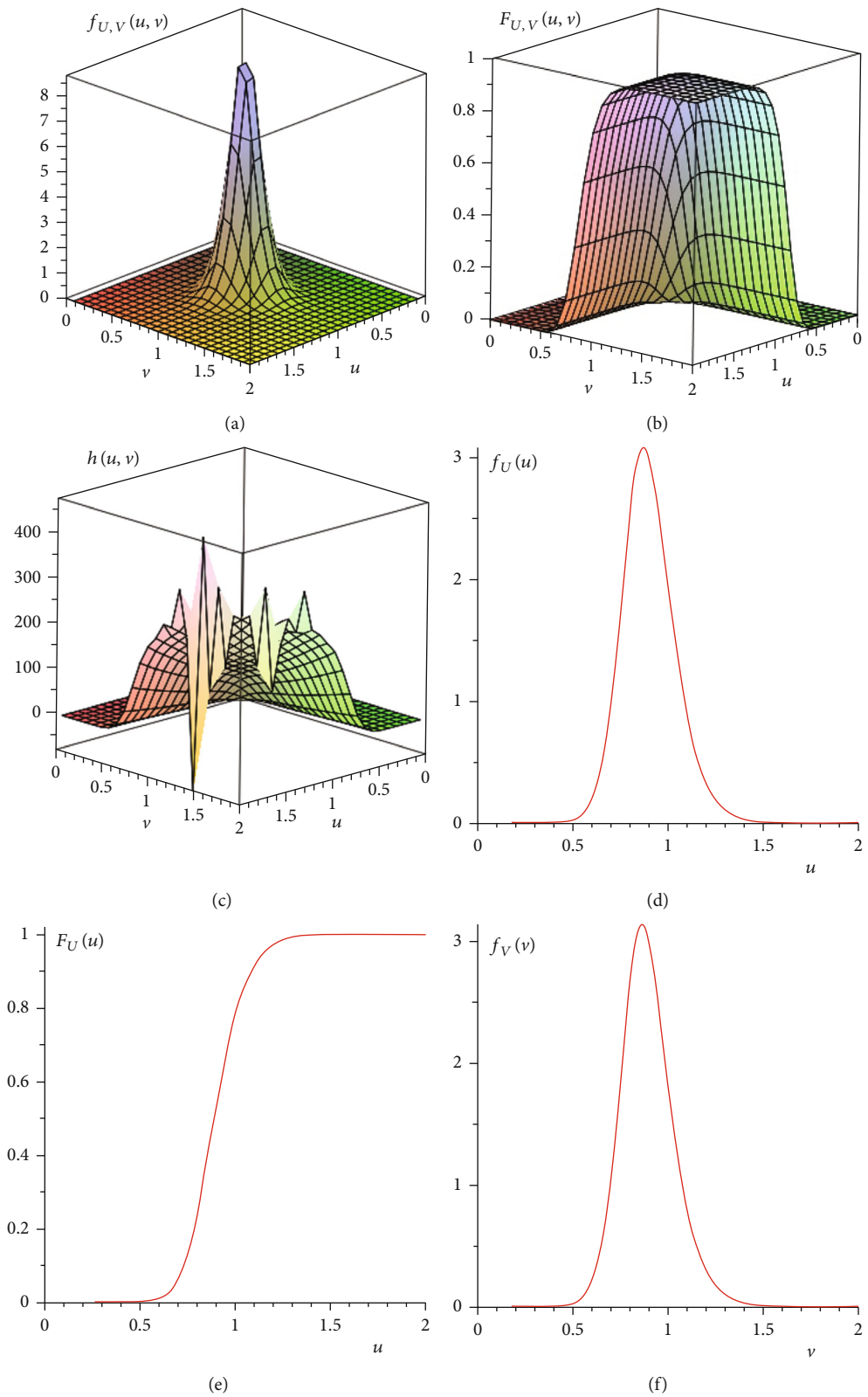

Figure 1: Continued.

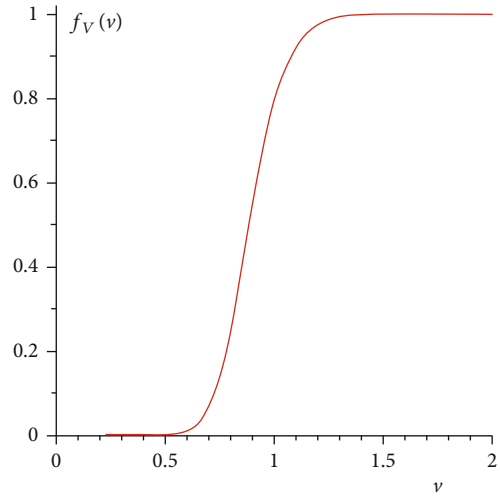

(g)

FIGURE 1: For the set of parameters $\alpha = 1$, $\beta = 1.8$, $\gamma = 2.0$, $\lambda = 1.5$, $\delta = 1.6$, $\delta_1 = -0.6$, $\delta_2 = -0.5$, $\delta_3 = 0.7$, and $\phi = 2.5$, the density function (4) is given in (a), the cumulative function (3) is given in (b), the hazard function (17) is given in (c), and the marginals (5), (7), (6), and (8) are given in (d–g), respectively.

5. Estimation

The maximum likelihood method is used to perform point estimators of the unknown parameters $\Theta = (\alpha, \beta, \gamma, \lambda, \varphi, \delta, \delta_1, \delta_2, \delta_3)'$. Let $(u_1, v_1), (u_2, v_2), \cdots, (u_n, v_n)$ be a random sample from the BIEGIKw-Weibull random variable. The maximum log-likelihood function is given by $L(\Theta) = L_1(\Theta) + L_2(\Theta)$, where

$$\begin{aligned} L_1(\Theta) = {} & 2n \ln(\alpha\beta\gamma\lambda\delta\varphi) + (\varphi - 1)\sum_{i=1}^{n} \ln u_i - \delta \sum_{i=1}^{n} u_i^{\varphi} - (\lambda + 1) \\ & \times \sum_{i=1}^{n} \ln\left[1 - e^{-\delta u_i^{\varphi}}\right]\Big) - (\gamma + 1)\sum_{i=1}^{n} \ln\left(\left[1 - e^{-\delta u_i^{\varphi}}\right]^{-\lambda} - 1\right) \\ & - (\alpha + 1) \times \sum_{i=1}^{n} \ln\left\{1 + \left(\left[1 - e^{-\delta u_i^{\varphi}}\right]^{-\lambda} - 1\right)^{-\gamma}\right\} \\ & + (\beta - 1) \times \sum_{i=1}^{n} \ln\left(1 - \left(\left\{1 + \left(\left[(1 - e^{-\delta u_i^{\varphi}}\right]^{-\lambda} - 1\right)^{-\gamma}\right)\right\}^{-\alpha}\right) +, \end{aligned}$$

$$\begin{aligned} L_2(\Theta) = {} & (\varphi - 1)\sum_{i=1}^{n} \ln v_i - \delta \sum_{i=1}^{n} v_i^{\varphi} - (\lambda + 1)\sum_{i=1}^{n} \ln\left[1 - e^{-\delta v_i^{\varphi}}\right] \\ & - (\gamma + 1) \times \sum_{i=1}^{n} \ln\left(\left[1 - e^{-\delta v_i^{\varphi}}\right]^{-\lambda} - 1\right) \\ & - (\alpha + 1)\sum_{i=1}^{n} \ln\left\{1 + \left(\left[1 - e^{-\delta v_i^{\varphi}}\right]^{-\lambda} - 1\right)^{-\gamma}\right\} \\ & + (\beta - 1)\sum_{i=1}^{n} \ln\left(1 - \left\{1 + \left(\left[1 - e^{-\delta v_i^{\varphi}}\right]^{-\lambda} - 1\right)^{-\gamma}\right\}^{-\alpha}\right) \\ & + \sum_{i=1}^{n} \ln\left\{1 + (\delta_1 + \delta_3)\left(1 - 2\left(1 - \left\{1 + \left(\left[1 - e^{-\delta u_i^{\varphi}}\right]^{-\lambda} - 1\right)^{-\gamma}\right\}^{-\alpha}\right)^{\beta}\right)\right. \\ & \left. + (\delta_2 + \delta_3)\left(1 - 2\left(1 - \left\{1 + \left(\left[1 - e^{-\delta v_i^{\varphi}}\right]^{-\lambda} - 1\right)^{-\gamma}\right\}^{-\alpha}\right)^{\beta}\right)\right\}. \end{aligned} \tag{20}$$

Consider the score vector $\Psi = (\Psi_\alpha, \Psi_\beta, \Psi_\gamma, \Psi_\lambda, \Psi_\varphi, \Psi_\delta, \Psi_{\delta_1}, \Psi_{\delta_2}, \Psi_{\delta_3})'$, where $\Psi_\alpha = \Psi_{\alpha 1} + \Psi_{\alpha 2}, \Psi_\beta = \Psi_{\beta 1} + \Psi_{\beta 2}, \Psi_\gamma = \Psi_{\gamma 1} + \Psi_{\gamma 2}, \Psi_\lambda = \Psi_{\lambda 1} + \Psi_{\lambda 2}, \Psi_\varphi = \Psi_{\varphi 1} + \Psi_{\varphi 2} + \Psi_{\varphi 3}, \Psi_\delta = \Psi_{\delta 1} + \Psi_{\delta 2}$; then,

The system of equations can be solved via symbolic mathematical packages.

6. Simulation

In this section, simulation is performed for three different sets of parameters to verify our theoretical results and to discuss the new bivariate distribution properties. For the first set of parameters, $\alpha = 1$, $\beta = 1.8$, $\gamma = 2.0$, $\lambda = 1.5$, $\delta = 1.6$, $\delta_1 = -0.6$, $\delta_2 = -0.5$, $\delta_3 = 0.7$, and $\phi = 2.5$. The symmetry, unimodality, and high beakness of the density function (4) can be observed in Figure 1(a). For (u, v) approximately greater than $(2, 2)$, the cumulative function (3) approaches 1 (Figure 1(b)). The bivariate hazard function increases with the increase of (u, v) as displayed in Figure 1(c). Symmetry of marginals and bell shape densities with beakness can be noted in Figures 1(d)–1(g). For the second set of parameters, $\alpha = 1.5$, $\beta = 1.0$, $\gamma = 0.7$, $\lambda = 2.0$, $\delta = 0.6$, $\delta_1 = 0.7$, $\delta_2 = 0.8$, $\delta_3 = -0.5$, and $\phi = 1.0$. The density function (4) is unimodal and has high beak (Figure 2(a)). For (u, v) approximately greater than $(10, 10)$, the cumulative function (3) approaches 1 (Figure 2(b)). The bivariate hazard function decreases with the increase of (u, v) (Figure 2(c)). Unimodality and right tail property can be observed for marginals (Figures 2(d)–2(g)). For the third set of parameters, $\alpha = 0.5$, $\beta = 0.7$, $\gamma = 0.9$, $\lambda = 0.6$, $\delta = 0.2$, $\delta_1 = 0.5$, $\delta_2 = 0.4$, $\delta_3 = 0.1$, and $\phi = 0.3$. The density function (4) deformed and becomes an open surface (Figure 3(a)). The cumulative function (3) approaches 1 as (u, v) approaches infinity (Figure 3(b)). The bivariate hazard function decreases with the increase of

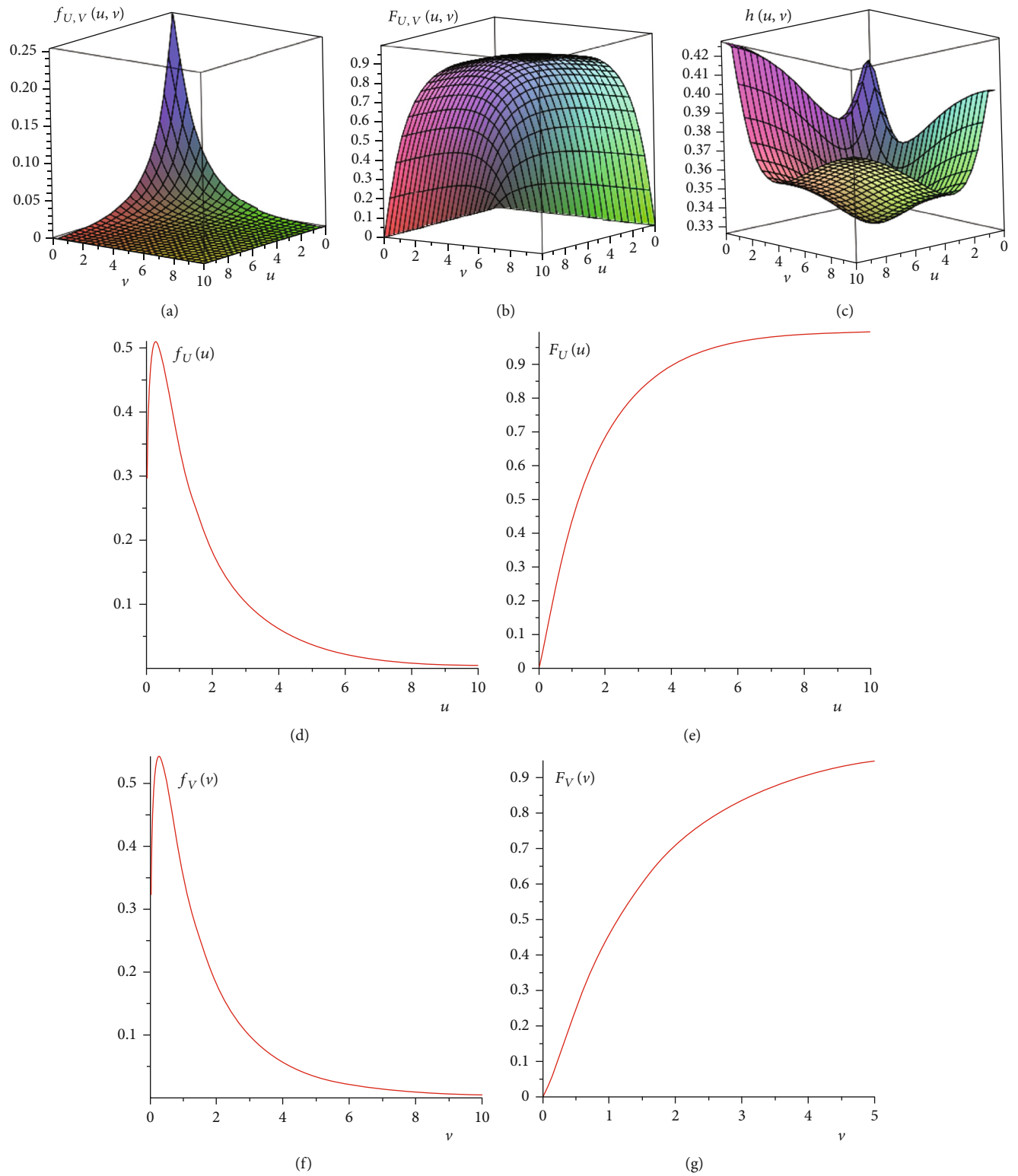

FIGURE 2: For the set of parameters $\alpha = 1.5$, $\beta = 1.0$, $\gamma = 0.7$, $\lambda = 2.0$, $\delta = 0.6$, $\delta_1 = 0.7$, $\delta_2 = 0.8$, $\delta_3 = -0.5$, and $\phi = 1.0$, the density function (4) is given in (a), the cumulative function (3) is given in (b), the hazard function (17) is given in (c), and the marginals (5), (7), (6), and (8) are given in (d–g), respectively.

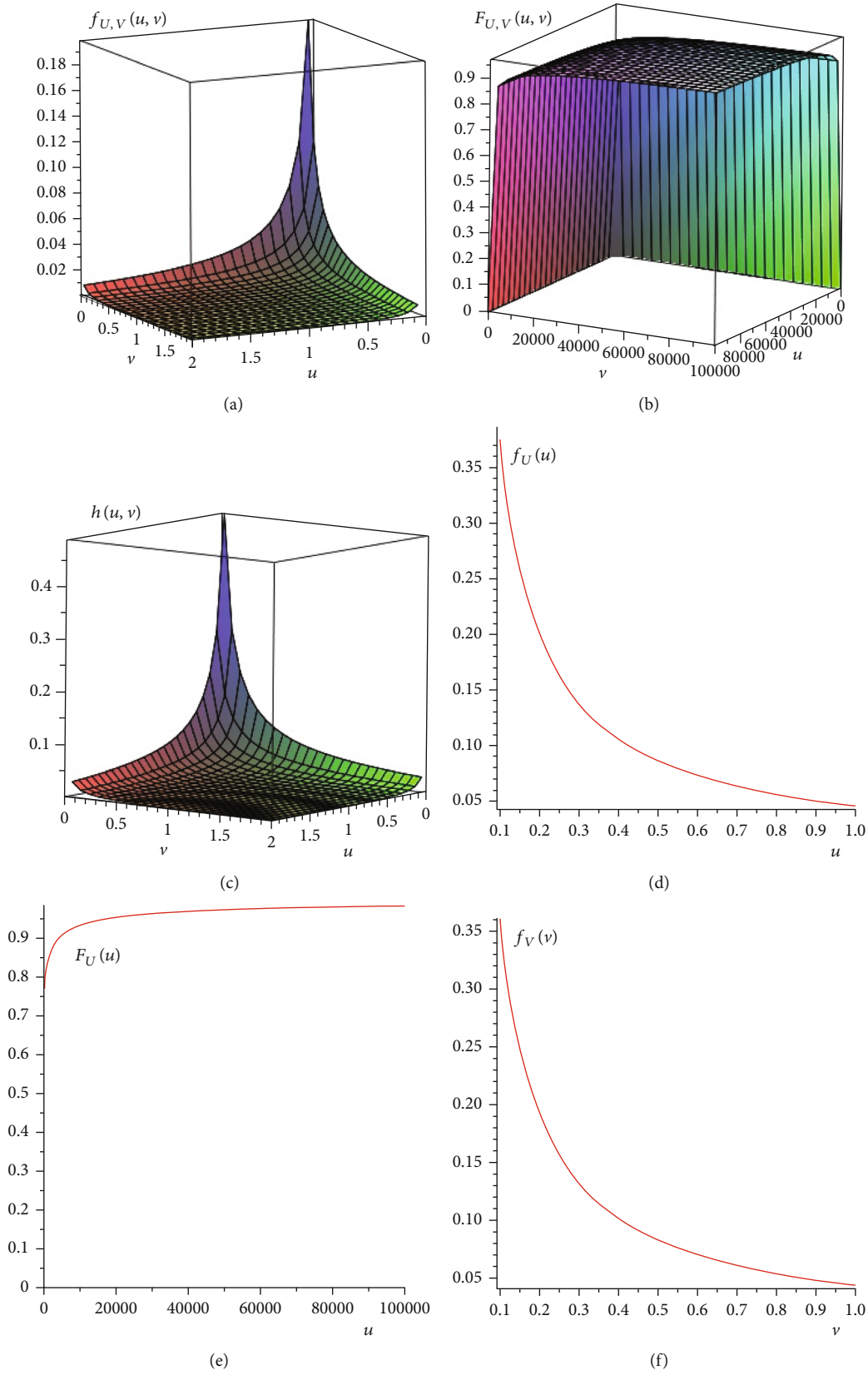

Figure 3: Continued.

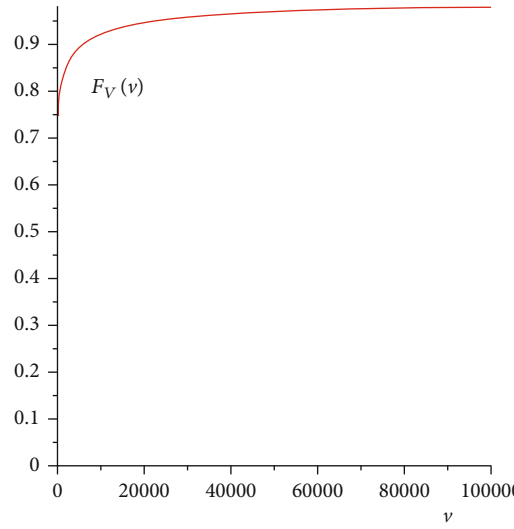

(g)

Figure 3: For the set of parameters $\alpha = 0.5$, $\beta = 0.7$, $\gamma = 0.9$, $\lambda = 0.6$, $\delta = 0.2$, $\delta_1 = 0.5$, $\delta_2 = 0.4$, $\delta_3 = 0.1$, and $\phi = 0.3$, the density function (4) is given in (a), the cumulative function (3) is given in (b), the hazard function (17) is given in (c), and the marginals (5), (7), (6), and (8) are given in (d–g), respectively.

Table 1: Average maximum likelihood estimates for the first set of observations.

Sample size	Parameter	Average estimate	Bias	SE
$n = 20$	α	0.3420	-0.158	0.0279
	β	2.510	-0.49	0.134
	γ	0.535	0.035	0.102
	λ	0.573	0.073	0.118
	δ	1.216	-0.284	0.143
	φ	2.902	-0.098	0.103
$n = 50$	α	0.4829	-0.017	0.0914
	β	4.508	1.508	0.667
	γ	0.5422	0.042	0.0986
	λ	0.4006	-0.099	0.0773
	δ	0.858	-0.642	0.153
	φ	2.801	-0.199	0.177
$n = 100$	α	0.2661	-0.244	0.0203
	β	3.206	0.206	0.243
	γ	0.9153	0.4153	0.0441
	λ	0.4187	-0.0813	0.0748
	δ	0.3047	-0.1953	0.0325
	φ	3.1596	0.1596	0.0850

Table 2: Average maximum likelihood estimates for the second set of observations.

Sample size	Parameter	Average estimate	Bias	SE
$n = 20$	α	1.463	-0.237	0.185
	β	1.98	0.18	1.40
	γ	0.96	-0.04	1.24
	λ	1.148	0.052	0.366
	δ	1.991	0.391	0.561
	φ	0.883	0.183	0.240
$n = 50$	α	1.405	-0.259	0.104
	β	2.424	0.624	0.956
	γ	1.39	0.39	1.21
	λ	1.497	0.297	0.579
	δ	1.941	0.341	0.378
	φ	0.714	-0.014	0.310
$n = 100$	α	1.448	-0.251	0.0804
	β	1.363	-0.437	0.332
	γ	1.08	0.08	1.76
	λ	1.403	0.203	0.309
	δ	1.323	-0.123	0.422
	φ	0.63	-0.07	0.276

(u, v) (Figure 3(c)). Marginals are given in Figures 3(d)–3(g). Monte Carlo simulation is used to generate samples for different sizes to discuss the performance of the new distribution. The first set of observations is generated for the parameters $\alpha = 0.5$, $\beta = 3$, $\gamma = 0.5$, $\lambda = 0.6$, $\delta = 1.5$, $\delta_1 = -0.7$, $\delta_2 = -0.6$, $\delta_3 = 0.9$, and $\phi = 3$; the second set is generated for the parameters $\alpha = 1.7$, $\beta = 1.8$, $\gamma = 1.0$, $\lambda = 1.2$, $\delta = 1.6$, $\delta_1 = -0.6$, $\delta_2 = -0.5$, $\delta_3 = 0.8$, and $\phi = 0.7$. Considering δ_1, δ_2, and δ_3 as

Table 3: Simulated computer series system of two components.

Sys	Processor lifetime	Memory lifetime	Sys	Processor lifetime	Memory lifetime	Sys	Processor lifetime	Memory lifetime	Sys	Processor lifetime	Memory lifetime	Sys	Processor lifetime	Memory lifetime
1	1.9292	3.9291	11	1.9386	4.0043	21	1.1739	3.3857	31	0.1181	0.0884	41	0.6270	1.7289
2	3.6621	0.0026	12	2.1000	2.0513	22	1.3482	1.9705	32	5.0533	2.3238	42	0.7947	0.7947
3	3.9608	0.8323	13	0.9867	0.9867	23	3.0935	3.0935	33	1.6465	2.0197	43	0.5079	5.3535
4	2.3504	3.3364	14	0.1837	0.1837	24	2.1396	2.1548	34	0.9096	0.6214	44	2.5913	2.5913
5	1.0833	3.3059	15	1.3989	4.1268	25	1.3288	0.9689	35	1.7494	2.3643	45	2.5372	2.4923
6	2.8414	1.8438	16	2.3757	2.7953	26	0.1115	0.1115	36	0.1058	0.1058	46	1.1917	0.0801
7	0.3309	0.3309	17	3.5202	1.4095	27	0.8503	2.8578	37	0.4593	0.4593	47	1.5254	4.4088
8	2.9884	1.5961	18	2.3364	0.1624	28	0.1955	0.1955	38	0.9938	1.7689	48	1.0986	1.0986
9	0.5784	1.8795	19	0.8584	1.9556	29	0.4614	0.8584	39	5.7561	0.3212	49	1.0051	1.0051
10	0.5520	0.5520	20	4.3435	1.0001	30	3.3887	1.9796	40	6.2950	1.0495	50	1.3640	1.3640

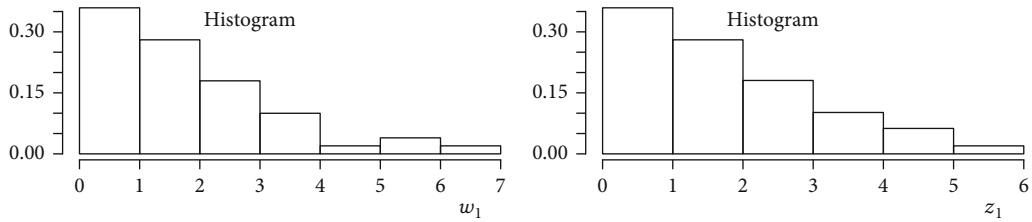

Figure 4: Histogram of the data in Table 3.

Table 4: The average maximum likelihood estimates of the BIEGIKw-Weibull parameters for the data in Table 3.

Parameter	Estimate	AIC	BIC
α	0.82096924		
β	0.38096869		
γ	1.03547483		
λ	1.25168661		
δ	0.23330064	325.4836	342.6918
ϕ	1.65658910		
δ_1	-0.36575551		
δ_2	0.86741494		
δ_3	-0.05319925		

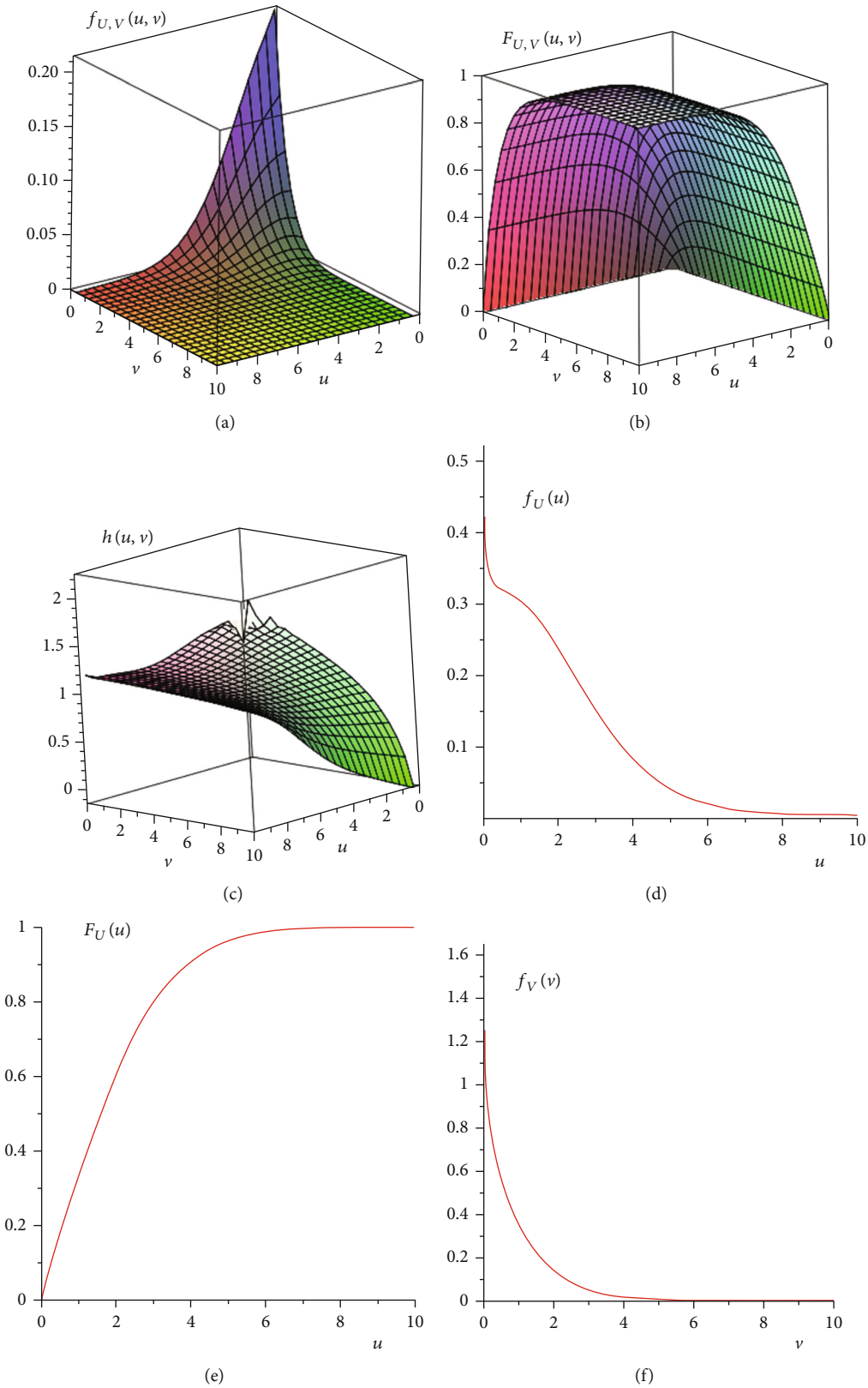

Figure 5: Continued.

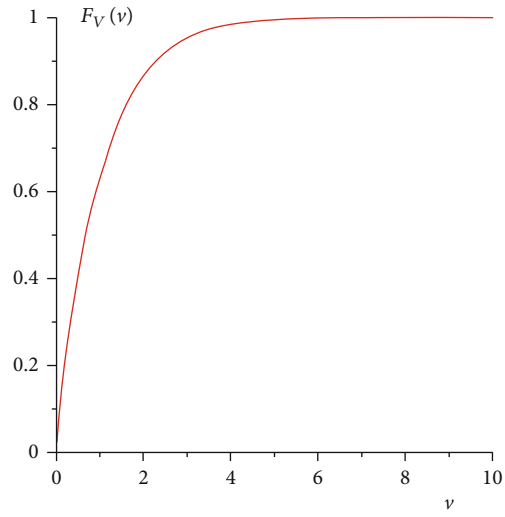

FIGURE 5: (a) The joint density function, (b) the cumulative function, (c) the hazard function, and (d–g) the marginals for the estimated parameters in Table 4.

chosen parameters, the maximum likelihood method is used to estimate the rest parameters; results are given in Tables 1 and 2. Depending on the bias and standard error, the maximum likelihood method shows well performance.

7. Real Data Application

In this section, the data discussed by [31] is used to investigate the applicability of the new distribution. Let $(u_1, v_1), (u_2, v_2), \cdots, (u_{50}, v_{50})$ be observed values of a BIEGIKw-Weibull random variable (U, V) with parameters $(\alpha, \beta, \gamma, \lambda, \delta, \phi, \delta_1, \delta_2, \delta_3)$, where U is the processor lifetime and V is the memory lifetime; see Table 3 and Figure 4. The maximum likelihood method is conducted to estimate the parameters with AIC and BIC; see Table 4. The joint density function, hazard function, and marginals for the estimated parameters are given in Figure 5.

8. Conclusions

Analysis of correlated data is one of the most important problems in statistics and data science. Here, we introduced a new bivariate distribution named BIEGIKw-Weibull. The proposed model is with nine parameters. It is a flexible one. Theoretical properties including density function, cumulative function, marginals, copula function, conditional distributions, and conditional moments have been derived explicitly. The new model exhibits very rich characteristics that differ according to the parameters. That supports the applicability of the model for a large set of correlated data with various properties. Simulation clearly verified the theoretical properties and the richness of its preferable characteristics. For different values of the parameters, the distribution has extremely different properties that are clear from Figures 1–3. For a set of values, we can observe symmetry and close surface for density function side by side with unimodality (Figure 1). All these properties deformed for another set of parameters (Figure 3). The bivariate hazard function exhibited different shapes. Monte Carlo simulation and real data application prove the applicability of the new distribution and the availability of the maximum likelihood method.

Data Availability

The data used are included within the article.

Conflicts of Interest

The authors declare that there are no conflicts of interest regarding the publication of this article.

Acknowledgments

This project was funded by the Deanship of Scientific Research (DSR) at King Abdulaziz University (KAU), Jeddah, Saudi Arabia, under grant no. G: 80-351-1442. The authors therefore acknowledge with thanks DSR for the technical and financial support.

References

[1] A. Z. Keller and A. R. R. Kamath, "Alternative reliability models for mechanical systems," in *Third International Conference in Reliability and Maintainability*, Toulse, France, 1982.

[2] W. B. Nelson, *Applied Life Data Analysis*, Wiley, New Yourk, 1982.

[3] R. M. Pakungwati, Y. Widyaningsih, and D. Lestari, "Marshall-Olkin extended inverse Weibull distribution and its application," *Journal of physics: conference series*, vol. 1108, no. 1, article 012114, 2018.

[4] D. A. Ramadan and W. A. Magdy, "On the alpha-power inverse Weibull distribution," *International Journal of Computer Applications*, vol. 181, no. 11, pp. 6–12, 2018.

[5] M. Q. Shahbaz, S. Shahbaz, and N. S. Butt, "The Kumaraswamy–inverse Weibull distribution," *Pakistan Journal of Statistics and Operation Research*, vol. 8, no. 3, pp. 479–489, 2012.

[6] G. Aryal and I. Elbatal, "Kumaraswamy modified inverse Weibull distribution: theory and application," *Applied Mathematics & Information Sciences*, vol. 9, no. 2, p. 651, 2015.

[7] M. A. Aldahlan, "The inverse Weibull inverse exponential distribution with application," *International Journal of Contemporary Mathematical Sciences*, vol. 14, no. 1, pp. 17–30, 2019.

[8] A. Aljouharah, "Estimating the parameters of an exponentiated inverted Weibull distribution under type-II censoring," *Applied Mathematical Sciences*, vol. 7, no. 35, pp. 1721–1736, 2013.

[9] A. S. Hassan and S. G. Nassr, "The inverse Weibull generator of distributions, properties and applications," *Journal of Data Science*, vol. 16, no. 4, pp. 723–742, 2018.

[10] S. A. Hassan, M. E. Almetwally, and M. G. Ibrahim, "Kumaraswamy inverted Topp-Leone distribution with applications to COVID-19 data," *Computers, Materials & Continua*, vol. 68, no. 1, pp. 337–358, 2021.

[11] F. R. S. de Gusmão, E. M. Ortega, and G. M. Cordeiro, "The generalized inverse Weibull distribution," *Statistical Papers*, vol. 52, no. 3, pp. 591–619, 2011.

[12] A. A. L.-F. AM, A. A. El-Helbawy, and G. R. Al-Dayian, "Inverted Kumaraswamy distribution: properties and estimation," *Pakistan Journal of Statistics*, vol. 33, no. 1, pp. 37–67, 2017.

[13] Z. Iqbal, M. M. Tahir, N. Riaz, S. A. Ali, and M. Ahmad, "Generalized inverted Kumaraswamy distribution, properties and application," *Open Journal of Statistics*, vol. 7, no. 4, pp. 645–662, 2017.

[14] F. Jamal, M. Arslan Nasir, G. Ozel, M. Elgarhy, and N. Mamode Khan, "Generalized inverted Kumaraswamy generated family of distributions: theory and applications," *Journal of Applied Statistics*, vol. 46, no. 16, pp. 2927–2944, 2019.

[15] H. Z. Muhammed, "On a bivariate generalized inverted Kumaraswamy distribution," *Physica A: Statistical Mechanics and its Applications*, vol. 553, article 124281, 2020.

[16] S. Mondal and D. Kundu, "A bivariate inverse Weibull distribution and its applications in complementary risks models," *Journal of Applied Statistics*, vol. 47, no. 6, pp. 1084–1108, 2021.

[17] J. A. Darwish and M. Q. Shahbaz, "Bivariate transmuted Burr distribution: properties and applcations," *Pakistan Journal of Statistics & Operation Research*, vol. 17, no. 1, pp. 15–24, 2021.

[18] A. Sarhan and N. Balakrishnan, "A new class of bivariate distributions and its mixture," *Journal of Multivariate Analysis*, vol. 98, no. 7, pp. 1508–1527, 2007.

[19] D. Kundu and R. D. Gupta, "Bivariate generalized exponential distribution," *Journal of Multivariate Analysis*, vol. 100, pp. 581–593, 2009.

[20] D. Kundu and R. D. Gupta, "A class of bivariate models with proportional reversed hazard marginals," *Sankhya B*, vol. 72, pp. 236–253, 2010.

[21] A. Sarhan, D. C. Hamilton, B. Smith, and D. Kundu, "The bivariate generalized linear failure rate distribution and its multivariate extension," *Computational Statistics and Data Analysis*, vol. 55, no. 1, pp. 644–654, 2011.

[22] H. Z. Muhammed, "Bivariate inverse Weibull distribution," *Journal of Statistical Computation and Simulation*, vol. 86, no. 12, pp. 2335–2345, 2016.

[23] H. Z. Muhammed, "Bivariate Dagum distribution," *International Journal of Reliability and Applications*, vol. 18, no. 2, pp. 65–82, 2017.

[24] M. S. Eliwa and M. El-Morshedy, "Bivariate discrete inverse Weibull distribution," 2018, https://arxiv.org/abs/1808.07748.

[25] H. Z. Muhammed, "Bivariate generalized Burr and related distributions: properties and estimation," *Journal of Data Science*, vol. 17, no. 3, pp. 532–548, 2019.

[26] M. Ganji, H. Bevraninand, and H. Golzar, "A new method for generating a continuous bivariate distribution families," *Journal of The Iranian Statistical Society*, vol. 17, no. 1, pp. 109–129, 2018.

[27] A. Alzaatreh, C. Lee, and F. Famoye, "A new method for generating families of continuous distributions," *Metron*, vol. 71, pp. 63–79, 2013.

[28] Q. Ramzan, M. Amin, A. Elhassanein, and M. Ikram, "The extended generalized inverted Kumaraswamy Weibull distribution: properties and applications," *AIMS Mathematics*, vol. 6, no. 9, pp. 9955–9980, 2021.

[29] T. S. Durrani and X. Zeng, "Copulas for bivariate probability distributions," *Electronics Letters*, vol. 43, no. 4, 2007.

[30] J. Navarro, "Characterizations using the bivariate failure rate function," *Statistics and Probability Letters*, vol. 78, no. 12, p. 1349, 2010.

[31] R. P. Oliveira, J. A. Achcar, J. Mazucheli, and W. Bertoli, "A new class of bivariate Lindley distributions based on stress and shock models and some of their reliability properties," *Reliability Engineering and System Safety*, vol. 211, article 107528, 2021.

Hindawi
Advances in Mathematical Physics
Volume 2021, Article ID 6229706, 9 pages
https://doi.org/10.1155/2021/6229706

Research Article

Unsteady Electrohydrodynamic Stagnation Point Flow of Hybrid Nanofluid Past a Convective Heated Stretch/Shrink Sheet

Muhammad Jawad,[1] Rashid Jan,[1] Salah Boulaaras,[2,3] Ibni Amin,[4] Niaz Ali Shah,[1] and Sahar Ahmed Idris[5,6]

[1]*Department of Mathematics, University of Swabi, Swabi 23561, KPK, Pakistan*
[2]*Department of Mathematics, College of Sciences and Arts, ArRass, Qassim University, Saudi Arabia*
[3]*Laboratory of Fundamental and Applied Mathematics of Oran (LMFAO), University of Oran 1, Oran, Algeria*
[4]*Department of Mathematics, Abdul Wali Khan University, Mardan, 23200 Khyber Pakhtunkhwa, Pakistan*
[5]*College of Industrial Engineering, King Khalid University, Abha 61471, Saudi Arabia*
[6]*Department of Mathematics, College of Sciences, Juba University, Sudan*

Correspondence should be addressed to Sahar Ahmed Idris; sa6044690@gmail.com

Received 26 August 2021; Accepted 11 October 2021; Published 29 October 2021

Academic Editor: David Carf

Unsteady electrohydrodynamic hybrid nanofluid (Al_2O_3-Cu/H_2O) past a convective heat stretched/shrinked sheet is examined. A stagnation point fluid flow with velocity slip constrains and heat source or sink is deliberated. The combined set of PDEs is translated into ODEs by including approved similarity transformations. HAM is applied for the solution to the obtained nonlinear system. The magnetic input factor, Prandtl number, electric field factor, Eckert number, heat source factor, and unstable factor are the governing parameters. The impact of these factors on the temperature and velocity profiles features of the problem is considered with explanation. Intensification in values of electric and magnetic fields parameters enhanced the heat transfer rate. The greater Prandtl number lessens the temperature. Amplification in temperature is perceived for Eckert parameter. The heat transferred rate of hybrid nanofluid in the entire domain increases as the heat source increases, while the heat sink has the opposite effect. Skin friction and Nusselt number is increased for increasing values of magnetic field parameters. It is also noted that Nusselt number lessens for raising in Pr, E, and Ec. Furthermore, it is eminent that the hybrid nanofluid possesses better result compared to the nanofluid.

1. Introduction

The ability of nanofluids to improve heat transfer performance in a range of industrial applications due to the substantial raise in thermal conductivity of the resulting fluid has piqued interest in recent years. A liquid in which nano-sized metallic or nonmetallic components are suspended is defined as this new class of fluids. By dispersing a composite nanopowder or various types of nanoparticles in the hybrid nano- and base fluids, which are a continuation of nanofluids, can be created. An enhanced nanofluid having two distinct nanoparticles scattered in the base fluid is called a hybrid nanofluid.

Many researchers have been interested in studying heat source in a hybrid nanofluid in recent years because of its ability to boost heat transfer rates when compared to ordinary nanofluid. As a result, most heat transferring uses, such as transformer cooling, electronic cooling, and coolant in machines, have used hybrid nanofluid as the heat source fluid. Nanofluid is an eminent as a high heat transferred when compared to other fluids. The hybrid nanofluid, on the other hand, is researched in this study is to strengthen the rate of heat source of the standard nanofluid. Several scientists used numerical methods to explore the heat transport and the boundary layering flow of a hybrid nanofluid. The researchers in [1] studied the flow of a hybrid nanofluid past

a stretched sheet by considering Cu-Al_2o_3 nanoparticles with magnetic impacts. Newtonian heated condition was examined by these researchers with the 3-D flow [2]. The rate of heat transferring of hybrid nanofluid was found to be greater than that of standard nanofluid. Hayat and Nadeem [3] considered the rotating flow of hybrid nanofluid which consisted of Ag-CuO/water. The authors in [4] conceptualize and investigate the flow of hybrid nanofluid over an unsteady stagnation point convective heat stretch/shrink surface including the velocity slip impact on heat transfer. Using the Buongiorno model, Daniel et al. [5] analyzed and interrogated mixed convection electrico MHD flow and heat source caused nano-fluid over a permeable stretched surface. Xie et al. [6] worked out on the friction coefficient and wear volume of hybrid nanoparticles to determine their tribological properties of the SiO_2/Mo S_2. When compared to pure nanofluids, they found that hybrid nanofluids have a smaller friction coefficient and wear volume. The authors in [7] scrutinized the impact of nanoparticle concentration and temperature distribution on rheological performance of (Fe_3O_2-Ag/EG) hybrid nanofluid.

Ghadikolaei et al. [8] examined the thermophysical possessions of (TiO_2-Cu/H_2O) with a shape factor with Lorentz forces. Hussian et al. [9] considered hybrid nanofluid containing (Al_2o_3-Cu/H_2o) and proved excellent results in the circumstance of their assumptions. They calculated numerical solutions using the finite element scheme and analyzed the impact of various input factors on the hybrid nanofluids. Magnetohydrodynamic (MHD) has recently gotten prominent attention due to its wide range of applications in geophysics, petroleum, chemical technology, environmental, engineering, and many other branches of science and technology. The Lorentz force which is also known as the drag force produced through the magnetic field that is used by MHD. Waqas et al. [10] investigated non-Newtonian liquid MHD mixed convection flow of fluid on stretched and nonlinear surface. Furthermore, the impact of magnetic field heat transferred of nanofluids in microchannels was discussed by the researchers in their research [11]. Other researchers also worked out in this area and produced a significant work in the field [12–14].

Scientists are interested in the stretching surface because of its numerous uses in engineering domains such as glass blowing, polymer extrusion, fast spray, wire drawing, quenching in metal foundries, and microelectronics cooling. The theoretical boundary layer flows over stretched sheet has been scrutinized by Crane [15]. Different authors investigated the exponentially stretching sheet [16–19], the main applications in technology and industry. In everyday life and industrial challenges, the exponentially shrinked/-stretched sheet is often used with fluid flow and heat transmission. The article by Magyari and Keller [20] appears to be the first to investigate at the fluid boundary layer flow on an exponentially stretched sheet. The exponential similarity variables were used by Mushtaq et al. [21] to turn the controlling PDEs into ODEs. Furthermore, the researchers in [22] interrogated the mixed convective flow of nanofluid and obtained excellent result and find out the influence of input parameter in the flow. The MHD fluid flow for the stagnation point was created by Rahman et al. [23], who employed exponential similarity variables to generate ODEs.

Fluid movement near a solid surface's stagnation area is explained by the stagnation point flow. Hiemenz [24] was the first to inspect stagnation-point flow problem in a flowing fluid over a fixed surface. Homann [25] then enlarged to a 3-D stagnation-point flow problem in the axis symmetric condition. The researcher in [26] reported a stagnation fluid flow in a diminishing surface. According to him, the presence of a stagnation fluid flow velocity can constrain the vorticity to maintain the flow, eliminating the need for suction on the shrinked sheet. Many academics have studied numerous influences on flow behavior by extending the stagnation-point flow problem. This problem is further investigated by Bachok et al. [27] without and with heat transferred where the authors discovered the decreasing case's solutions are no unique and that increasing the melting parameter reduces the heat source rate at the solid-fluid interface. In 1992, Liao [28] discovered that this method was a faster technique to get approximated solution and that it was a better fit for solving nonlinear problems. Several researchers contributed to find the solution through a homotopy analysis scheme (HAM) [29–32]. The reader can further study about heat transfer through nanofluid flow in Refs. [33–40].

The target of this work is to look into the combined impact of magnetic field, heat generation/absorption, electric field, and velocity slip parameter for unstable stagnation-point flow of electrical conducting hybrid nanofluids with the velocity slip input factor. In addition to this, we will focus on the stability of the system. As a result of the aforementioned issues, the researchers decided to interrogate the unstable stagnation-point flow towards a convective heated stretched or shrinked surface in alumina–copper/water (Al_2O_3-Cu/H_2O) to see how velocity slip affects heat transfer. To decrease the independent variables in governing equations resulting from mathematical modelling, a suitable set of dimensionless variables is utilised. By applying the homotopy method, an analytical solution has been computed.

2. Mathematical Formulation

This research considers the unstable 2-D stagnation point flow of a hybrid system (Al_2o_3-Cu/H_2o) nanofluid over a convective heated stretched or shrinked surface with the impact of velocity slip. In our formulation, the term $u_w(x, t) = bx/(1 - ct)$ is the stretched/shrinked velocity in which b represent a fix association with shrinked $(b < 0)$ and stretched $(b > 0)$. We have the following cases while c denotes the unsteadiness problem and the velocity of the free stream is defined by $u_e(x, t) = ax/(1 - ct)$. Here, $a > 0$ indicates the power of the stagnation flow. T_1 and T_0 are the ambient temperature and the reference temperature, respectively. Further, heat is provided to it with some specific temperature given by $T_f(x, t) = T_1 - T_0(ax^2/2v)(1 - ct)^{-3/2}$ which provided a heat transferred coefficient, denoted by h_f. Then, the governing equation of [4] with all our

assumptions is as follows:

$$\frac{\partial u}{\partial x} + \frac{\partial u}{\partial y} = 0, \tag{1}$$

$$\frac{\partial u}{\partial t} + u\frac{\partial u}{\partial x} + v\frac{\partial u}{\partial y} = \frac{\partial u_e}{\partial t} + \mu_e \frac{\partial u_e}{\partial x} + \frac{\mu_{\text{hnf}}}{\rho_{\text{hnf}}}\frac{\partial^2 u}{\partial y^2} + \frac{\sigma_{\text{hnf}}}{\rho_{\text{hnf}}}\left(E_0 B_0 - B_0^2 u\right), \tag{2}$$

$$\frac{\partial T}{\partial t} + u\frac{\partial T}{\partial x} + v\frac{\partial T}{\partial y} = \frac{k_{\text{hnf}}}{\left(\rho c_p\right)_{\text{hnf}}}\frac{\partial^2 T}{\partial y^2} + \frac{\sigma_{\text{hnf}}}{\left(\rho c_p\right)_{\text{hnf}}}\left(uB_0 - E_0\right)^2 + \frac{Q_0}{\left(\rho c_p\right)_{\text{hnf}}}\left(T - T_\infty\right), \tag{3}$$

where u and v indicated the velocity components along the x-axis and along the y-axis, respectively, while the dynamic viscosity is indicated by μ_{hnf}, T is the Al_2O_3-Cu/H_2O temperature, ρ_{hnf} is the density of Al_2o_3-Cu/H_2o, k_{hnf} is the conductivity of thermal/heat of Al_2o_3-Cu/H_2o, and $\left(\rho c_p\right)_{\text{hnf}}$ is the Al_2o_3-Cu/H_2o heat capacity.

$$u = u_w(x,t) + H_1 v\frac{\partial u}{\partial y}, v = 0, -k_{hnf}T_y = h_f\left(T_f - T\right)\text{at } y = 0,$$
$$u \longrightarrow u_e(x,t), T \longrightarrow T_\infty \text{ at } y \longrightarrow \infty. \tag{4}$$

The above given Equation (4) show the Bcs, together with the partial slip for velocity component, the velocity slip factor is $H_1 = H(1-ct)^{1/2}$, where the initial value of the velocity slip parameter has been denoted by H. The properties of copper (Cu) thermophysical along with water (H_2O) nanoparticles and with aluminum oxide (Al_2O_3) have been presented in Table 1. In the meantime, the thermophysical properties of hybrid nanofluid were published in Table 2. All the related input factors and symbols are represented in the nomenclature with detailed description.

To simplify the abovementioned problem represented in Equations (1)–(3) along with condition (4), we take the following similarity transformations [4]:

$$\psi = \left(\frac{av}{1-ct}\right)^{1/2} xf(\eta), \theta(\eta) = \frac{T - T_\infty}{T_f - T_\infty}, \eta = \left(\frac{a}{v(1-ct)}\right)^{1/2} y. \tag{5}$$

In the above, η is the similarity variable and $u = \partial\psi/\partial y$ and $v = -\partial\psi/\partial x$ are satisfied through the stream function ψ ; thus, we get the following:

$$u = \frac{ax}{1-ct}f'(\eta), v = -\left(\frac{av}{1-ct}\right)^{1/2} f(\eta). \tag{6}$$

In the case, when the similarity variables (5) and (6) are employed to (2) and (3), they are converted to the following equations:

$$\frac{\mu_{\text{hnf}}/\mu_f}{\rho_{\text{hnf}}/\rho_f}f''' + 2ff'' - f'^2 + 1 - \varepsilon\left(f' - \frac{1}{2}\eta f'' - 1\right) + \frac{\sigma_{\text{hnf}}/\sigma_f}{\rho_{\text{hnf}}/\rho_f}M\left(E - f'\right) = 0, \tag{7}$$

$$\frac{1}{\text{Pr}}\frac{k_{\text{hnf}}/k_f}{\left(\rho c_p\right)_{\text{hnf}}/\left(\rho c_p\right)_f}\theta'' + f\theta' - 2f'\theta + \frac{\varepsilon}{2}\left(\eta\theta' + 3\theta\right) + \frac{\sigma_{\text{hnf}}/\sigma_f}{\left(\rho c_p\right)_{\text{hnf}}/\rho_f}M\text{Ec}\left(f' - E\right) + \frac{Q\left(\rho c_p\right)_f}{\left(\rho c_p\right)_{\text{hnf}}}\theta = 0. \tag{8}$$

After that, the beginning and boundary constrain (4) becomes

$$f(0) = 0, f'(0) = \lambda + \gamma f''(0), -\frac{k_{\text{hnf}}}{k_f}\theta'(0) = Bi[1 - \theta(0)],$$
$$f'(\eta) \longrightarrow 1, \theta(\eta) \longrightarrow 0, \text{while } \eta \longrightarrow \infty, \tag{9}$$

Where $\varepsilon, M, E, \text{Ec}, \text{Pr}, \text{Bi}, \text{Re}_x, \lambda$, and Q unsteadiness parameter, magnetic parameter, ELECTRIC FIELD PARAMETER, Eckert number, local Reynolds number in the x-axis, Biot number, Prandtl number, ratio of velocity parameter, and heat source/sink parameter.

$$\lambda = \frac{G_r}{\text{Re}_x^2},$$
$$\varepsilon = \frac{b}{a},$$
$$\text{Re}_x = \frac{ax^2}{v_f},$$
$$\text{Pr} = \frac{v_f}{\alpha},$$
$$M = \frac{\sigma\beta_0^2}{\rho_f a},$$
$$\text{Bi} = \frac{h_f}{k}\sqrt{\frac{v_f}{a}},$$
$$\text{Ec} = \frac{ax^2}{c_p\Delta T},$$
$$Q = \frac{Q_0(1-ct)^2}{ax},$$
$$E = \frac{E_0}{\beta_0 ax}. \tag{10}$$

Table 1: Illustration of thermo-physical properties of Al_2O_3, H_2O, and Cu [4].

Thermophysical properties	Cu	Al_2O_3	H_2O
c_p(J/kgK)	385	765	4179
$\rho(\mathrm{kg/m^3})$	8933	3970	9971
k(W/mK)	400	40	0.613
$\beta \times 10^5$(1/K)	1.67	0.85	21

Table 2: Applied models for thermophysical properties of the hybrid nanofluid [4].

Property	Hybrid nanofluid
Thermal capacity	$(\rho c_p)_{\mathrm{hnf}} = (1-\phi_{\mathrm{hnf}})(\rho c_p)_f + \phi_1(\rho c_p)_{s1} + \phi_2(\rho c_p)_{s2}$
Density	$\rho_{\mathrm{hnf}} = (1-\phi_{\mathrm{hnf}})\rho_f + \phi_1\rho_{s1} + \phi_2\rho_{s2}$
Viscosity	$\mu_{\mathrm{hnf}} = 1/(1-\phi_{\mathrm{hnf}})^{2.5}$
Thermal conductivity	$k_{\mathrm{hnf}}/k_f = \left[((\phi_1 k_{s1} + \phi_2 k_{s2})/\phi_{\mathrm{hnf}}) + 2k_f + 2(\phi_1 k_{s1} + \phi_2 k_{s2}) - 2\phi_{\mathrm{hnf}} k_f/((\phi_1 k_{s1} + \phi_2 k_{s2})/\phi_{\mathrm{hnf}}) + 2k_f - 2(\phi_1 k_{s1} + \phi_2 k_{s2}) - \phi_{\mathrm{hnf}} k_f\right]$

3. Physical Quantities of Interest

For the above model, we take the coefficient of skin friction (c_f) and local Nusselt number (Nu_x) as follows:

$$C_f = \frac{\tau_w}{\rho_f u_e^2}, \qquad Nu_x = \frac{x q_w}{k_f(T_f - T_\infty)}. \tag{11}$$

In which

$$\tau_w = \mu_{\mathrm{hnf}}\left(\frac{\partial u}{\partial y}\right)_{y=0}, \qquad q_w = -k_{\mathrm{hnf}}\left(\frac{\partial T}{\partial y}\right)\Big|_{y=0}. \tag{12}$$

The dimensional form of the above is

$$[R_{ex}]^{1/2} C_f = \frac{\mu_{\mathrm{hnf}}}{\mu_f} f''(0), \qquad [R_{ex}]^{-1/2} Nu_x = -\frac{k_{\mathrm{hnf}}}{k_f}\theta'(0). \tag{13}$$

4. Solution by HAM

In this section of the paper, HAM will be used to solve Equations (7) and (8) with boundary conditions (9). Mathematica software is utilized for this purpose. The basic HAM derivation is given as follows:

$$L_{\widehat{f}}\left(\widehat{f}\right) = \widehat{f}''' - \widehat{f}', L_{\widehat{\theta}}\left(\widehat{\theta}\right) = \widehat{\theta}'' - \widehat{\theta}. \tag{14}$$

Linear operators $L_{\widehat{f}}$ and $L_{\widehat{\theta}}$ are specified by

$$L_{\widehat{f}}(\gamma_1 + \gamma_2 e^{-\eta} + \gamma_3 e^{\eta}) = 0, L_{\widehat{\theta}}(\gamma_4 e^{-\eta} + \gamma_5 e^{\eta}) = 0. \tag{15}$$

The nonlinear operators $N_{\widehat{f}}$ and $N_{\widehat{\theta}}$ are as follows:

$$\begin{aligned} N_{\widehat{f}}\left[\widehat{f}(\eta;\zeta)\right] &= \frac{\mu_{\mathrm{hnf}}/\mu_f}{\rho_{\mathrm{hnf}}/\rho_f}\widehat{f}_{\eta\eta\eta} + 2\widehat{f}\widehat{f}_{\eta\eta} - \widehat{f}_{\eta}^2 + 1 \\ &\quad - \varepsilon\left(\widehat{f}_{\eta} - \frac{1}{2}\eta\widehat{f}_{\eta\eta} - 1\right) + \frac{\sigma_{\mathrm{hnf}}/\sigma_f}{\rho_{\mathrm{hnf}}/\rho_f} M\left(E - \widehat{f}_{\eta}\right), \\ N_{\widehat{\theta}}\left[\widehat{f}(\eta;\zeta), \widehat{\theta}(\eta;\zeta), \widehat{\phi}(\eta;\zeta)\right] &= \frac{1}{\mathrm{Pr}}\frac{k_{\mathrm{hnf}}/k_f}{(\rho c_p)_{\mathrm{hnf}}/(\rho c_p)_f}\widehat{\theta}_{\eta\eta} + \widehat{f}\widehat{\theta}_{\eta} - 2\widehat{f}_{\eta}\widehat{\theta} \\ &\quad + \frac{\varepsilon}{2}\left(\eta\widehat{\theta}_{\eta} + 3\widehat{\theta}\right) + \frac{\sigma_{\mathrm{hnf}}/\sigma_f}{(\rho c_p)_{\mathrm{hnf}}/\rho_f} M\mathrm{Ec}\left(\widehat{f}_{\eta} - E\right) \\ &\quad + \frac{Q(\rho c_p)_f}{(\rho c_p)_{\mathrm{hnf}}}\widehat{\theta}, \end{aligned} \tag{16}$$

For Equations (7) and (8), we have shown the 0^{th}-order system as

$$\begin{aligned} (1-\zeta)L_{\widehat{f}}\left[\widehat{f}(\eta;\zeta) - \widehat{f}_0(\eta)\right] &= p\hbar_{\widehat{f}} N_{\widehat{f}}\left[\widehat{f}(\eta;\zeta)\right], \\ (1-\zeta)L_{\widehat{\theta}}\left[\widehat{\theta}(\eta;\zeta) - \widehat{\theta}_0(\eta)\right] &= p\hbar_{\widehat{\theta}} N_{\widehat{\theta}}\left[\widehat{\theta}(\eta;\zeta), \widehat{f}(\eta;\zeta)\right]. \end{aligned} \tag{17}$$

The BCs are:

$$\widehat{f}(\eta;\zeta)\Big|_{\eta=0}=0,\frac{\partial\widehat{f}(\eta;\zeta)}{\partial\eta}\Big|_{\eta=0}=\lambda+\gamma\widehat{f}_{\eta\eta}(0),f(0)=0,$$
$$\frac{k_{nf}}{k_f}\frac{\partial\widehat{\theta}(\eta;\zeta)}{\partial\eta}\Big|_{\eta=0}=-Bi\left(1-\widehat{\theta}(0)\right),$$
$$\frac{\partial\widehat{f}(\eta;\zeta)}{\partial\eta}\Big|_{\eta=\infty}\longrightarrow 1,\widehat{\theta}(\eta;\zeta)\Big|_{\eta=\infty}\longrightarrow 0, \tag{18}$$

While the embedded constraint is $\zeta\in[0,1]$, $\hbar_{\widehat{f}}$ and $\hbar_{\widehat{\theta}}$ are utilized to regulate the convergence. When $\zeta=0$ and $\zeta=1$, we have

$$\widehat{f}(\eta;1)=\widehat{f}(\eta),\widehat{\theta}(\eta;1)=\widehat{\theta}(\eta), \tag{19}$$

After that, $\widehat{f}(\eta;\zeta)$ and $\widehat{\theta}(\eta;\zeta)$ are expended through Taylor's expansion for $\zeta=0$:

$$\widehat{f}(\eta;\zeta)=\widehat{f}_0(\eta)+\sum_{n=1}^{\infty}\widehat{f}_n(\eta)\zeta^n,$$
$$\widehat{\theta}(\eta;\zeta)=\widehat{\theta}_0(\eta)+\sum_{n=1}^{\infty}\widehat{\theta}_n(\eta)\zeta^n,$$
$$\widehat{f}_n(\eta)=\frac{1}{n!}\frac{\partial\widehat{f}(\eta;\zeta)}{\partial\eta}\Big|_{p=0},$$
$$\widehat{\theta}_n(\eta)=\frac{1}{n!}\frac{\partial\widehat{\theta}(\eta;\zeta)}{\partial\eta}\Big|_{p=0}. \tag{20}$$

The BCs are

$$\widehat{f}(0)=0,\widehat{f}'(0)=\lambda+\gamma\widehat{f}''(0),\frac{k_{\text{hnf}}}{k_f}\widehat{\theta}'(0)=-Bi\left(1-\widehat{\theta}(0)\right)$$
$$\widehat{f}'(\eta)\longrightarrow 0,\widehat{\theta}(\eta)\longrightarrow 0,\eta\longrightarrow\infty. \tag{21}$$

Now,

$$\mathfrak{R}_n^{\widehat{f}}(\eta)=\frac{\mu_{\text{hnf}}/\mu_f}{\rho_{\text{hnf}}/\rho_f}\widehat{f}_{n-1}^{'''}+2\sum_{j=0}^{w-1}\widehat{f}_{w-1-j}\widehat{f}''_j-\widehat{f}_{n-1}^{'2}+1$$
$$-\varepsilon\left(\widehat{f}'_{n-1}-\frac{1}{2}\eta\widehat{f}_{n-1}-1\right)+\frac{\sigma_{\text{hnf}}/\sigma_f}{\rho_{\text{hnf}}/\rho_f}M\left(E-\widehat{f}'_{n-1}\right),$$
$$\mathfrak{R}_n^{\widehat{\theta}}(\eta)=\frac{1}{\text{Pr}}\frac{k_{\text{hnf}}/k_f}{(\rho c_p)_{\text{hnf}}/(\rho c_p)_f}\left(\widehat{\theta}''_{n-1}\right)+\sum_{j=0}^{w-1}\widehat{\theta}'_{w-1-j}\widehat{f}_j$$
$$-2\sum_{j=0}^{w-1}\widehat{\theta}_{w-1-j}\widehat{f}'_j+\frac{\varepsilon}{2}\left(\eta\widehat{\theta}'_{n-1}+3\widehat{\theta}_{n-1}\right)$$
$$+\frac{\sigma_{\text{hnf}}/\sigma_f}{(\rho c_p)_{\text{hnf}}/\rho_f}M\text{Ec}\left(\widehat{f}'_{n-1}-E\right)+\frac{Q(\rho c_p)_f}{(\rho c_p)_{\text{hnf}}}\widehat{\theta}_{n-1}, \tag{22}$$

with the condition

$$\chi_n=\begin{cases}0,\text{if } n\le 1,\\ 1,\text{if } n>1.\end{cases} \tag{23}$$

5. Results and Discussion

The transformed equations of concentration, energy, and momentum (7) and (8) with the boundary condition (9) are solved using the homotopy analysis technique in this work. Pr, M, E, ε, Ec, and Q are some of the parameters used in the computational analysis. $f'(\eta)$ for the different embedded parameters, such as E, M, and ε, are shown in Figures 1–3 to highlight the influence of these input factors on the system.

Higher values of E enhance the hybrid nanofluid velocity, as seen in Figure 1. An accelerating force is provided by an electric parameter. The stronger Lorentz force is connected with the higher value of E, whereas the weaker Lorentz force is related with the lower value of E. The larger Lorentz force enhances and resolves the sticky effect caused by nanoparticles in the fluid, indicating an enhancement in convective heating transferred and the thickness of the momentum barrier layer. In Figure 2, we have shown the effect of M on the hybrid nanofluid $f'(\eta)$. In which, we observed that the thickness of the velocity and momentum boundary layers decreased as the magnetic parameter was raised. Lorentz flow is a resistive type force that occurs when a magnetic field is applied in the opposite flow direction. As a result, the fluid flow behavior becomes more resistive, resulting in a decline in $f'(\eta)$ and a thickness boundary layer. In addition to this, we highlighted the impact of ε on the nanofluid $f'(\eta)$ in Figure 3.

Because of the acceleration situation $(\varepsilon>0)$, the hybrid nanofluid flow rate is slower, and the thickness of boundary layer of momentum is thinner. For enhanced acceleration, the $f'(\eta)$ decreases. In Figures 4–9, we illustrated the effect of Ec, E, Q, M, ε, and Pr on $\theta(\eta)$. Figure 4 shows that the thickness of the thermal boundary layer and the nanofluid temperature are increased as the kinetic energy to enthalpy ratio rises with an enhance in the Ec values. In Figures 5 and 6, the influence of heat absorption or generation on $\theta(\eta)$ is highlighted numerically. The parameter $\theta(\eta)$ of the fluid and the thickness of the thermal boundary layer are both increased when $(Q>0)$ is used.

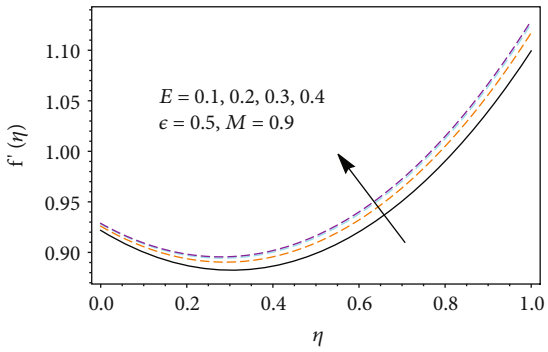

Figure 1: Illustration of the influence of E on $f'(\eta)$.

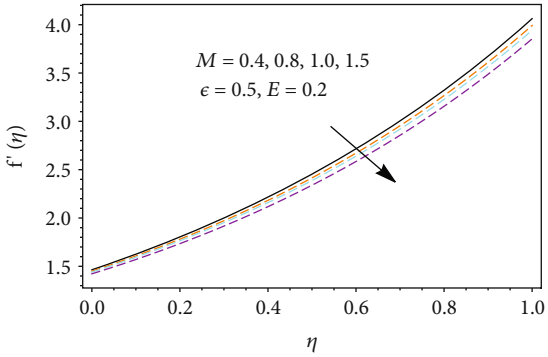

Figure 2: Illustration of the influence of M on $f'(\eta)$.

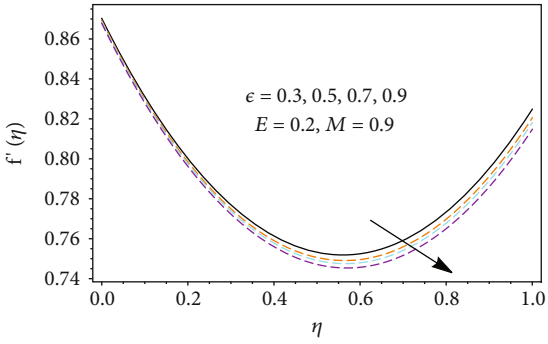

Figure 3: Illustration of the influence of the ε on $f'(\eta)$.

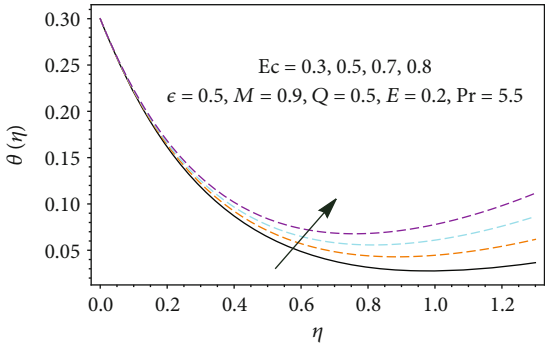

Figure 4: Illustration of the influence of Ec on $\theta(\eta)$.

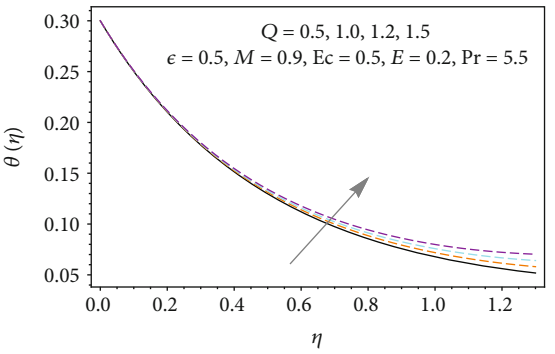

Figure 5: Illustration of the influence of the input factor $Q > 0$ on $\theta(\eta)$.

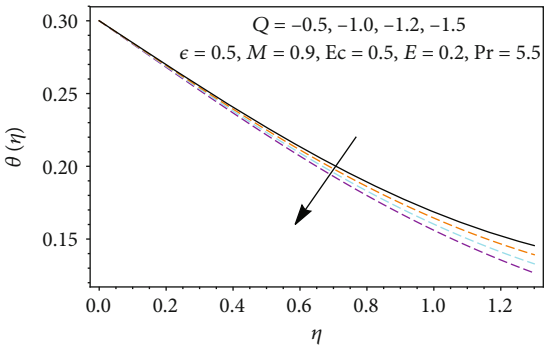

Figure 6: Illustration of the influence of the input factor $Q < 0$ on $\theta(\eta)$.

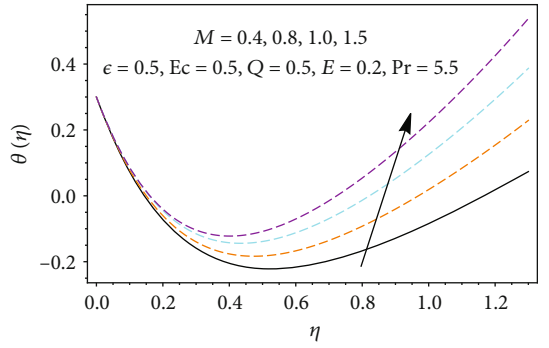

Figure 7: Illustration of the influence of M on $\theta(\eta)$.

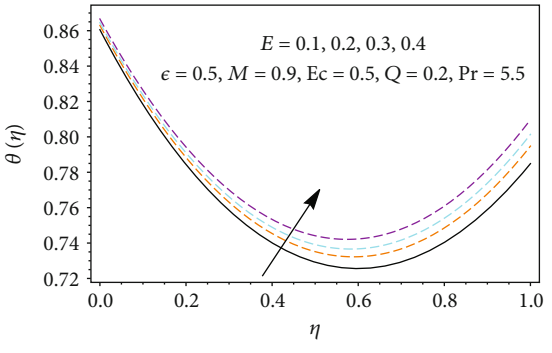

Figure 8: Illustration of the influence of the electric field parameter on temperature profile.

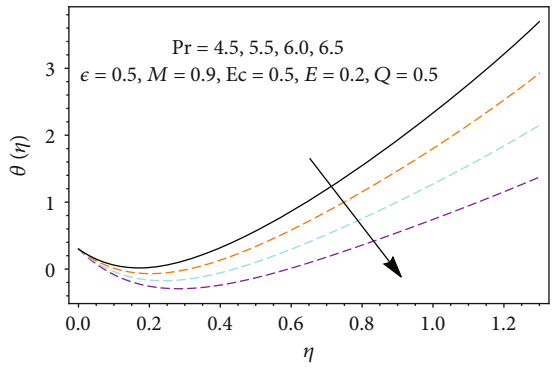

Figure 9: Illustration of the influence of the input factor Pr on $\theta(\eta)$.

Table 3: Impact of different input factors on skin friction $[R_{ex}]^{1/2} C_f = (\mu_{hnf}/\mu_f) f''(0)$.

ε	E	M	$\left(\mu_{hnf}/\mu_f\right) f''(0)$
0.3	0. 1	0.4	0.72059328
0.5			0.83542092
0.7			1.03614135
	0.1		1.86313569
	0.2		1.64385204
	0.3		1.76103193
		0.4	1.03873708
		0.8	1.30863981
		1.0	1.58376213

On the other hand, $(Q < 0)$ outcomes in a lower fluid temperature and a smaller thickness of the thermal boundary layer. $Q = 0$ denotes the lack of heat generation or absorption. Figure 7 reveals the impact of M on $\theta(\eta)$ of the nanofluids. We noticed that the transverse magnetic field increases the thickness of the thermal boundary layer. As a result, the temperature of the fluid as well as the thickness of the thermal boundary layer increased. The magnetic field acts as a strong Lorentz force, increasing the temperature of the nanofluid in the boundary region. Figure 8 shows the depicts the impact of E on $\theta(\eta)$.

The impact of E on $\theta(\eta)$ is shown in Figure 8, which showed that the electric field acts as an accelerating force, raising the fluid flow temperature and increasing the thickness of the thermal boundary layer. A thicker, higher quantity temperature distribution within the boundary layer region of the hybrid nanofluid's vicinity is connected with a greater value of an electric field. The Prandtl number is a material property that varies depending on the fluid. From Figure 9, it reveals that as it raises in Pr, $\theta(\eta$) declines. Moreover, the higher value of Pr implies smaller thermal diffusivity than the momentum diffusivity. As a result, the energy boundary layer thickness declines. Table 3 represents that C_f is raised when the values of $M, \varepsilon,$ and E are increased. Table 4 shows that Nu_x is

Table 4: Impact of different input factors on the Nusselt number $[(-k_{hnf}/k_f)\theta'(0)]$.

Ec	Q	Pr	M	E	$-\left(k_{hnf}/k_f\right)\theta'(0)$
0.3	0.5	4.5	0.4	0.1	1.07386504
0.5					1.17290347
0.7					1.23893104
	0.5				2.30319769
	1.0				2.15912307
	1.5				2.02463073
		4.5			0.54354079
		5.5			0.73865302
		6.5			0.93865321
			0.4		1.13159603
			0.8		1.09764384
			1.0		1.05346068
				0.1	1.12183304
				0.2	1.23583931
				0.3	1.30346893

increased when the values of M, Q are increased. The Nu_x is decreased, when the values of Pr, E, and Ec is increased.

6. Concluding Remarks

This study investigates the unsteady electrohydrodynamic stagnation-point fluid flow of a hybrid nanofluid over a convective heat stretch or shrink sheet, taking into account the velocity slip effect on heat transferred. The effects of heat generation and absorption, as well as the electric and magnetic fields, are all taken into account. The following are the main observations of the present study:

(i) $f'(\eta)$ and $\theta(\eta)$ raises with an enhance in the value of E

(ii) The magnetic factor has an inverse impact for velocity and temperature gradient

(iii) A heat source raises the temperature, whereas a heat sink does the opposite

(iv) The velocity and temperature are reduced at higher levels of the unsteadiness parameter

(v) The Eckert parameter shows an enhance in temperature, while Pr shows a reduction

(vi) Skin friction is raised when the values of $M, \varepsilon,$ and E are augmented

(vii) The Nusselt number is enlarged when the values M, Q are increased, and Nu_x is diminished, when the values of Pr, E, and Ec are enlarged

Nomenclature

u_w: Stretched/shrinking velocity (m/s)
u and v: Along x- and y-axis velocity terms (m/s)
$(\rho c_p)_{\text{hnf}}$: Volumetric heat capacity of hybrid nanofluid ($m^2s^{-2}K^{-1}$)
T_1: Ambient temperature (K)
h_f: Coefficient of heat transfer
μ_{hnf}: Hybrid nanofluid viscosity ($kgm^{-1}s^{-1}$)
k_{hnf}: Hybrid nanofluid thermal/heat conductivity
Re_x: Reynolds number
H_1: Velocity slip factor
ρ_s: The density of the nanoparticle(kgm^{-3})
ψ: Stream function
Ec: Eckert number
Pr: Prandtl number
Bi: Biot number
Nu_x: Local Nusselt number
λ: Ratio of velocity parameter and heat
f': Dimensionless velocity
υ: Kinematic viscosity (m^2s^{-1})
ϕ: Nanoparticle solid volume fraction
x, y: Plane coordinate axis
u_e: Strength of the stagnation flow
ρ_f: Basie fluid density (kgm^{-3})
T_0: Reference temperature (K)
ρ_{hnf}: Hybrid nanofluid density (kgm^{-3})
k_s: Nanoparticle thermal conductivity ($Wm^{-1}K^{-1}$)
η: Similarity variable
H: Initial value of the velocity slip factor
c_p: Heat capacity constant pressure
k_f: Base fluid thermal conductivity ($Wm^{-1}K^{-1}$)
ε: Unsteadiness parameter
E: Electric field parameter
M: Magnetic parameter
Q: Source/sink parameter.
c_f: Coefficient of skin friction
μ_f: Dynamic viscosity ($kgm^{-1}s^{-1}$)
T: Temperature of fluid (K)
τ_w: Wall shear stress
q_w: Transportation of heat.

Data Availability

No data were used to support the study.

Conflicts of Interest

The authors declare that they have no conflicts of interest.

Acknowledgments

The sixth named author extends appreciation to the Deanship of Scientific Research at King Khalid University for funding this work through research groups program under grant (RGP2/53/42).

References

[1] S. P. A. Devi and S. S. U. Devi, "Numerical investigation of hydromagnetic hybrid Cu – Al_2O_3/Water nanofluid flow over a permeable stretching sheet with suction," *International Journal of Nonlinear Sciences and Numerical Simulation*, vol. 17, no. 5, pp. 249–257, 2016.

[2] S. S. U. Devi and S. P. A. Devi, "Numerical investigation of three-dimensional hybrid Cu–Al_2O_3/water nanofluid flow over a stretching sheet with effecting Lorentz force subject to Newtonian heating," *Canadian Journal of Physics*, vol. 94, no. 5, pp. 490–496, 2016.

[3] T. HAYAT and S. NADEEM, "Heat transfer enhancement with Ag-CuO/water hybrid nanofluid," *Results in Physics*, vol. 7, pp. 2317–2324, 2017.

[4] N. A. Zainal, R. Nazar, K. Naganthran, and I. Pop, "Unsteady stagnation point flow of hybrid nanofluid past a convectively heated stretching/shrinking sheet with velocity slip," *Mathematics*, vol. 8, no. 10, pp. 1649–1722, 2020.

[5] Y. S. Daniel, Z. A. Aziz, Z. Ismail, and F. Salah, "Double stratification effects on unsteady electrical MHD mixed convection flow of nanofluid with viscous dissipation and Joule heating," *Journal of Applied Research and Technology*, vol. 15, no. 5, pp. 464–476, 2017.

[6] H. Xie, B. Jiang, B. Liu, Q. Wang, J. Xu, and F. Pan, "An investigation on the tribological performances of the SiO2/MoS2 hybrid nanofluids for magnesium alloy-steel contacts," *Nanoscale Research Letters*, vol. 11, no. 1, pp. 329–336, 2016.

[7] M. Afrand, D. Toghraie, and B. Ruhani, "Effects of temperature and nanoparticles concentration on rheological behavior of Fe_3O_4-Ag/EG hybrid nanofluid: an experimental study," *Experimental Thermal and Fluid Science*, vol. 77, pp. 38–44, 2016.

[8] S. S. Ghadikolaei, M. Yassari, H. Sadeghi, K. Hosseinzadeh, and D. D. Ganji, "Investigation on thermophysical properties of Tio_2-Cu/H_2O hybrid nanofluid transport dependent on shape factor in MHD stagnation point flow," *Powder Technology*, vol. 322, pp. 428–438, 2017.

[9] S. Hussain, S. E. Ahmed, and T. Akbar, "Entropy generation analysis in MHD mixed convection of hybrid nanofluid in an open cavity with a horizontal channel containing an adiabatic obstacle," *International Journal of Heat and Mass Transfer*, vol. 114, pp. 1054–1066, 2017.

[10] M. Waqas, M. Farooq, M. I. Khan, A. Alsaedi, T. Hayat, and T. Yasmeen, "Magnetohydrodynamic (MHD) mixed convection flow of micropolar liquid due to nonlinear stretched sheet with convective condition," *International Journal of Heat and Mass Transfer*, vol. 102, pp. 766–772, 2016.

[11] G. Zhao, Y. Jian, and F. Li, "Streaming potential and heat transfer of nanofluids in microchannels in the presence of magnetic field," *Journal of Magnetism and Magnetic Materials*, vol. 407, pp. 75–82, 2016.

[12] D. Yadav, J. Wang, R. Bhargava, J. Lee, and H. H. Cho, "Numerical investigation of the effect of magnetic field on the onset of nanofluid convection," *Applied Thermal Engineering*, vol. 103, pp. 1441–1449, 2016.

[13] A. J. Chamkha, A. M. Rashad, E. R. EL-Zahar, and H. A. EL-Mky, "Analytical and numerical investigation of Fe_3O_4–water nanofluid flow over a moveable plane in a parallel stream with high suction," *Energies*, vol. 12, no. 1, pp. 198–198, 2019.

[14] S. M. M. el-Kabeir, E. R. el-Zahar, M. Modather, R. S. Gorla, and A. M. Rashad, "Unsteady MHD slip flow of a ferrofluid

over an impulsively stretched vertical surface," *AIP Advances*, vol. 9, no. 4, article 045112, 2019.

[15] L. J. Crane, "Flow past a stretching plate," *Zeitschrift für angewandte Mathematik und Physik ZAMP*, vol. 21, no. 4, pp. 645–647, 1970.

[16] N. Sandeep, C. Sulochana, and B. Rushi Kumar, "Unsteady MHD radiative flow and heat transfer of a dusty nanofluid over an exponentially stretching surface," *Engineering Science and Technology, an International Journal*, vol. 19, no. 1, pp. 227–240, 2016.

[17] M. K. Nayak, N. S. Akbar, D. Tripathi, Z. H. Khan, and V. S. Pandey, "MHD 3D free convective flow of nanofluid over an exponentially stretching sheet with chemical reaction," *Advanced Powder Technology*, vol. 28, no. 9, pp. 2159–2166, 2017.

[18] T. Hayat and S. Nadeem, "Flow of 3D Eyring-Powell fluid by utilizing Cattaneo-Christov heat flux model and chemical processes over an exponentially stretching surface," *Results in Physics*, vol. 8, pp. 397–403, 2018.

[19] F. U. Rehman, S. Nadeem, and R. U. Haq, "Heat transfer analysis for three-dimensional stagnation-point flow over an exponentially stretching surface," *Chinese Journal of Physics*, vol. 55, no. 4, pp. 1552–1560, 2017.

[20] E. Magyari and B. Keller, "Heat and mass transfer in the boundary layers on an exponentially stretching continuous surface," *Journal of Physics D: Applied Physics*, vol. 32, no. 5, pp. 577–585, 1999.

[21] A. Mushtaq, M. A. Farooq, R. Sharif, and M. Razzaq, "The impact of variable fluid properties on hydromagnetic boundary layer and heat transfer flows over an exponentially stretching sheet," *Journal of Physics Communications*, vol. 3, no. 9, article 095005, 2019.

[22] G. B. Reddy, B. S. Goud, and M. R. Shekar, "Numerical solution of MHD mixed convective boundary layer flow of a nanofluid through a porous medium due to an exponentially stretching sheet with magnetic field effect," *International Journal of Applied Engineering Research*, vol. 14, pp. 2074–2083, 2019.

[23] A. N. H. Rahman, N. Bachok, and H. Rosali, "Numerical solutions of MHD stagnation-point flow over an exponentially stretching/shrinking sheet in a nanofluid," *Journal of Physics: Conference Series*, vol. 1366, article 012012, 2019.

[24] K. Hiemenz, "Die grenzschicht an einem in den gleichformigen flussigkeitsstrom eingetauchten geraden kreiszylinder," *Dingler's Polytechnisches Journal*, vol. 326, pp. 321–410, 1911.

[25] F. Homann, "Der Einfluß großer Zähigkeit bei der Strömung um den zylinder und um die kugel," *Zeitschrift für Angewandte Mathematik und Mechanik*, vol. 16, no. 3, pp. 153–164, 1936.

[26] K. L. Hsiao, "Stagnation electrical MHD nanofluid mixed convection with slip boundary on a stretching sheet," *Applied Thermal Engineering*, vol. 98, no. 5, pp. 850–861, 2016.

[27] N. Bachok, A. Ishak, and I. Pop, "Melting heat transfer in boundary layer stagnation-point flow towards a stretching/shrinking sheet," *Physics letters A*, vol. 374, no. 40, pp. 4075–4079, 2010.

[28] S. J. Liao, "On the homotopy analysis method for nonlinear problems," *Applied Mathematics and Computation*, vol. 147, no. 2, pp. 499–513, 2004.

[29] N. Nasir, Z. Shah, S. Islam, E. Bonyah, and T. Gul, "Darcy Forchheimer nanofluid thin film flow of SWCNTs and heat transfer analysis over an unsteady stretching sheet," *AIP Advances*, vol. 9, no. 1, article 015223, 2019.

[30] I. Tlili, W. A. Khan, and I. Khan, "Multiple slips effects on MHD SA- Al_2O_3 and SA-Cu non-Newtonian nanofluids flow over a stretching cylinder in porous medium with radiation and chemical reaction," *Results in physics*, vol. 8, pp. 213–222, 2018.

[31] N. S. Khan, Z. Shah, S. Islam, I. Khan, T. A. Alkanhal, and I. Tlili, "Entropy generation in MHD mixed convection non-Newtonian second-grade nanoliquid thin film flow through a porous medium with chemical reaction and stratification," *Entropy*, vol. 21, no. 2, article e21020139, p. 139, 2019.

[32] M. Fiza, S. Islam, H. Ullah, Z. Shah, and F. Chohan, "An asymptotic method with applications to nonlinear coupled partial differential equations," *Punjab University Journal of Mathematics*, vol. 50, pp. 139–151, 2018.

[33] N. Mezouar and S. M. Boulaaras, "Global existence and decay of solutions of a singular nonlocal viscoelastic system with damping terms," *Topological Methods in Nonlinear Analysis*, vol. 56, no. 1, pp. 1–312, 2020.

[34] S. M. Boulaaras, A. Choucha, A. Zara, M. Abdalla, and B. B. Cheri, "Global existence and decay estimates of energy of solutions for a new class of -Laplacian heat equations with logarithmic nonlinearity," *Journal of Function Spaces*, vol. 2021, Article ID 5558818, 11 pages, 2021.

[35] S. M. Boulaaras and M. Haiour, "The finite element approximation of evolutionary Hamilton–Jacobi–Bellman equations with nonlinear source terms," *Indagationes Mathematicae*, vol. 24, no. 1, pp. 161–173, 2013.

[36] S. M. Boulaaras, "Some new properties of asynchronous algorithms of theta scheme combined with finite elements methods for an evolutionary implicit 2-sided obstacle problem," *Mathematical Methods in the Applied Sciences*, vol. 40, no. 18, pp. 7231–7239, 2017.

[37] S. Khattak, I. Hussain, J. F. Gomez-Aguilar, and R. Jan, "Analysis of PD-type iterative learning control for discrete-time singular system," *Mathematical Methods in the Applied Sciences*, 2021.

[38] S. Toualbia, A. Zaraï, and S. M. Boulaaras, "Decay estimate and non-extinction of solutions of p-Laplacian nonlocal heat equations," *AIMS Mathematics*, vol. 5, no. 3, pp. 1663–1679, 2020.

[39] W. U. Jan, M. Farooq, R. A. Shah, A. Khan, M. S. Zobaer, and R. Jan, "Flow dynamics of the homogeneous and heterogeneous reactions with an internal heat generation and thermal radiation between two squeezing plates," *Mathematics*, vol. 9, no. 18, p. 2309, 2021.

[40] K. Hosseini, M. Ilie, M. Mirzazadeh, and D. Baleanu, "An analytic study on the approximate solution of a nonlinear time-fractional Cauchy reaction–diffusion equation with the Mittag–Leffler law," *Mathematical Methods in the Applied Sciences*, vol. 44, no. 8, pp. 6247–6258, 2021.